Murdoch
UNIVERSITY

School of Engineering and Information Technology

Stability Aspects of Wind Power Integration in Power Systems and Microgrids

Amit Kunwar

This thesis is presented for the Degree of

Doctor of Philosophy

of

Murdoch University

July 2019

Declaration

I declare that this thesis is my own account of my research and contains as its main content work, which has not previously been submitted for a degree at any tertiary education institution.

Amit Kunwar

July 2019

Abstract

Wind farms can be located in remote and weak parts of power networks, due to the availability of wind energy. With integration of power from such wind farms, the power system's stability might be affected especially at higher penetration levels. Instability issues resulting from such incorporations must be addressed to accommodate higher wind power penetration in the power networks. This thesis attempts to analyse the stability issues of power system with integration of variable speed wind turbine technology especially focusing on doubly fed induction generators. Additionally, a microgrid with different inertial and non-inertial sources is examined for enhancing design aspect of such microgrids from stability perspectives.

At different penetration levels of wind power, oscillatory modes are identified, and participation factors of the most associated state variables on such oscillatory modes are observed. Flexible ac transmission system based series and shunt devices are found effective in enhancing the small signal stability of such power networks for different wind power penetration levels. Besides, series devices are observed to contribute to an improvement in the transient behaviour of the power system. Similarly, high voltage dc link is also witnessed to positively influence low frequency oscillation damping. Furthermore, this thesis shows that higher voltage gain values of wind farms can contribute to an improvement in the small signal stability for increased wind power penetration. Another observation displays that a doubly fed induction based wind farm can contribute to improving the voltage stability of a distribution network in a steady state operating condition, as well as following disturbances. Based on the study on an isolated microgrid that has a combination of synchronous, converter-based distributed resources, and energy storage systems, it is observed that a suitable modification in such microgrid's various components and parameters can positively influence its small signal stability.

Table of Contents

List of Figures

List of Tables

List of Abbreviations

BES	Battery Energy Storage
DFIG	Doubly Fed Induction Generator
FACTS	Flexible ac Transmission System
HVDC	High Voltage Direct Current
IEEE	Institute of Electrical and Electronics Engineers
SCIG	Squirrel Cage Induction Generator
SSSC	Static Synchronous Series Compensator
STATCOM	Static Compensator
SVC	Static Var Compensator

Chapter 1 Introduction

A major portion of world electricity is still generated from fossil fuels due to the low unit price of power generation. Such dependency has led to environmental degradation such as global warming and environmental pollution which has necessitated exploration and development of alternative clean energy resources for electricity generation. Renewable energy policies and governments initiatives such as carbon tax are being placed and endorsed to promote environmentally friendly energy resources including wind power. Such initiatives have assisted in the increase of the penetration of these renewable resources in the power sector requiring an urgent understanding of their impact on the power system stability, especially at their higher penetration levels.

1.1 Background

Environmental concerns, exhaustive nature of the fossil fuels and increasing energy needs have encouraged the search for alternative energy resources for electricity generation. Recent advancement in the renewable energy technologies, coupled with the reduction in their unit energy generation cost, has opened opportunities for the renewable energy resources for their integration in power networks. More importantly, in contrast to the conventional energy sources which are concentrated in limited geographical areas in the whole world, the renewable energy resources exist virtually everywhere [1]. Wind power is the most promising of the renewable resources from technical and economic perspective.

People have harnessed wind energy from the ancient ages for their usages such as pumping water, grinding grains, cutting wood at sawmills, etc. Since the 20^{th} century, wind power has found a new application in electric power generation from small wind plants suitable for farms and residences to larger utility-scale wind farms connected to the electricity grids [2].

Fig. 1.1 shows the worldwide installed wind power capacity during 2001- 2017 [3]. In the last seventeen years, the total annual installed wind capacity has increased from 6.5 to 52.573 GW. However, in 2017 the annual installed wind capacity has shown a decline in comparison to a previous couple of years. Given the economic climate, the wind installation in 2017 is still a strong growth; even though it does not follow the overall upward trend of wind installation in the preceding years. This shows a strong commitment to wind installation, by power industries around the globe, as the source of electricity generation.

China led the overall wind market since 2009 and remained at the top in 2017 as well. With China's dominance, the installation in Asia leads the global market; with Europe remaining at the second spot then comes North America. In 2017, the new installed wind capacity in Asia alone was 24.447 GW followed by 16.845 GW in Europe and 7.836 GW in North America. This brings the total installed wind capacity in Asia to 228,542 GW, in Europe to 178.096 GW, and in North America to 105.321 GW. With all these and from the remaining part of the world, the cumulative global wind capacity reaches 539.581 GW [3].

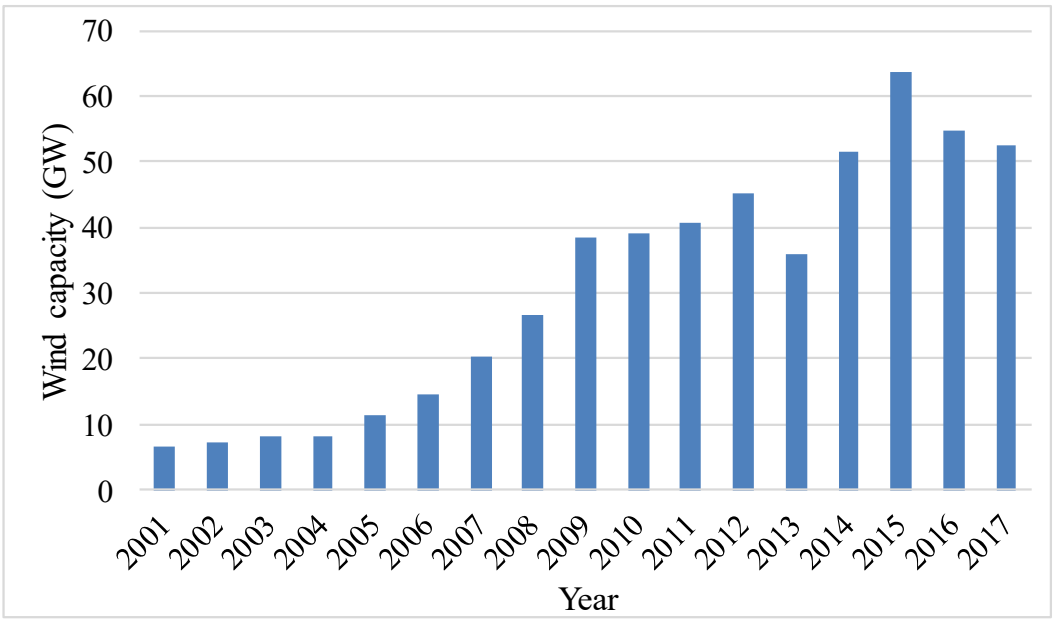

Figure 1.1 Global wind power installed capacity

In America, about 7.017 GW of the wind capacity was installed in 2017 alone which brought the total installed capacity to 89.077 GW. In addition to that, there is about 28.668 GW capacity of wind farms in the construction stage [4]. Hence, there is a

promising future for global wind power installation, which is expected to reach about 800 GW by 2021 [5]. Coming to the Australian context, it has some of the world's best wind resources, with such resources mainly located in the southern part of the country [6]. It is one of the 24 countries which have installed capacity of more than 1000 MW. Australia added 245 MW in 2017, bringing the total installed wind capacity to 4.557 GW [3]. South Australia has the highest wind installed capacity accounting for more than 25% of the state's electricity requirement. With the renewable energy target of 20% of Australia's power by 2020, there is a high prospect for the development of the wind sector in the country. Table 1.1 shows the installed wind capacity by state, in Australia till 2016 [7]. Sydney has outlined measures for procuring 100% of its electricity from renewable energy sources, including wind by 2030, in its renewable energy master plan. Similarly, a new climate action plan of the Tasmanian Government has a commitment to 100% renewable by 2020 [8].

Table 1.1 Installed wind capacity (in MW) by the state in Australia

South Australia	1595
Victoria	1250
Western Australia	491
Tasmania	310
New South Wales	668
Queensland	13
Total	4326

With such commitments from many countries including Australia, it's a requirement to understand how the increased wind power integration affects the stability of the power networks, especially at the higher penetration levels. At the small penetration levels, wind power has a very minimal impact on the power system stability; however, as the penetration level increases, it may adversely impact the power networks, requiring a strong support system especially during the disturbances. Wind farms are generally located at a geographically distant location, far from the load centers and are connected to a weak part of the networks. Due to a high wind power penetration on such weak networks, the power system might present serious concerns regarding the power system stability. The study of this issue is the main focus of this thesis. Hence, this research attempts to investigate the network stability issues of high power

penetration from variable speed wind technology like doubly fed induction generator (DFIG).

1.2 Power system stability

Power system stability is the property of a power system that enables it to maintain the state of operating equilibrium under normal condition and to regain an acceptable equilibrium state following network disturbances [9]. Such disturbances in power network may be small in the form of gradual load changes, the operation of the controllers, etc., and large in the form of the loss of a large generator or load, and a short circuit on a power line, etc. [10].

Power system stability may be classified as rotor angle stability and voltage stability [9-10]. Rotor angle stability refers to the synchronism in synchronous machines in the power system, whereas, the voltage stability refers to the ability of the power system to maintain acceptable voltages at all its buses. The rotor angle stability can be sub-categories as small signal stability and transient stability. The small signal stability is the power system's ability to maintain synchronism following the occurrence of small disturbances. In contrary, the transient stability refers to its ability to maintain synchronism following severe transient disturbances [9]. The power system stability is the main concern for the secure and reliable operation of the power system. The growth in interconnections, addition of new renewable technologies and their operation in stressed conditions have raised concerns for the power system instability even higher than before [10].

High penetration from wind farms could influence the dynamic behaviour of the whole power system network. Therefore, the wind power integration might introduce some challenges to the power system reliability and stability concerns. More importantly, as the world is moving towards increasing renewable penetration including the wind energy, their effect in the power system stability is still not very well explored and perceived. In this context, this thesis attempts to address the rotor angle stability concerns, mostly focusing on the small signal stability, with the variable speed wind farm integration. This thesis has been extended to the distribution level to address the voltage stability impact of the DFIG-based wind farm integration to observe steady state and transient voltage responses. In the end, the small signal stability of a

microgrid network is studied with a variation in the parameters of its renewable energy resources as well as those of the other network components.

1.3 Motivation

Technology has enabled wind energy to be utilized for the utility scaled electricity production. The environmental benefits and cost reduction in the wind technologies have placed wind power as a competitive resource to the conventional energy resources for the electricity production. Penetration of wind power in the electricity networks has increased significantly and will continue to grow for the above-mentioned reasons. In this scenario, the network stability issues need to be addressed to accommodate the higher penetration of wind power as well as the stable power system operations during the steady state condition and following network disturbances so as to guarantee the reliability and power quality to the end users.
This thesis investigates the small signal stability and voltage stability issues of the electricity networks under increased power penetrations from wind power. Additionally, this thesis attempts to establish a better understanding of the interactions of the wind power penetration with the power system components such as the conventional synchronous generator, static var compensator (SVC), static synchronous series compensator (SSSC), high voltage direct current (HVDC) link, large motor loads and battery energy storages (BESs).

1.4 Research objectives

The main research objective is to investigate the impact of higher penetration of wind power into the electricity networks from the stability point of view. The other major points can be summarized as

- To study the impact of different penetration levels of wind power on the small signal stability of the power system.
- To observe the effect of other network components on the high wind power penetration from the stability power of view.
- To study the impact of the wind power penetration on the voltage stability of a weak distribution network.

- To study the impact of a variation in the parameters and penetration level of renewable resources, including the converter-based energy resources to resemble wind farms, on the small signal stability of a microgrid.

1.5 Outline of research contributions

The main intent of this thesis is to analyse the power system stability issues, with the integration of wind farm, for enabling high penetration of the renewable resource.
The main contribution of this thesis can be listed as

- Investigation of the impact of a remotely connected DFIG-based wind farm on the low frequency oscillations and the identification of the influence of the series compensation on those oscillations. The study shows an increase in series compensation has a positive influence on the power system stability for the wind farm connected power network.
- Investigation of the impact of the DFIG-based wind farm on the small signal stability of a power system with an HVDC link. The study shows how the HVDC link influences the stability as the wind power penetration varies.
- Investigation of the impact of the DFIG-based wind farm on the voltage stability of a weak distribution network. The study identifies how a wind farm connected near a large industrial/commercial load influences the system voltages at the steady state condition and following system disturbances.
- Design of a supplementary controller for an improvement of the small signal stability of a power system at the high penetration of wind power from a DFIG-based wind farm.
- Small signal stability study of a microgrid with converter-based and conventional inertial renewable resources, and battery storage system. The study identifies the influence of the sources' and the network parameters on the dynamic stability of the microgrid.

These contributions would support for the better understanding of the stability aspects of the increased wind power penetrations into the power system networks.

1.6 Organization of the thesis

The thesis is organized as follows

Chapter 1, which is the current chapter, gives a background of this research work. This provides brief outlines of the wind installation till date and the commitments for an increase in the wind integrations. This chapter also presents the motivations for this research, the research objectives, and finally the contributions of this research work in the field of stability issues of wind power integration.

Chapter 2 gives a more detailed justification of why the research problem is addressed. This chapter through the literature survey provides evidence that others agree with this being a relevant issue and how they have tried to address this issue. The small signal stability, transient stability, and voltage stability analysis have been discussed briefly. This chapter also presents the stability impacts of wind integration and the control of power system oscillations. In addition to that, the stability of a microgrid is discussed and presented in this chapter.

Chapter 3 presents the modelling of the power system components used for the research work. The components are modelled for the stability analysis of the test power systems. The mathematical formulations of the power system components and devices are developed and discussed in this chapter, which is used in the later chapters for the detailed study and analysis work.

Chapter 4 presents the steady state and dynamic voltage stability analysis of a distribution system with a remote wind farm. Transient voltage responses are studied under different fault scenarios. This chapter also presents the simulation and analysis of the results obtained.

Chapter 5 discusses the design of a supplementary controller to damp critical oscillatory modes in the power networks. A methodology to select the best input signal for the controller is developed and presented. The time domain simulations are used to observe the effectiveness of the designed controller.

Chapter 6 portrays outcomes of the small signal stability analysis of the DFIG-based wind farm integrated into the power network. A comparative analysis of the influence of an HVDC link on the behaviour of the oscillatory modes is analysed and presented in this chapter.

Chapter 7 discusses the stability analysis of a power system with a remote DFIG-based wind farm connected through a long line. The simulation and small signal

stability analysis of the power system with and without a series compensation are presented here. A sensitivity analysis of the oscillatory modes to the system parameters is examined.

Chapter 8 covers the small signal stability study of a microgrid with converter-based and conventional inertia-based renewable resources, and battery storage systems. The study identifies the influence of the sources' and network parameters on the dynamic stability of the microgrid through a sensitivity type analysis.

Chapter 9 concludes the research work by summarising the major contributions. This chapter also proposes future works in the direction of the research field.

Chapter 2 Literature review

In this chapter, the integration impacts of a variable speed wind technology on the stability of the power system, and the control of power oscillations are presented through a detail literature survey. The power system stabilities such as small signal stability, transient stability, and voltage stability issues are briefly discussed and classified. The impact of wind penetration on these stabilities are presented as being an issue to the power system, especially at the high wind penetration levels. Additionally, the stability aspects of a microgrid are discussed and presented.

2.1 Wind energy conversion system

A conventional power system is controllable for power output; however, a wind-based power system depends on the availability of variable wind from nature. However, with the technological improvement and economic competitiveness, the wind power is an important energy source today. These superiorities exist over other the renewable sources, making the wind power a clear choice for the utility scale power production. A wind energy conversion system converts the wind's kinetic energy into the electric energy or other energy forms. Being environmentally friendly and the above-mentioned benefits over the other resources, the wind power has shown a considerable growth in the past decade [11]. The technological advancement has improved the reliability and the capacity of the wind turbines in addition to the reduction in the unit cost of power production [12].

A basic wind energy conversion system consists of a wind turbine, an electric generator, power lines and loads as shown in the Fig. 2.1. Based on the turbine spin, the wind turbines can be categorized into two types; horizontal wind turbines and vertical wind turbines. A horizontal wind turbine is the most common style of wind

turbines in which the turbine spins on the horizontal axis, whereas in the vertical wind turbine the main

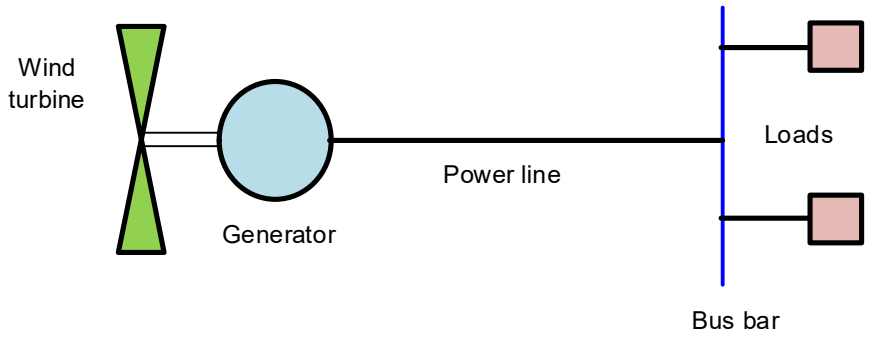

Figure 2.1 A basic wind energy conversion system

rotor shaft is placed vertically. The grid-connected wind farms are mainly of the horizontal wind turbine type [12]. These wind turbines can further be classified as fixed and variable speed types. In the fixed speed wind turbines, a rotor is coupled with the generator, and the stator winding is directly connected to the grid. The examples of the fixed speed wind turbines are found in the squirrel cage induction generator (SCIG) and wound rotor induction generator coupled wind farms. The fixed speed turbines have a simple construction and are comparatively cheaper; however, they are incapable of tracking fluctuating wind speed. On the contrary, the variable speed wind turbines can operate at variable speeds at fluctuating winds so as to maximize the energy capture for the wind source. In spite of that, they require a complex power electronics converter and are expensive as compared to the fixed speed wind turbines [13]. In the variable speed wind turbines, the DFIG-based generator, permanent magnet synchronous generator and wound rotor synchronous generator are used. Among them, the variable speed wind technology using the DFIG-based generator is the popular wind technology today. For this thesis, variable speed wind turbine technology based on the DFIG-based generator is considered for the stability analysis.

2.2 Stability impact of wind power penetration

Wind power is one of the leading renewable resources being utilized for electricity generation all over the world due to its technological and economic superiority over the rest of the renewable resources [14]. Apart from that, the wind integration has

already given beneficial impacts by cutting off carbon emissions from electricity production and reducing the operational costs of the power system. Additionally, the wind power integrated into power networks also adds the capacity value to the power system. In the technical sense, there is no limitation to wind integration; however, such integrations should not reduce the reliability, and must guarantee the stability of the power system [15]. Even though, a power system is designed to withstand a wide range of disturbances, small and large, the dynamic behaviour of such power system is determined by the behaviour and the interaction of the generators existing there, including the wind generators [16-17].

Till date, the majority of the wind farms are based on the constant speed technology due to the simplicity in its design, low cost, and robustness. Even so, in the recent years, the variable speed wind turbines have gained more attention due to their ability of to capture maximum wind power, the capability of operating smoothly, and the superiority in their control. More importantly, the speed of variable speed wind turbines can be controlled to extract more energy as compared to the fixed speed SCIG [18]. It is imperative to understand how these technologies impact on the power system stability, especially at the higher penetration levels so as to enable higher wind integrations. In the wind farm integrated power system, the frequency and damping of oscillatory modes depend on the technology of the wind turbine used, the fixed wind turbine or variable speed wind turbine. The variable speed wind turbines have a higher capability to improve the stability and power quality of the power system [19]. In addition to that, such variable speed wind turbines can provide reactive power support and voltage control when required in the power networks [20]. These types of wind turbines use power electronic converter to decouple voltages and frequencies of the generation with that of the grid [21]. In the construction terms, they are equipped with an induction generator or a synchronous generator connected through a power converter [22]. Such type of wind turbines, which use DFIGs are more popular among the other wind generators currently employed in the power industries.

Various power system issues, including the small signal stability, need to be considered to integrate more wind farms into power networks. The influence on the stability can defer highly at the different penetration levels. At the small scale of wind power integration, the impact of the wind generators on the power system stability is minimal. Despite that, as the penetration level increases, they could influence the dynamic performance of the power networks, especially at the higher penetration

levels. According to [23], the increasing level of wind power penetration on the conventional power system may significantly affect the small signal power system dynamics and operational characteristics. In reality, the current penetration level of wind power has already modified power system behaviour including the stability [24]. The increased wind power penetration can increase low frequency oscillations in the power networks. Depending on the location and the scale of power generation from the wind farms, the power flow in the network changes considerably influencing the damping characteristics of the power system. As the electromechanical interactions and the behaviour of the generators determine the power system stability, the wind power's influence on the power networks is a vital issue of the modern power system. This stability issue is even more pronounced due to the interconnection of power systems, and their expansion over a large geographical area, therefore, maintaining the power system operation following small disturbances has become a challenging issue for the system operation [25]. As a result, the network reliability and the security can be challenging to maintain if the wind power integration and their higher penetrations are not assessed and appropriately managed [26-27].

When the wind power is integrated, the effective inertia of the power system is reduced, which in turn, might jeopardize the power system stability [28]. The impact on the low frequency oscillatory modes can be either detrimental or beneficial with the change in the system inertia [29]. Therefore, it's imperative to understand the stability concerns of the wind penetrations. In real terms, the electromechanical modes of oscillations, their amplitudes and frequencies are dependent on the total system inertia and synchronizing power in the power system. At the higher system inertia, the power system becomes more robust and exhibit more stability under disturbances. However, the high level of wind power penetration might affect the stability as it does not contribute to any additional inertia to the power system, it is integrating into [27]. At the high wind penetration, as the effective inertia of the power system is reduced, the reliability following the disturbances is also get impacted [28]. Because of this issue, the increasing penetration of renewable resources-based generations including the wind power has added challenges to planners and engineers for maintaining the reliability and security of the power system. Hence, the issues of the wind integration must be clearly understood and addressed during the planning and designing stages to avoid any financial and technical implications [30].

It is evident that various power system stability issues, including the small signal stability, need to be considered to integrate wind power into power networks, and other problems that require attention are voltage fluctuations, frequency deviations and power quality [31]. It is, therefore, a vital requirement to understand stability apprehensions of the power networks with the integration of wind farms. This understanding would assist power engineers and designers to be ascertained of the issues, and the implementation of the necessary corrective measures would be easier. Coming to the small signal stability issue, according to [24, 32] as the wind turbines are not synchronously connected to the power system, they neither induce new oscillatory modes nor participate in the existing electromechanical oscillations. However, the wind penetration affects the power oscillation damping by three mechanisms [29].

- Replacing synchronous generators that are involved in oscillations. Hence, affecting the electromechanical modes.
- Wind turbine generator controllers interacting with the synchronous generators, thereby, partially influencing the damping torques.
- Altering the dispatch of the conventional generation and power flow profile, thereby, influencing the power system damping.

Further to this point, the literature search demonstrates that several researchers have studied and contributed to the study of the stability impacts of wind penetrations in the power networks. In [20], the dynamic performance of the DFIG-based wind farms and their effect on electromechanical oscillations have been analysed. While [33] has studied the probabilistic small signal stability analysis considering the uncertainty of wind generation. However, there is no generalization on the view of the researchers about the impacts of the variable speed wind technologies on the small signal stability issues. Ref. [16, 34-36] have mentioned that the high penetration of the DFIG-based wind farm can improve the small signal stability of the power system. In reality, such improvement in the small signal stability is dependent on the location of the wind farms [37]. However, as mentioned in [38] the enhancement in the small signal stability due to the wind power integration is irrespective of the location of the wind farms. While some researchers argue that the DFIG-based wind farm decreases the damping of power oscillations, hence, increases the instability in the power networks [39]. This decrease in the stability is due to the fact that the increased wind power

penetration decreases the overall damping torque by replacing the torque provided by the existing synchronous generators.

There is no consensus on the stability impact of wind penetration. Some researchers present that it has both beneficial and detrimental impacts depending on the operating conditions of the farms in the network. The effect of the increased penetration of a DFIG-based wind farm on the electromechanical oscillations is a complex phenomenon. A DFIG-based wind farm at a weak power network, interconnected to the infinite bus, shows increased frequency and damping of the inter-area oscillations [20]. However, the impact of the DFIG-based wind farm, in its voltage control mode of operation, is dependent on the parameters used and can have a detrimental effect on the damping of the power oscillations. Ref. [39], based on their study about the interaction of a DFIG-based wind farm with the electromechanical modes of the synchronous generator, has shown that the wind farm can decrease damping of the electromechanical oscillations. However, they further concluded that an adjustment in the wind farm controller could improve the damping of such oscillations. Similarly, [40] points out that increased penetration of a DFIG-based wind farm has both beneficial and detrimental impacts on the power system stability. They also found that certain inter-area modes are detrimentally affected by the increased wind penetration. Some argue that wind integration has no beneficial impact on the power system stability, and mention that such integrations influence the power system stability in a negative way leading towards a more unstable region of operation. According to [41], the DFIG-based wind farm can change shapes of local and inter-area modes resulting in a dynamically unstable behaviour. Furthermore, [42] mentions that the increased wind penetration leads to congestion at the weak links, subsequently leading to reduced damping of power oscillations. These line of thought is further supported by the study of [23], which states that an increase in the penetration of wind power increases the probability of the power system becoming unstable. Hence, as per these research works, the penetration of the variable speed wind power threatens the small signal stability of the power system. On the contrary to the arguments mentioned above, the study conducted by [43] found that the inter-area modes are unaffected by the increase in wind penetration.

In addition to the small signal stability study, literature survey also shows the study regarding the transient behaviour of the wind farm connected power system. The power system security and the transient stability of the power system with the large

wind power penetration are issues to be concerned of [44]. With the high integration of wind power, the characteristics of the power network may be modified which results in a change in the power system's response to the sudden transient disturbances. In addition to this, wind power intermittency also affects the transient stability response depending on the operating conditions of the wind farms [45]. Ref. [46] has proposed a topology to provide transient stability improvement of a small scale wind farm comprising of fixed and variable speed wind turbines. Wind farm location also can affect the transient stability, especially when the penetration level is high. A large scale wind farm located in a particularly weak area can highly modify power flows, reduce critical fault clearing times, and may require additional lines for power evacuation.

Apart from the location, wind generator technologies might influence the transient stability aspects of the power system [47]. Thereby, it is important to study the influence of the integrated wind power technologies and their penetration levels on the transient response of the power system. Ref. [48] has studied the transient behaviour and transient stability evaluation methods of a grid-fed wind turbine with a SCIG-based generator. The variable speed wind turbines including the DFIG-based one can provide some reactive support during transient disturbances as compared to the fixed speed wind turbines, thereby, enhancing the transient response of the power system. An appropriate operation and control of the pulse width modulation-based converters help such variable wind farms to ride through the faults. As a result, there exist no issues of the angular stability as seems to be associated with the synchronous generators [49]. The power network with the DFIG-based wind farms even could restore powers and voltages after a grid faults [50], thereby, enhancing the short term stability issues associated with the conventional generators. This arrangement keeps torque equilibrium, maintains the transient stability margin, and gives less speed deviation. As a result, there exists a better ability to control the network behaviour [51]. Besides, reactive devices such as SVC, static compensator (STATCOM), capacitor banks, etc. could provide supplementary reactive support during transient conditions. At the distribution level, the penetration of wind power also affects the transient stability, especially when the active power output reaches the limit. As a result, the power system may go to instability during fault conditions [52].

In the network impact study of the wind penetration, the voltage stability is one of the major issues requiring special attention. The voltage issues could be a short-term voltage fluctuation including flickers, and long-term voltage variations that are

experienced in the wider network [53]. The wind integration might cause problems in the voltage and frequency regulation, reactive power support, power quality, and protection systems [54]. Different wind technologies can have different impacts on the network voltage stability. The fixed speed wind turbine demands reactive power support whereas the variable speed wind turbine can provide such support without any additional reactive compensations [55]. Due to the reactive power regulation capability, the DFIG-based wind farms have better transient voltage stability characteristics and voltage recovery performance than the induction generator-based wind farms, even though, the voltage control capability of the DFIGs is not as comparable as the synchronous generators [56].

Due to the recent rapid growth in the small-sized DFIG-based wind farms, the reactive power control capability of such wind farms can be utilized as a continuous reactive power source to support the voltage control capability of the distribution network, as when needed [57]. Hence, an appropriate level of wind power penetration from the DFIG-based wind farm can improve the voltage profile of all buses as well as the maximum loading margins, thereby, enhancing the voltage stability of the radial distribution system [58]. Additionally, at the fault conditions, the DFIG-based wind farm provides voltage control capability with its ability to re-establish the desired voltage level [59]. However, such support may be dependent on the operating modes of the wind farm. At the voltage control mode, the DFIG-based wind farm shows better improvement and can mitigate the voltage rise effect as compared to the power factor control mode of its operation [60].

According to [61], a large-scale DFIG-based wind farm can be connected to both distribution and transmission level voltage buses without degrading the voltage stability. However, when the voltage control requirement exceeds the capability of the wind turbine, the voltage stability becomes an issue [56]. The adverse effect on the system voltage stability can be reduced by connecting the wind farm at the higher voltage levels and closer to the load centre, which in turn, minimizes the requirement of reactive compensation for the wind integration [62]. In reality, due to the favorable wind conditions, wind farms are mostly exploited in the remote areas, where the electricity network is relatively weaker. As a result, this situation brings challenges for the voltage control and reactive power compensation in the network. In such scenarios, the additional reactive power support devices can be integrated to enhance the voltage stability limit in order to support increased wind penetration. However, in the

interconnected power system, the additional voltage control device can influence the damping of the oscillatory modes positively or negatively [63]. Therefore, care must be taken at the design and planning phase for accurately optimizing the power system and its components.

2.3 Small signal stability

Small signal stability indicates the capability of a power system to remain in the synchronous operating state following small disturbances. Inability to remain in such condition occurs either due to the lack of sufficient synchronizing torque resulting in a steady rise in rotor angle or due to the lack of sufficient damping torque resulting in rotor oscillations of increasing amplitude. It is a well-known fact that the power system responds to the small disturbances is a complex phenomenon, and depends on many factors like initial operating condition, system strength, and generator excitation controls, etc. [9]. For the study purposes, such small disturbances are considered to be sufficiently small that the linearization of the power system equations is permissible for mathematical analysis and interpretation [10].

Small disturbances might cause low frequency oscillations in power system by gradual variations in the loads, generations and actions of control devices. Such oscillations are power system characteristics and are acceptable as long as they decay without causing the small signal instability in the power network [64]. Electric utilities mostly experience small signal stability problems related to insufficient damping of low frequency oscillations in their real power networks. Hence, the instability is generally due to oscillations of increasing amplitude. Such power system stability problems might either be local or global in nature, and are of the following types [65].

Intraplant modes: These modes are associated with the swinging of the machines of the same power generation site against each other. The frequency range of such oscillations is 2.0-3.0 Hz depending upon their unit ratings and the reactance connecting the units. Such oscillations are local to the site, as a result, the rest of the power system remains unaffected.

Local modes: Local oscillations mean the swinging of a single power plant against the rest of the power system and are also called local plant mode oscillations. These oscillations are localized to the generator and the line connected to the grid. The frequency range of such oscillations is observed between 1.0-2.0 Hz. The damping and

oscillatory frequencies depend upon the machine output and the impedance between the machine terminal and the infinite bus bar.

Interarea modes: These modes are associated with the swinging of a group of generators in one area against a group of generators in another area, generally connected through a weak transmission line. Such oscillations are called interarea mode oscillations and are observed over a large portion of the power network. These modes exhibit oscillations of a frequency range of 0.1-1.0 Hz. This is a complex phenomenon and is dictated by the network structure, tie-line strength, nature of loads, power transfer through tie lines, etc.

Control modes: These modes are caused by poorly tuned power system controllers such as exciters, HVDC converters, SVC, and governors etc.

Torsional modes: These modes are associated with the turbine generator shaft system. The interactions with excitation controls, speed governors etc. cause oscillations of this nature. The frequency of such oscillations is in the range of 10-46 Hz.

Local and inter-area modes of oscillations are known as the low frequency electromechanical oscillations. In secured operations, these oscillations are decayed within the adopted time period, returning power system in a stable and reliable operating condition. However, sustained oscillations of such nature could lead to system separations and possible outages to a considerable number of customers [25]. Power system outages due to the loss of small signal stability have occurred around the world. The incidents of such system outages due to inter-area oscillations include [25, 65].

- Detroit Edison-Ontario Hydro-Hydro Quebec, 1960s, 1985.
- Finland-Sweden-Norway-Denmark, 1960s.
- Saskatchewan-Manitoba Hydro-Western Ontario, 1966.
- Western Electric Coordinating Council, 1964, 1996.
- Italy-Yugoslavia-Austria, 1971-1974.
- South East Australia, 1975.
- Scotland-England, 1978.
- Western Australia, 1982, 1983.
- Taiwan, 1985.
- China, 2003.
- Italy, 2003.

- Yunan and Guizhou provincial grid, 2006, 2007, 2008.

These incidents outline how important it is to understand and manage such oscillations for the secure and reliable operation of the power network.

2.4 Transient stability

Transient stability of a power system refers to the ability of the power system in maintaining synchronism after sudden severe transient disturbances. These responses involve a large excursion of rotor angles, power flows, bus voltages, and other system variables. A power system is stable if the resulting angular separation between the machines comes within an acceptable bound in a specified time. In a complex practical power system, the transient stability analysis is performed by time domain simulations, in which nonlinear differential equations are solved using step by step numerical integration techniques. In such a power network, usually, the response to a large disturbance is followed by the isolation of the faulty element by the protective relaying system. So, the bus voltages, line flows, and performance of protection schemes are of interest in the transient stability study. The transient stability of the generators in a power system depends upon the following factors [9].

- Generator loading.
- The power output of the generator during the transient fault.
- Fault location and type.
- Fault-clearing time.
- Post-fault system reactance.
- Generator reactance.
- Generator inertia.
- Generator internal voltage. Hence, field excitation.

Transient stability can be enhanced by many methods such as reducing fault clearing time, reducing system reactance, installing shunt compensation, etc. Faster a fault is cleared, lesser would be the kinetic energy gained by the generator during the fault duration. Thus, faster fault clearing can reduce resulting disturbances. Additionally, the series reactance of the power system network is the determinant of the transient stability limit. Reduction in the series reactance increases post-fault synchronizing power transfer, thereby, improving the transient stability. As shunt compensation can

support voltages at different buses, which as a result, can increase the flow of synchronizing power among the generators [9].

Integration of wind power should not compromise the transient stability of the power system. Transient stability issues of the wind power integration should be understood during the planning and integration studies which are performed through the time domain simulations.

2.5 Voltage stability

Voltage stability refers to the ability of a power system to retain acceptable voltages at all the buses at normal operating conditions and after disturbances. Voltage instability condition arises when a disturbance leads to an uncontrolled decline of the voltages in network buses due to the inability of the power system to meet demands for reactive power. Voltage stability analysis involves the examination of two aspects i.e., the proximity to the voltage instability and the mechanism of the voltage instability. Proximity gives closeness of the power system to the voltage instability, whereas mechanism covers how and why such instability occurs, what are the key factors contributing to the instability, where are the voltage weak areas in the network, and what are the effective measures to improve the voltage instability [9]. Mainly weak systems, long lines, and heavier loading zones are prone to the voltage instability due to reactive power mismatches.

Voltage stability can be studied by classifying into two categories: small disturbance and large disturbance voltage stability. Small disturbance voltage stability controls bus voltages following small disturbances. Such stability issues can be studied with the steady state approaches such as linearizing system dynamic equations at a given operating point. Large disturbance voltage stability refers to the system voltage control following large disturbances and can be studied using time-domain simulations. Conventionally, the steady state voltage stability analysis is determined using active power-voltage and reactive power-voltage curves at the selected load buses [9]. The active power-voltage curve is a plot of bus voltage as a function of active power for a specified power factor. However, the reactive power-voltage curve shows the relation between reactive power and receiving end voltage for different values of active power [66]. These methods might not always be appropriate to analyse the voltage stability in a large complex power system. Thereby, the voltage stability analysis of large power

networks can be computed using the modal analysis technique. With this method, a specified number of the smallest eigenvalues and their associated eigenvectors are calculated. The magnitude of the eigenvalues provides a relative measure of the proximity to the voltage instability. Participation factor gives the contribution of the mode to the reactive power-voltage sensitivity at the selected bus. For a small eigenvalue, the bus participation factor analysis determines the closeness of that bus to the voltage instability [67].

Power system needs to be securely designed and operated to prevent voltage collapse. In the voltage collapse condition, voltage reduces to an unacceptably low level in a significant part of the power system [9]. Low voltage profiles, heavy reactive power flows, inadequate reactive power support, and heavily loaded lines are the main symptoms of voltage collapse. The voltage collapse mitigating schemes need to use those symptoms to diagnose the approach of collapse, and necessary actions are to be initiated promptly in order to prevent the collapse [68]. The following measures can be taken in order to avoid the power system from such collapse [9].

1. System design measures
- Application of reactive power compensators
- Network and generator reactive output control
- Proper coordination of protections and controls
- Control of transformer tap changers
- Under voltage load shedding

2. System operating measures
- Stability margin
- Spinning reserve
- Operators' action

Modern distribution networks are active due to the integration of renewable resources, battery storage systems and reactive power compensating devices. Additionally, such networks might be extended and stressed due to the remotely connected large commercial loads. In such distribution systems, the voltage stability is a significant concern from planning and operation perspectives. Remote wind farms connected to such a weak distribution network through a long line could adversely affect the voltage stability. To be specific of these type of scenarios, in countries like Australia large mining loads, agro farms, etc. are generally located far from the distribution load

center. When a wind farm is integrated at the end of such distribution feeder, with large motor loads and other residential customers, the steady state and transient voltage stability of the respective power network should not be compromised. Thereby, the impact of the wind farms on the voltage stability of a distribution system needs to be studied to identify their effects on the existing network and customers.

Notably, large induction motors, as a distribution load, can consume a significant amount of reactive power upon network disturbances, thereby, negatively influencing fault recovery by pushing the distribution system voltages to an unusually low level [69]. Several researchers have studied the voltage stability issues in the distribution system with the wind farms. Ref. [70] has presented a methodology for calculating annual voltage profile and slow voltage variations of a distribution system with wind power. The study indicates an improvement in the voltage profiles with the wind integration. According to [71], the voltage stability of a power system during small and large disturbances can be improved with wind power integration, especially when combined with reactive power compensation devices. Ref. [72-73] have presented methods for finding a steady-state voltage stability region for each distribution bus with wind power generators. Both the papers have determined the maximum permissible load in each bus of their distribution networks within the voltage limit allowed by the utilities.

Many researchers have presented that the voltage stability impact of wind power integration depends on the type of wind technology realized for power production. Ref. [50] has observed that the variable speed wind technologies such as the inverter coupled permanent magnet synchronous generator and DFIG can restore voltage and power following a grid fault with a quicker restoration in the wind farm. Ref. [74] has presented a reactive power margin based var planning for improving dynamic voltage stability of a distribution system with an induction generator-based wind farm. Authors have shown that their approach can reduce power losses and improve voltage regulation of the distribution system. Similarly, ref. [75] has studied voltage stability and grid-loss related issues of a distribution system with DFIG-based wind farm for heavily unbalanced loading conditions. The study shows that multiple small-DFIG systems could provide higher system voltage improvement but exhibits similar grid loss reduction in comparison to a single large-DFIG system. Likewise, coordinated control of small wind turbines in a large wind farm can maintain a constant voltage at

the connecting bus irrespective of the variation in the power production from the turbines [76].

However, some other researchers have presented strategies for mixing both technologies, the fixed and variable speed ones, for better voltage stability scenario in the distribution network. Ref. [46] have presented a control strategy for a small wind farm with fixed and variable speed wind turbines to minimize voltage fluctuation and to improve the transient stability of the network. With this strategy, the variable speed wind turbines using DFIG support fixed speed wind turbines using induction generator with the reactive power during disturbances, thereby, improving the stability.

2.6 Control of power system oscillations

Oscillations in the power system are the result of the lack of damping torques in generator rotors, which causes oscillations of other power system variables like bus voltages, frequency, and power flows, etc. These types of oscillations generally exhibit low damping performance [77] and are usually in the range of 0.1 to 2 Hz. The oscillatory instabilities due to the mode oscillations are undesirable; thereby, acceptable damping can be achieved using various controllers such as the power system stabilizers, SVC, STATCOM, etc. [78]. In an interconnected power system, such poorly damped oscillations restrict power transfer and system security limits. As a result of which, this issue is considered as one of the main problems in the power system stability [79]. There are many approaches to improving the damping of such oscillations. Among them, the use of power system stabilizers is the most cost-effective method. However, they have limited capability in damping of inter-area oscillations. Likewise, flexible ac transmission system (FACTS) devices can provide damping to such electromechanical oscillations in addition to their function of balancing reactive power [80]. Because of which, different types of FACTS devices are deployed in power networks. Ref. [81] has proposed a control strategy to enhance damping control of the FACTS devices connected near a wind farm. According to [82], a controller can be designed to allow the wind farm to inject out of phase power to increase damping of interarea oscillations. Besides, HVDC links and energy storage systems with damping controllers have been developed to mitigate inter-area oscillations over the past decades. Such controllers must cover numerous power swing modes over a wide range of operation for secure power system operation [83].

Wind farms are generally located in remote locations for better wind conditions; therefore, for the evacuation of power from a large wind farm through a long line, the line might be series-compensated [84]. Series compensation can be achieved by using capacitor banks or series FACTS devices. The series FACTS devices can be utilized in damping oscillatory modes in the power system [85]. They are beneficial for improving power system dynamics with an effective damping of large and small signal disturbances. Additionally, they can support during transient conditions and improve transmission capability of the tie line for a long distance evacuation of a large scale wind power. A varying degree of series compensation can be utilized for controlling power flow in the line and for improving such stability issues. Ref. [86] have analysed the impact of a fixed series compensation on evacuating large scale wind power construction plan of Gansu Province in China. Based on the study, it is concluded that the fixed series compensation would significantly increase the power transmission capability. However, based on their study of the stability of the DFIG-based wind farm connected through a series compensated line, [30] advocates that the parameter of the rotor-side current control scheme, influence the power system stability.

The FACTS devices are used to enhance flexible power flow control in the power system. A static synchronous series compensator (SSSC), a series FACTS device, is a voltage-source converter-based series compensator, which can inject a voltage in quadrature with the line current providing the same compensation as provided by a conventional series capacitor. It can maintain a constant compensating voltage in the variable line current, or control the amplitude of the injected voltage independent of the amplitude of the line current. The use of the FACTS-based series compensation, such as SSSC, can increase power transfer through the line and provide an improvement in the transient stability limit [87]. An SSSC controller can effectively damp a range of oscillations originated from the small disturbances [88]. However, at a given series compensation level, the system stability margin is reduced with the increase in X/R ratio. In which, X and R respectively represent reactance and resistance of the compensated line. Therefore, the stability of a DFIG-based wind farm is of significant concern, when evacuating wind power through a high voltage and extra high voltage transmission line, as such lines have large X/R ratios [30].

Apart from the series FACTS devices, the shunt FACTS devices can also be implemented to improve the dynamic stability as well as for the voltage support to the power network. Such voltage support can be achieved during the steady state as well

as following transient conditions. According to [89-90], the FACTS-based shunt controllers such as SVC, STATCOM, etc. can provide continuously varying susceptance and fast response to control voltages and reactive powers. Appropriately located shunt controllers can effectively damp low frequency oscillatory modes for the stability improvement [80]. When a DFIG-based wind farm is integrated with such shunt devices, they provide reactive support to the wind farm and assist maintaining a better voltage profile irrespective of the variation in wind speed [91]. More importantly, such shunt devices dynamically support voltages at the key points in a power network, improving the transient stability and supporting increased oscillation damping. According to [92], a properly placed STATCOM controller with a supplementary damping control system can further enhance the damping of the power system oscillations. Similarly, SVCs are also used to maintain bus voltages and to enhance damping of such oscillations. Additionally, SVCs controlled by some auxiliary signals can also provide additional damping similar to STATCOM [93]. However, their effectiveness depends on their location in the network. Yet, ref. [94], based on their study on the damping performance of the induction generator connected power system, concludes that SVC has both detrimental and beneficial impacts depending on the operating circumstances of the device and the network.

According to [77], in order to further enhance the damping performance capability of a shunt power compensating device, a supplementary controller can be incorporated, which is referred to as power oscillation damping controller. Additionally, selection of the input signal plays a significant role in stabilizing ability of such shunt devices. In a multi-machine power system, selection of an effective installing location and feedback signal is the most important initial decisions on designing a FACTS-based stabilizer [95]. Literature has reported various methods to determine a suitable location and feedback signal selection for developing such damping controllers [9, 64]. From the voltage stability enhancement perspective, the modal analysis technique is proposed to find the best location for the shunt controllers [67], and residue method is proposed for the small signal stability enhancement [96]. In [97], the buses having higher participation to the weakest mode of voltage instability are recommended as the candidate buses for the shunt controllers, and among the buses which give a minimum shift to the real part of the critical mode are selected for the controller placement. Ref. [78, 98-99] have designed damping controllers to enhance damping of the critical modes in the distribution network with embedded distributed generators. In [99], a

capacitor bank has been selected for the application of a controller, based on the controllability factor of the critical modes in a distribution network.

For the selection of the controller's input signal, local signals are always preferred in order to avoid the additional communication related cost associated with the global signals. The signals like line power, line current magnitude, bus voltage magnitude, etc. are considered as the candidate signals [100]. Different works of literature have proposed various methods for the selection of such control signals. Residue method is the most common method and is very useful for simple controllers [9]. This method can be used for selecting an input signal for the controllers from the locally available signals. In [101], the relative gain array analysis approach, and residue analysis method are utilized, and the paper has proposed a hybrid method to find suitable control signals for the multiple wide-area damping control associated to the HVDC and FACTS devices.

Similarly, in [102], the minimum singular value, right-half plane zeros, relative gain array method, and Hankel singular values are used as the methods for selecting the control signals. In [103], the power oscillation damping controllers are designed using residue method and linear matrix inequalities method to demonstrate the contribution of a wind farm on power oscillation damping. Similarly, wide area power oscillation damping controllers have been designed using an observer-based state-feedback approach to achieve coordinated control of variable speed wind farms [104]. In [78], a method to design a controller for a photovoltaic generator, for enhancing damping of a critical mode, in a renewable energy-based distribution system has been proposed. In [98], a robust coordinated damping controller has been designed based on H_∞ robust stabilization technique to enhance damping of the critical modes in the distribution system. The input signal for the controller is selected from the local signals based on the residue method.

With the increase in wind integration in the power system over the years, the effect on the stability of the power system with HVDC link requires consideration, especially at the high penetration of wind power. Different works of literature have lauded the effectiveness of the HVDC technology for the stability benefits of the power network. The transmission of a large amount of power over a long line corridor can cause load flow problem and poor damping of the low frequency inter-area oscillations. Therefore, it's a challenge to increase both the transmission capability and flexibility in a power grid with the conventional ac options. An HVDC system in ac network aids

to enhance power system stability, improve voltage stability and independently control active and reactive power flows [105] Ref. [106] has studied the impact of HVDC on the power system stability and proposed a mechanism to enhance such stability. Likewise, [107] has examined the advantages of the HVDC technology in improving the power system stability. The HVDC link is highly controllable, and this characteristic can be utilized to enhance the stability of the interconnected power system for the small signal stability enhancement as well as under severe transient disturbances [9].

Ref. [108] addresses that a fast power modulation can be utilized in the HVDC system to improve power stability with the different type of controllers and control signals. Furthermore to this, a proper control mechanism designed and incorporated in the power system with an HVDC link can considerably improve the system stability [106]. Similar to FACTS devices, the HVDC line can influence power system stability at the high penetration of wind power. According to [109-111], an HVDC system can be an effective and reliable solution for the evacuation of a large scale power from a distant offshore wind farm. Additionally, an HVDC link with a damping controller can provide further damping enhancement and power fluctuation mitigation of a DFIG-based offshore wind farm [112].

2.7 Stability of a microgrid

Commitment to move towards environmental friendly power generation from most of the developed countries and deregulation in power utilities have boosted the rapid advancement of distributed generation units in power sector [113], enabling dissociation of conventional power networks to form smaller power grids, referred to as microgrids. Microgrids are clusters of distributed generators, energy storing devices and electrical loads, and have a capability of operating in islanded and grid-connected states [114]. The distributed generators can be conventional inertia-based generators or converter-interfaced resources like photovoltaic systems and wind turbines. Microgrids can run permanently in an islanded mode (when a utility feeder does not exist) or for a limited period (because of a fault or scheduled/unscheduled maintenance in the grid) [115]. Operation and control of islanded microgrids is more sophisticated due to the lack of network support from the power grid, and consequently, the

frequency and voltage values of the buses have to be maintained within their specified limits by its dispatchable distributed generators [116-118].

The penetration of converter-interfaced renewable resources has been increasing due to progression in renewable energy technologies. In contrary to the conventional inertia-based synchronous generators, such as diesel, gas or hydro-driven ones, that are equipped with suitable excitation and governors, the converter-based non-inertial distributed generators are managed by smart control schemes that enable rapid and flexible control of active and reactive power flows [119]. By increasing the penetration of converter-based distributed generators or replacing conventional ones with the converter-based ones, the microgrids start observing lower equivalent system inertia and are therefore becoming more susceptible to stability issues. Thus, even a minor disturbance, for example, load switching and a slight deviation in the output power of distributed generators might cause severe voltage and frequency fluctuations or system instability [120].

The stability of microgrids depends on their micro-resources, energy storages, network topologies, and control strategies [121]. Converter-based distributed generators are efficient, reliable and controlled precisely; however, their predominance might have a negative influence on the microgrids' stability. They potentially make microgrids more susceptible to power oscillations during faults, depending on the control strategy of the power converter at the microgrid interface [122]. On the other hand, synchronous generators support the microgrids in frequency and voltage stabilization and help to boost stability [123]. With smart power management strategies, energy storage devices can store or release power to sustain instantaneous power supply/demand equilibrium, which is equivalent to an increase in overall inertia in the microgrid [124].

The stability issues in microgrids are well noted and have been researched in the past [121]. To this end, a power grid's small signal stability analysis with the numerous interconnected synchronous generators is extended to microgrid studies. Ref. [125-128] have used various approaches such as eigenvalue, gain-phase margin criterion, frequency-response, as well as singular entropy and matrix pencil to evaluate the dynamic stability of converter-based microgrids while [129] reviews techniques such as dynamic phasors, reduced-order, rotating direct-quadrature (dq) frame and harmonic linearization. Likewise, [121] reviews various small signal stability analysis approach implemented in grid-connected and isolated microgrids on top of transient and voltage stabilities. According to [130], in a microgrid environment, DFIG-based

wind farm increases negative real components and damping ratio of critical modes associated with the wind turbine, thus improving the small signal stability.

In an eigenvalue-oriented technique, the microgrid will be expressed by a set of state-space equations, and its equivalent overall state matrix needs to be formulated and used to determine its eigenvalues [125]. This technique is used by [121-122, 125, 129, 131-136] to analyse the small signal stability of a microgrid with converter-based distributed generators while [120, 137-139] have focused on microgrids also including inertial distributed generators. Ref. [138, 140-141] have considered the internal dynamics of the renewable sources in the small signal stability analysis while [142-143] uses a reduced order technique to neglect the internal dynamics of the converters and the filters respectively. Besides, [144-150] respectively take into account the effect of constant power and induction motor type loads, energy storage systems, the uncertainty of renewable resources, ramp rates of distributed generators, communication delays and resonance in converters in microgrid stability studies.

It is observed from the literature survey that, several studies have been carried out to understand the stability of power system at different penetration levels of wind power. However, the correlation between the power system components and such penetrations has not been explored in details. Thus, this research contributes to identifying the impact of the correlation between the power system components and network parameters on the stability of power systems and microgrids at different penetration levels of wind power.

2.8 Summary

Growing awareness towards global warming has caused a rapid rise in the exploitation of the renewables. Wind energy is the most popular of the renewable energy resources due to the advancement in wind technologies and power electronics which enables a utility scale power production. At the small penetration levels of wind integration, the stability impacts might not be significant enough to be considered as a significant issue. However, at the higher penetration levels, the wind power exhibits substantial effect to the power system, thereby, this issue is to be understood entirely to maintain the power stability to an acceptable limit. The small signal, transient as well as voltage stability issues need to be examined and addressed to allow a further increase in wind penetration from the current levels.

The stability impact of the wind power depends upon the technology of the wind generators. Literature survey shows that the HVDC line, FACTS-based devices, and the supplementary controllers are observed to be positively influencing the stability of a wind farm connected power system. Additionally, at the microgrid level, an increase in the penetration of the inertia-less generators lowers system inertia, thereby, increasing proneness to the instability.

Chapter 3 Modelling and analysis of power system components

This chapter presents modelling of power system components such as a conventional synchronous generator, DFIG-based wind generator, loads, FACTS devices, HVDC link, and power oscillation damping controller. A detailed mathematical explanation of those power system components has been developed for the stability studies in this thesis. Additionally, the investigation of the power system stability is also discussed and presented here. This chapter also covers a detail small signal modelling of the microgrid building components such as a synchronous generator, a converter based distributed resource, battery energy storage system, lines and loads.

3.1 Generators

This section provides mathematical equations of the generators considered for the stability studies. However, the power sources for the microgrid scenario are covered in the section 3.6 Construction and operation of a microgrid components. The generators considered here are the conventional synchronous generator, and DFIG-based wind generator.

3.1.1 Synchronous generator

Conventionally, the synchronous generators are the main source of energy generation in the power system. In addition to the active power, it can be operated for providing reactive power support for controlling voltage. The sixth order model of the synchronous generator is used for the stability study excepting the microgrids and

assumes the presence of field winding and damper windings. The following equations represent the synchronous machine model for the stability analysis [151].

$$\dot{\delta} = \omega_{\mathrm{b}}(\omega - 1) \tag{3.1}$$

$$\dot{\omega} = \left(P_{\mathrm{m}} - P_{\mathrm{e}} - D(\omega - 1)\right)/M \tag{3.2}$$

$$\dot{e}'_{\mathrm{q}} = \left(-e'_{\mathrm{q}} - \left(x_{\mathrm{d}} - x'_{\mathrm{d}} - \frac{T''_{\mathrm{d0}}}{T'_{\mathrm{d0}}}\frac{x''_{\mathrm{d}}}{x'_{\mathrm{d}}}(x_{\mathrm{d}} - x'_{\mathrm{d}})\right) i_{\mathrm{d}} + \left(1 - \frac{T_{\mathrm{AA}}}{T'_{\mathrm{d0}}}\right) v_{\mathrm{fd}}\right)/T'_{\mathrm{d0}} \tag{3.3}$$

$$\dot{e}'_{\mathrm{d}} = \left(-f_{\mathrm{s}}(e'_{\mathrm{d}}) + \left(x_{\mathrm{q}} - x'_{\mathrm{q}} - \frac{T''_{\mathrm{q0}}}{T'_{\mathrm{q0}}}\frac{x''_{\mathrm{q}}}{x'_{\mathrm{q}}}\left(x_{\mathrm{q}} - x'_{\mathrm{q}}\right)\right) i_{\mathrm{q}}\right)/T'_{\mathrm{q0}} \tag{3.4}$$

$$\dot{e}''_{\mathrm{q}} = \left(-e''_{\mathrm{q}} + e'_{\mathrm{q}} - \left(x'_{\mathrm{d}} - x''_{\mathrm{d}} + \frac{T''_{\mathrm{d0}}}{T'_{\mathrm{d0}}}\frac{x''_{\mathrm{d}}}{x'_{\mathrm{d}}}(x_{\mathrm{d}} - x'_{\mathrm{d}})\right) i_{\mathrm{d}} + \left(\frac{T_{\mathrm{AA}}}{T'_{\mathrm{d0}}}\right) v_{\mathrm{fd}}\right)/T''_{\mathrm{d0}} \tag{3.5}$$

$$\dot{e}''_{\mathrm{d}} = \left(-e''_{\mathrm{d}} + e'_{\mathrm{d}} + \left(x'_{\mathrm{q}} - x''_{\mathrm{q}} + \frac{T''_{\mathrm{q0}}}{T'_{\mathrm{q0}}}\frac{x''_{\mathrm{q}}}{x'_{\mathrm{q}}}\left(x_{\mathrm{q}} - x'_{\mathrm{q}}\right)\right) i_{\mathrm{q}}\right)/T''_{\mathrm{d0}} \tag{3.6}$$

where δ is power angle, ω_{b} is frequency base of fundamental frequency ω, P_{m} is mechanical power, P_{e} is electrical power output, M is mechanical starting time, D is damping coefficient, x_{d} is d-axis synchronous reactance, x'_{d} is d-axis transient reactance, x''_{d} is d-axis sub-transient reactance, x_{q} is q-axis synchronous reactance, x'_{q} is q-axis transient reactance, x''_{q} is q-axis sub-transient reactance, T'_{d0} is d-axis open circuit transient time constant, T''_{d0} is d-axis open circuit sub-transient time constant, T'_{q0} is q-axis open circuit transient time constant, T''_{q0} is q-axis open circuit sub-transient time constant, T_{AA} is d-axis additional leakage time constant, i_{d} is d-axis current, i_{q} is q-axis current, v_{fd} is field voltage, e'_{d} is d-axis transient voltage, e''_{d} is d-axis sub-transient voltage, e'_{q} is q-axis transient voltage, and e''_{q} is q-axis sub-transient voltage.

The output power delivered by the synchronous generator is given by

$$P_{\mathrm{e}} = \left(v_{\mathrm{q}} + r_s i_{\mathrm{q}}\right) i_{\mathrm{q}} + (v_{\mathrm{d}} + r_{\mathrm{s}} i_{\mathrm{d}}) i_{\mathrm{d}} \tag{3.7}$$

where r_{s} is armature resistance, v_{d} is d-axis voltage, and v_{q} is q-axis voltage.

The synchronous machine in its capacity of voltage support device can be controlled to regulate flow of reactive power by controlling the excitation of the machine. For such operation, the machine is also referred to as synchronous condenser. In the over-

excited operation, the machine works as a capacitor producing a leading current whereas in the under-excited operation the same machine operates as a reactor generating a lagging current. In such scenarios, an automatic voltage regulator continuously senses the terminal voltage and adjusts the reactive power output of the condenser to maintain a constant terminal voltage [9].

3.1.2 DFIG-based wind generator

A schematic diagram of the DFIG-based wind generator model is shown in Fig. 3.1. The stator is connected to a balanced three-phase grid, and the rotor side is fed via a back to back pulse width modulation based voltage source inverter with a common DC link. The supply side converter controls the power flow between the DC link and grid whereas the rotor side power converter provides excitation for the machine [152]. The supply side converter operates at grid frequency, whereas, the rotor-side converter at a different frequency depending on the blades speed. The converter is modelled as a current source with the d-axis rotor current and q-axis rotor current as the state variables, and these state variables are used for the rotor speed and voltage control [151]. A dynamic model of the DFIG-based

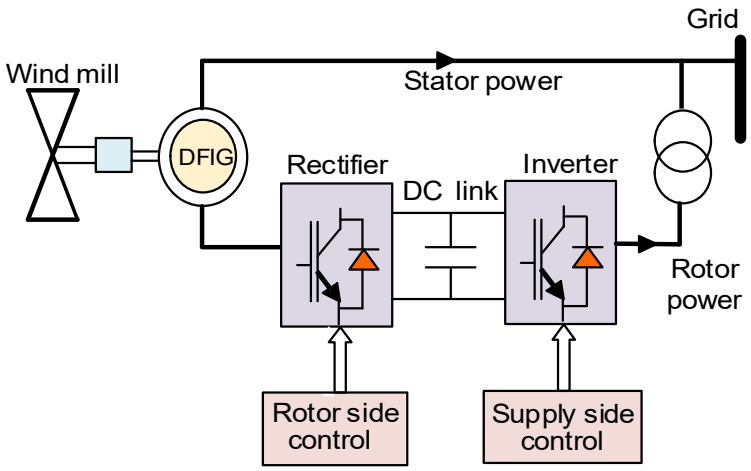

Figure 3.1 Schematic diagram of a DFIG wind turbine

wind generator is made up of the following components: wind speed model, aerodynamic model, pitch angle control model, mechanical drive model, and DFIG model. The wind speed model is composed of four parts: basic wind, gust wind, ramp wind and random wind. An aerodynamic model captures wind energy and converts to

mechanical energy. A mechanical drive model has a low speed shaft, gear box and high-speed shaft [153]. A pitch angle controller adjusts the pitch angle to limit generator's speed to a maximum permitted value. Ref. [154] has studied the equivalent models of wind farms using aggregated wind turbines to represent the collective behaviour on the power system simulations. In this study, wind turbines are aggregated as one equivalent wind turbine. Additionally, wind speed is assumed to be constant during the simulation period of this study.

The performance of wind energy conversion systems depends upon the subsystems such as wind turbine (aerodynamic), gears, and generator [155].

Several components that contribute to the dynamic behaviour of a DFIG are [29]

- Turbine aerodynamics
- Pitch control that controls the mechanical power delivered to the shaft
- Shaft dynamics
- Generator electrical characteristics
- Electrical controls: three controllers are used to provide controls for frequency/active power, voltage/reactive power, and pitch angle mechanical power.

The mechanical power developed by the wind turbine is given by [35]

$$P_{\mathrm{m}} = \frac{\pi \rho r^2}{2} U^3 C_{\mathrm{P}}(\lambda) \tag{3.8}$$

where ρ is air density in m^3, r is the radius of the turbine in m, U is wind speed in m/s, $C_{\mathrm{P}}(\lambda)$ is power coefficient, and λ is tip speed ratio.

The equations of the DFIG generator can be written as [151, 156]

$$v_{\mathrm{ds}} = -r_{\mathrm{S}} i_{\mathrm{d}} + \left((x_{\mathrm{S}} + x_{\mathrm{m}}) i_{\mathrm{q}} + x_{\mathrm{m}} i_{\mathrm{qr}}\right) \tag{3.9a}$$

$$v_{\mathrm{qs}} = -r_{\mathrm{S}} i_{\mathrm{q}} - \left((x_{\mathrm{S}} + x_{\mathrm{m}}) i_{\mathrm{d}} + x_{\mathrm{m}} i_{\mathrm{dr}}\right) \tag{3.9b}$$

$$v_{\mathrm{dr}} = -r_{\mathrm{R}} i_{\mathrm{dr}} + (1-\omega)\left((x_{\mathrm{R}} + x_{\mathrm{m}}) i_{\mathrm{qr}} + x_{\mathrm{m}} i_{\mathrm{q}}\right) \tag{3.9c}$$

$$v_{\mathrm{qr}} = -r_{\mathrm{R}} i_{\mathrm{qr}} - (1-\omega)\left((x_{\mathrm{R}} + x_{\mathrm{m}}) i_{\mathrm{dr}} + x_{\mathrm{m}} i_{\mathrm{d}}\right) \tag{3.9d}$$

where v_{dr}, v_{qr} i_{dr}, and i_{qr} are d and q axis rotor voltages and currents respectively; r_{R}, x_{S} and x_{R} are the rotor resistance, and the stator and rotor reactance respectively; and x_{m} is the magnetizing reactance.

The active and reactive powers injected into the grid depend on the stator currents and grid side currents of the converter as given by

$$P = v_{\mathrm{d}} i_{\mathrm{d}} + v_{\mathrm{q}} i_{\mathrm{q}} + v_{\mathrm{dc}} i_{\mathrm{dc}} + v_{\mathrm{qc}} i_{\mathrm{qc}} \quad (3.10a)$$

$$Q = v_{\mathrm{q}} i_{\mathrm{d}} - v_{\mathrm{d}} i_{\mathrm{q}} + v_{\mathrm{qc}} i_{\mathrm{dc}} - v_{\mathrm{dc}} i_{\mathrm{qc}} \quad (3.10b)$$

where v_{dc}, v_{qc}, i_{dc}, and i_{qc} are d and q axis converter voltages and currents, respectively.

The converter powers on the grid side are

$$P_{\mathrm{c}} = v_{\mathrm{dc}} i_{\mathrm{dc}} + v_{\mathrm{qc}} i_{\mathrm{qc}} \quad (3.11a)$$

$$Q_{\mathrm{c}} = v_{\mathrm{qc}} i_{\mathrm{dc}} - v_{\mathrm{dc}} i_{\mathrm{qc}} \quad (3.11b)$$

whereas on the rotor side, they are

$$P_{\mathrm{r}} = v_{\mathrm{dr}} i_{\mathrm{dr}} + v_{\mathrm{qr}} i_{\mathrm{qr}} \quad (3.12a)$$

$$Q_{\mathrm{r}} = v_{\mathrm{qr}} i_{\mathrm{dr}} - v_{\mathrm{dr}} i_{\mathrm{qr}} \quad (3.12b)$$

Assuming a lossless converter model and unity power factor on the grid side of the converter, one gets

$$P_{\mathrm{c}} = P_{\mathrm{r}} \quad (3.13a)$$

$$Q_{\mathrm{c}} = 0 \quad (3.13b)$$

Therefore, the powers injected in the grid can be calculated as

$$P = v_{\mathrm{d}} i_{\mathrm{d}} + v_{\mathrm{q}} i_{\mathrm{q}} + v_{\mathrm{dr}} i_{\mathrm{dr}} + v_{\mathrm{qr}} i_{\mathrm{qr}} \quad (3.14)$$

$$Q = v_{\mathrm{q}} i_{\mathrm{d}} - v_{\mathrm{d}} i_{\mathrm{q}} \quad (3.15)$$

3.2 HVDC model

An HVDC link consists of two ac/dc converter stations connected by dc line(s) which enables an isolated operation of the two power systems and the bidirectional power transmission to and from the ac power systems. The ability of the HVDC system to rapidly control transmitted power has an impact on the power system stability of the ac systems. The HVDC link can be classified into three categories [9].

- Monopolar link
- Bipolar link
- Homopolar link

The first one, the mono-polar link, has a single conductor of negative polarity and the return path is provided through the ground. Whereas, the bipolar link has one positive conductor and another negative conductor as the return path. The terminal converters are of equal voltage ratings and are connected in series. However, the homopolar link has minimum two conductors with the same polarity; usually a negative, and the return

path is provided through the ground as in the case of the mono-polar link [9]. In this study, an HVDC link with two ac/dc converters connected by a single dc line is considered for the stability impact on the high penetration of a DFIG-based wind farm. Fig. 3.2 represents a simplified diagram of the HVDC link in which a converter connected to bus-*k* is a rectifier and the converter connected to bus-*m* is an inverter.

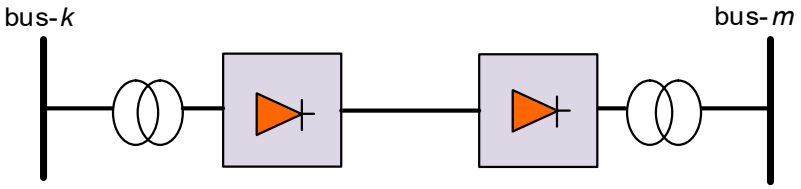

Figure 3.2 HVDC link

However, the converters function is reversed with the change in the direction of current flow. The firing angle α and extinction angle γ are controlled by the proportional integral regulators as shown in HVDC current control circuits in Fig. 3.3. Where I_{R0} and I_{I0} are reference currents of the rectifier and inverter respectively, K_P is proportional gain and K_I is integral gain.

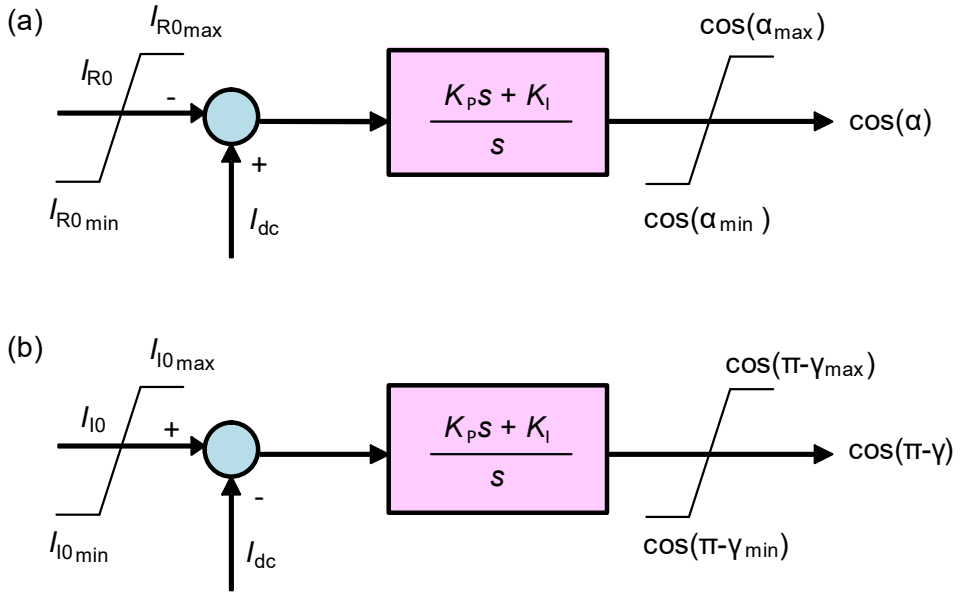

Figure 3.3 Current control circuits for (a) rectifier (b) inverter of HVDC link

The model of HVDC can be described by the following equations [151]

$$I_{\mathrm{dc}} = (V_{R_{\mathrm{dc}}} - V_{I_{\mathrm{dc}}} - R_{\mathrm{dc}} I_{\mathrm{dc}})/L_{\mathrm{dc}} \tag{3.16}$$

where I_{dc} is dc current flowing from rectifier to inverter; $V_{R_{\mathrm{dc}}}$ and $V_{I_{\mathrm{dc}}}$ are dc voltages at the rectifier and inverter terminals respectively, and R_{dc} and L_{dc} respectively are the resistance and inductance of the dc line.

The active and reactive powers of the rectifier at bus-*k* are:

$$P_{km} = \frac{V_{\mathrm{n_{dc}}} I_{\mathrm{n_{dc}}}}{S_{\mathrm{n}}} V_{\mathrm{R_{dc}}} I_{\mathrm{dc}} \tag{3.17a}$$

$$Q_{km} = \sqrt{S_{\mathrm{R}}^2 - \left(\frac{V_{\mathrm{n_{dc}}} I_{\mathrm{n_{dc}}}}{S_{\mathrm{n}}} V_{\mathrm{R_{dc}}} I_{\mathrm{dc}}\right)^2} \tag{3.17b}$$

$$V_{\mathrm{R_{dc}}} = \frac{3\sqrt{2}}{\pi} V_k cos\alpha - \frac{3}{\pi} X_{\mathrm{tR}} I_{\mathrm{dc}}$$

$$S_{\mathrm{R}} = \frac{3\sqrt{2} v_{\mathrm{n_{dc}}} I_{\mathrm{n_{dc}}}}{S_{\mathrm{n}}} V_k I_{\mathrm{dc}}$$

where S_{n}, $V_{\mathrm{n_{dc}}}$, $I_{\mathrm{n_{dc}}}$ V_k and X_{tR} are the rated apparent power at the ac side, voltage and current ratings at the dc side, voltage at bus-*k* and rectifier side transformer reactance respectively. The active and reactive powers of the inverter at bus-*k* are given as

$$P_{mk} = \frac{V_{\mathrm{n_{dc}}} I_{\mathrm{n_{dc}}}}{S_{\mathrm{n}}} V_{\mathrm{I_{dc}}} I_{\mathrm{dc}} \tag{3.18a}$$

$$Q_{mk} = \sqrt{S_{\mathrm{I}}^2 - \left(\frac{V_{\mathrm{n_{dc}}} I_{\mathrm{n_{dc}}}}{S_{\mathrm{n}}} V_{I_{\mathrm{dc}}} I_{\mathrm{dc}}\right)^2} \tag{3.18b}$$

$$V_{\mathrm{I_{dc}}} = \frac{3\sqrt{2}}{\pi} V_m cos(\pi - \gamma) - \frac{3}{\pi} X_{\mathrm{tI}} I_{\mathrm{dc}}$$

$$S_{\mathrm{I}} = \frac{3\sqrt{2} V_{\mathrm{n_{dc}}} I_{\mathrm{n_{dc}}}}{S_{\mathrm{n}}} V_m I_{\mathrm{dc}}$$

where V_m refers to the voltage at bus-*m* and X_{tI} denotes the inverter side transformer reactance.

3.3 FACTS devices

A detail mathematical model of the series and shunt FACTS devices are developed and presented in this section. The devices that are used for the study are SSSC and SVC, and are explained below.

3.3.1 Static synchronous series compensator

As the power transmission through a transmission line is limited by the series reactive impedance of the line, a series compensation can cancel a portion of the reactive impedance, thus, increasing the power transmission capability. A series FACTS device, with its variable series compensation capability, controls power flow in the line improving the stability. An SSSC is a voltage source inverter connected in series with the line and injects a sinusoidal voltage in quadrature with the line current. An SSSC compensated line is shown in Fig. 3.4. The injected quadrature voltage behaves as an inductive or a capacitive reactance in series with the line it is installed at [157].

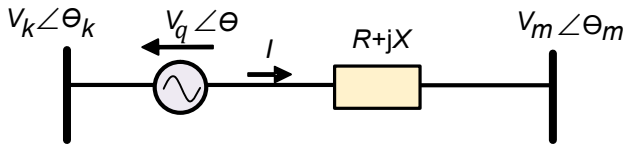

Figure 3.4 SSSC compensated line

where V_q is the magnitude of the injected voltage ($0 \leq V_q \leq V_q^{max}$) in the line, with bus-$k$ and bus-m voltage angles are respectively denoted by Θ_k and Θ_m. The ^{max} indicates maximum value of the injected voltage. The SSSC has a capability of inserting capacitive or inductive compensating voltage irrespective of the changing line current I up to its specified current rating [158].

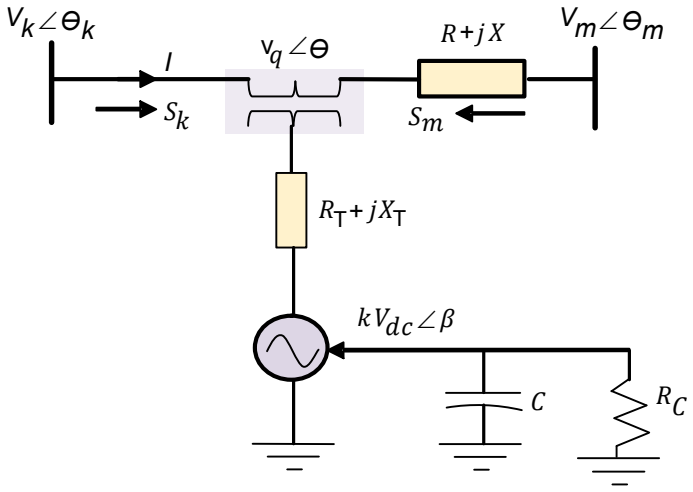

Figure 3.5 SSSC circuit

A simplified SSSC circuit is shown in Fig. 3.5. The equations to represent SSSC can be written as [151]

$$V_q = V_{\mathrm{I}} - (R_{\mathrm{T}} + \mathrm{j}X_{\mathrm{T}})I \tag{3.19}$$

$$V_k = V_q + V_m + (R + \mathrm{j}X)I \tag{3.20}$$

where $V_{\mathrm{I}} = kV_{\mathrm{dc}}e^{\mathrm{j}\beta}$, S_k and S_m respectively represent apparent power injection at bus-k and bus-m, V_{dc} denotes DC voltage, C and R_{C} respectively refers to the capacitance and resistance of the DC circuit, whereas, R_{T} and X_{T} express the resistance and reactance of the AC circuit.

From (3.19),

$$I = \frac{V_k - V_m - V_{\mathrm{I}}}{(R_{\mathrm{T}} + R) + \mathrm{j}(X_{\mathrm{T}} + X)} \tag{3.21a}$$

$$V_{\mathrm{q}} = \frac{R + \mathrm{j}X}{(R_{\mathrm{T}} + R) + \mathrm{j}(X_{\mathrm{T}} + X)}(V_k - V_m) + \frac{R_{\mathrm{T}} + \mathrm{j}X_{\mathrm{T}}}{(R_{\mathrm{T}} + R) + \mathrm{j}(X_{\mathrm{T}} + X)}V_{\mathrm{I}} \tag{3.21b}$$

The power injection at the SSSC bus-k and bus-m are

$$S_k = V_k . I^* \tag{3.22a}$$

$$S_m = -V_m . I^* \tag{3.22b}$$

where I^* denotes the conjugate of current I.

3.3.2 Static voltage compensator

An SVC is composed of thyristor-switched capacitors and reactors, the output of which is varied to produce and consume reactive power so as to control a specific parameter of the power system [158], typically the SVC bus voltage. The SVC increases system loadability [159] and provides dynamic voltage control to enhance power oscillation damping in addition to the improvement in the power system stability. As the power oscillation is a continuous phenomenon, the shunt compensation hence the voltage is necessary to be varied continuously to counteract the accelerating and decelerating swings of the disturbed machines [158]. Additionally, a supplementary controller with a suitable stabilizing signal can be designed to provide additional damping of low frequency power system oscillations [160]. A typical block diagram of the SVC control is shown in the Fig. 3.6.

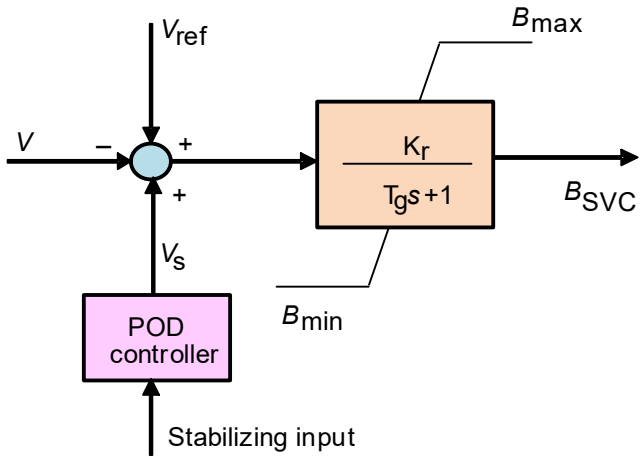

Figure 3.6 SVC block with supplementary control

The following differential equation can express susceptance B_{SVC} of the SVC model as

$$\dot{B_{\mathrm{svc}}} = (\mathrm{K_r}(V_{\mathrm{ref}} + V_{\mathrm{s}} - V) - B_{\mathrm{SVC}})/T_{\mathrm{r}} \quad (3.23a)$$

$$Q_{\mathrm{SVC}} = -B_{\mathrm{SVC}}V^2 \quad (3.23b)$$

in which V_{ref}, V_{s} and V are reference voltage, stabilizing input voltage, and bus voltage; whereas, $\mathrm{K_r}$, and T_g denote regulator gain and time constant respectively.

3.3.2.1 Location of SVC

For voltage stability enhancement study, the identification of the weakest bus is an essential decision to power engineers. Power flow sensitivity analysis can be used to perform the static voltage stability analysis in order to identify the weak buses or regions in a power network. In which, the modes of voltage instability are calculated using eigenvalues of the sensitivity matrix. The modes with the smallest magnitude is considered to be the weakest mode to the voltage stability. Then, the participation factor analysis can be performed to calculate the percentage participation of the buses to the mode of interest. The bus which exhibits the highest participation to the weakest mode gives the most appropriate location for the shunt reactive device from the voltage stability enhancement perspective [98].

The participation factor equation below gives the relationship of a bus-*k* to eigenmode *l* as:

$$\mathbf{PF}_{kl} = \boldsymbol{\Phi}_{kl}.\boldsymbol{\Psi}_{lk} \quad (3.24)$$

where $\boldsymbol{\Phi}_{kl}$ is the k^{th} entry of right eigenvector $\boldsymbol{\Phi}_l$, and $\boldsymbol{\Psi}_{lk}$ is the k^{th} entry of left eigenvector $\boldsymbol{\Psi}_l$.

3.3.2.2 Supplementary controller design

A supplementary stabilizing signal can modulate SVC control for enhancing the damping of low frequency system oscillations. The effectiveness of the oscillation damping performance of SVC depends on its location, input signal and controller design [9]. The mode of oscillation to be damped should be responsive to the supplementary input signal. The input signal for this study is chosen using different stability indicators such as residue analysis method, Hankel singular value method, right hand plane zeros. A wide range of local and global signals such as active powers, reactive powers and line currents are examined to select the best signal which can be utilized to achieve the highest damping performance of the controller designed.

In residue analysis method, $\mathbf{G}(s)$ is considered as an open loop transfer function between input variable u and output variable y. The residue matrix of the model can be obtained as [101]

$$\mathbf{G}(s) = \frac{\Delta y(s)}{\Delta u(s)} = \mathbf{C}(s\mathbf{I} - \mathbf{A})^{-1}\mathbf{B} = \sum_{i=1}^{n} \frac{\mathrm{R}_j}{(s - \lambda_j)} \tag{3.25a}$$

in which **A**, **B,** and **C** are matrices of state space model of the system; **I** refers to identify matrix. Residue R_j at eigenvalue λ_j, associated with mode j, can be expressed as

$$\mathrm{R}_j = \mathbf{C}\boldsymbol{\phi}_j\boldsymbol{\psi}_j \tag{3.25b}$$

The signal having the highest residue magnitude is selected as the feedback signal for the supplementary controller. In case of Hankel singular value method, joint observability and controllability indices of the power system are evaluated. The input and output signals showing more information on the system internal states are selected as the candidates for feedback control signal.

For a state space model with matrices **A**, **B**, **C** and **D**, Hankel singular values are given by [161]

$$\sigma_n = \sqrt{\lambda_j(\mathbf{EF})} \tag{3.26}$$

where **E** and **F** are controllability and observability grammians and are the solution of

$$\mathbf{AE} + \mathbf{EA}^T = -\mathbf{BB}^T \quad (3.27a)$$

$$\mathbf{A}^T\mathbf{F} + \mathbf{FA} = -\mathbf{C}^T\mathbf{C} \quad (3.27b)$$

The candidate input signal with the highest Hankel singular value represents better controllability and observability properties and can give more information about the internal stages of the power system [162].

In right hand plane zeros method, feedback of a controller changes pole locations with a change in gain whereas zeros remain unaffected. As we increase the feedback gain, the closed loop poles move from open loop pole positions to open loop zeros. This characteristic makes instability condition for a system with zeros in the right hand plane. Thereby, the input signal selected should have a minimum number of right hand plane zeros and should not lie outside the closed-loop bandwidth [162].

With the appropriate input signal selection, the next step is to determine the parameters of the controller. A typical block diagram of a power oscillation damping controller is shown in Fig. 3.7. It consists of a stabilizer gain, a washout filter block, and lead-lag block. The gain determines the damping provided by the controller, washout is to eliminate the dc component of the signal, and the phase compensators give phase lead-lag compensation [163].

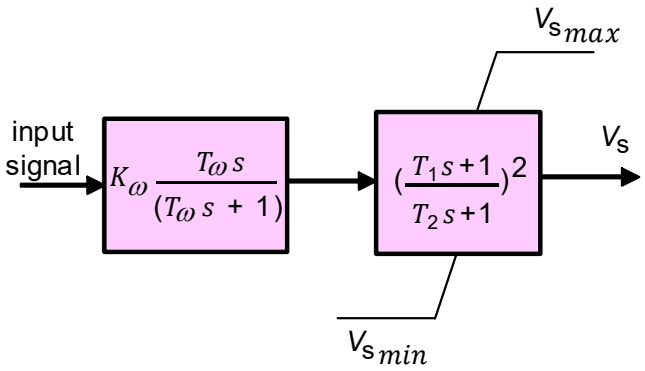

Figure 3.7 Typical block diagram of a supplementary controller

A compensator can be designed as [163]

$$POD(s) = K_\omega \left(\frac{T_\omega s}{T_\omega s+1}\right)\left(\frac{T_1 s+1}{T_2 s+1}\right)^2 \quad (3.28a)$$

$$T_2 = \frac{1}{\left(\omega_n \sqrt{(1-sin\frac{\emptyset}{k})/(1+sin\frac{\emptyset}{k})}\right)} \quad (3.28b)$$

$$T_1 = \frac{\left(1 - sin\frac{ø}{k}\right)}{\left(1 + sin\frac{ø}{k}\right)} T_2 \tag{3.28c}$$

where ø is phase compensation; ω_n is the oscillatory frequency of the critical mode; k is the number of lead-lag blocks, and T_1 and T_2 are time constants.

Controller gain (K_ω) can be determined by using root locus technique, and washout time constant T_ω is usually taken as 5-10 s [99].

3.4 Analysis of small signal stability

Small signal stability analysis provides information about the inherent dynamic characteristics of the power system. For the small signal stability analysis, the power system may be modelled by using a set of n first order nonlinear differential equations as [9]

$$\dot{x_i} = f_i(x_1, x_2, \dots, x_h; u_1, u_2, \dots, u_g; t) \tag{3.29}$$

where $i = 1, 2, \dots h$, in which h is the order of the power system, g is the number of inputs and t is time.

In vector-matrix notation

$$\dot{\mathbf{x}} = \mathbf{f}(\mathbf{x}, \mathbf{u}, t) \tag{3.30}$$

where

$$\mathbf{x} = \begin{bmatrix} x_1 \\ x_2 \\ \vdots \\ x_h \end{bmatrix}, \mathbf{u} = \begin{bmatrix} u_1 \\ u_2 \\ \vdots \\ u_g \end{bmatrix} \text{ and } \boldsymbol{f} = \begin{bmatrix} f_1 \\ f_2 \\ \vdots \\ f_h \end{bmatrix}$$

Vector **x** is the state vector, and x_i is the state variable. Vector **u** is the vector of inputs to the system.

In an autonomous system, (3.30) further simplifies to

$$\dot{\mathbf{x}} = \mathbf{f}(\mathbf{x}, \mathbf{u}) \tag{3.31a}$$

$$\mathbf{y} = \mathbf{g}(\mathbf{x}, \mathbf{u}) \tag{3.31b}$$

where

$$\mathbf{y} = \begin{bmatrix} y_1 \\ y_2 \\ \vdots \\ y_n \end{bmatrix} \text{ and } \mathbf{g} = \begin{bmatrix} g_1 \\ g_2 \\ \vdots \\ g_n \end{bmatrix}$$

y is output vector, and **g** is the vector of nonlinear functions linking state and input variables to output variables.

Linearization of (3.31a) and (3.31b) gives

$$\Delta\dot{\mathbf{x}} = \mathbf{A}\,\Delta\mathbf{x} + \mathbf{B}\Delta\mathbf{u} \tag{3.32}$$

$$\Delta\mathbf{y} = \mathbf{C}\,\Delta\mathbf{x} + \mathbf{D}\Delta\mathbf{u} \tag{3.33}$$

The small signal stability analysis is carried out using a linearized model. The eigenvalue of the state matrix **A** gives small signal stability of the power system.

- A real eigenvalue represents a non-oscillatory mode. A negative real eigenvalue refers to a decaying mode whereas a positive real eigenvalue corresponds to the aperiodic instability.
- Complex eigenvalues refer to an oscillatory mode of which real component gives the damping, and the imaginary component gives the frequency of oscillation. A negative real part refers to a damped oscillation, and a positive real part refers to an oscillation of increasing amplitude.

A complex eigenvalues pair is written as

$$\lambda = \alpha \pm j\omega_{\mathrm{n}} \tag{3.34}$$

of which, the oscillatory frequency can be expressed as

$$f = \omega_{\mathrm{n}}/2\pi \tag{3.35}$$

Whereas, the damping ratio ζ defines the decline of the oscillatory amplitude, and is expressed as

$$\zeta = -\alpha/\sqrt{(\alpha^2+\omega_{\mathrm{n}}{}^2)} \tag{3.36}$$

The contribution of the state variables on the oscillatory modes can be evaluated by using participation factor analysis. In a dynamic system, the participation factor gives the relationship among the state variables and eigenmode [164]. The participation of k^{th} state in the l^{th} eigenmode can be expressed as given by the section 3.24, in which k is the state variable.

The sensitivity of an eigenvalue λ_j to a system parameter K_l can be defined and presented as

$$\frac{\partial\lambda_j}{\partial K_{\mathrm{l}}} = \frac{\boldsymbol{\Psi}_j^T\left(\frac{\partial\mathbf{A}}{\partial K_l}\right)\boldsymbol{\Phi}_j}{\boldsymbol{\Psi}_j^T\boldsymbol{\Phi}_j} \tag{3.37}$$

With the eigenvalue sensitivity, the most sensitive eigenvalue to a change in system parameter can be identified. This study is vital for the stability analysis following the change in the system parameter.

3.5 Transient stability

Transient stability represents the capacity of a power system to remain in synchronism following severe transient disturbances. Such severe transient conditions may be the fault in lines, loss of generation or sudden loss of large loads [9]. In a power system with DFIG-based generators, disturbances in generator's load give rise to a speed variation and rotor position variation. However, being an asynchronous machine, the position of rotor flux vector is independent of the physical position of the rotor, and the synchronizing torque angle characteristics does not exist [165]. However, the machine rotor angle with respect to the synchronously rotating reference gives a means for a test of power system stability. Transient stability index (TSI) gives the severity of a contingency and the trajectory of a power system following a disturbance [29].

$$\mathrm{TSI} = \frac{360 - \delta^{\max}}{360 + \delta^{\max}} \times 100 \tag{3.38}$$

where $-100 < \mathrm{TSI} < 100$, $\mathrm{TSI} > 0$ and $\mathrm{TSI} \leq 0$ correspond to the stable and unstable conditions respectively.

3.6 Construction and operation of a microgrid components

The electric power system has the same basic characteristics even though they vary in size and structural components [9]. Detail description of construction and operation of building components of a microgrid, considered in this research, and is presented in this section. The microgrid consists of conventional synchronous generators (SGs), converter-based sources (DGs), and battery energy storages (BESs), lines and loads. The *P-f* droop control method is considered as the controller of the generators in remote areas microgrids. This droop control is a simple and does not need any communication between the generators. The generator equations are considered in more generic forms using voltage and droop equations.

3.6.1 Synchronous generators

The synchronous generator is equipped with excitation and governor control systems and is directly connected to the microgrid network. In the excitation control system, the synchronous generator's terminal voltage magnitude v_m is continuously compared

against v_{ref} and their difference is applied to the exciter to yield a suitable v_{fd} as shown in Fig. 3.8.

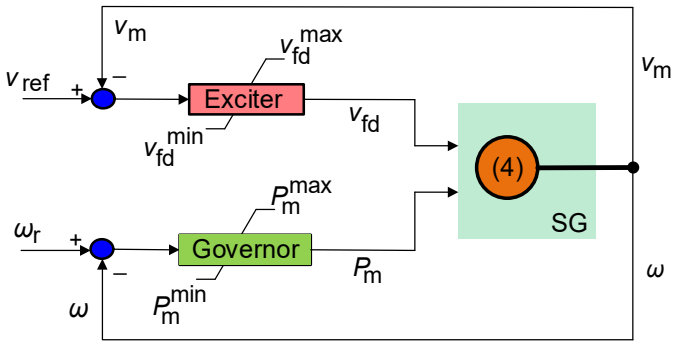

Figure 3.8 Block diagram of a synchronous generator

The angular frequency $\omega = 2\pi f_{SG}$ is acquired from the synchronous generator's droop equation of

$$f_{SG\text{-}i} = f^{max} - m_{SG\text{-}i} P_{SG\text{-}i} \tag{3.39}$$

while the difference between ω with that of rotor (ω_r) is applied to the governor to yield a suitable mechanical input power to the synchronous generator as shown in Fig. 3.8. The rotor motion is presented by the swing equation as

$$\frac{d\omega_r}{dt} = \frac{T_m - T_e}{J_r} \tag{3.40}$$

In (3.39), m_{SG} represents the synchronous generator's P-f droop coefficient. On the other hand, in (3.40), J_r expresses the rotor mass inertia; T_m represents the mechanical input torque to the shaft of the rotor; T_e shows the output electrical torque, given by [166]

$$T_e = \frac{1.5N_p}{2\omega_b}\left[X_{md} i^q \left(-i^d + i^{fd} + i^{kd}\right) - X_{mq} i^d \left(-i^q + i^{k1q} + i^{k2q}\right)\right] \tag{3.41}$$

in which X_{md} and X_{mq} are magnetizing reactance, and N_p represents the synchronous generator's number of poles. In (3.41), the current i flowing through the stator (noted by d and q), damper (depicted by ^{kd}, ^{k1q} and ^{k2q}) and field windings (shown by ^{fd}), based on which the synchronous generator's state variable of $\mathbf{x}_{SG} = [i^q \;\; i^d \;\; i^{k1q} \;\; i^{k2q} \;\; i^{fd} \;\; i^{kd}]^T$ can be formed while ^{T} is the transpose operator. The voltages appearing across the above windings (given by $\mathbf{v}_{SG} = [v^q \;\; v^d \;\; v^{k1q} \;\; v^{k2q} \;\; v^{fd} \;\; v^{kd}]^T$) can be expressed as [166]

$$\mathbf{v}_{SG} = \mathbf{L}_{SG}\mathbf{x}_{SG} + \mathbf{K}_{SG}\dot{\mathbf{x}}_{SG} \tag{3.42a}$$

as expanded in

$$\begin{bmatrix} v^{q} \\ v^{d} \\ v^{k1q} \\ v^{k2q} \\ v^{fd} \\ v^{kd} \end{bmatrix} = \begin{bmatrix} -r_s & \frac{-\omega X_d}{\omega_b} & 0 & 0 & \frac{-\omega X_{md}}{\omega_b} & \frac{-\omega X_{md}}{\omega_b} \\ \frac{\omega X_q}{\omega_b} & -r_s & \frac{-\omega X_{mq}}{\omega_b} & \frac{-\omega X_{mq}}{\omega_b} & 0 & 0 \\ 0 & 0 & r_{k1q} & 0 & 0 & 0 \\ 0 & 0 & 0 & r_{k2q} & 0 & 0 \\ 0 & 0 & 0 & 0 & X_{md} & 0 \\ 0 & 0 & 0 & 0 & 0 & r_{kd} \end{bmatrix} \begin{bmatrix} i^{q} \\ i^{d} \\ i^{k1q} \\ i^{k2q} \\ i^{fd} \\ i^{kd} \end{bmatrix} + \begin{bmatrix} \frac{-X_q}{\omega_b} & 0 & \frac{X_{mq}}{\omega_b} & \frac{X_{mq}}{\omega_b} & 0 & 0 \\ 0 & \frac{-X_d}{\omega_b} & 0 & 0 & \frac{X_{md}}{\omega_b} & \frac{X_{md}}{\omega_b} \\ \frac{-X_{mq}}{\omega_b} & 0 & \frac{X_{k1q}}{\omega_b} & \frac{X_{mq}}{\omega_b} & 0 & 0 \\ \frac{-X_{mq}}{\omega_b} & 0 & \frac{X_{mq}}{\omega_b} & \frac{X_{k2q}}{\omega_b} & 0 & 0 \\ 0 & \frac{-X_{md}^2}{r_{fd}\omega_b} & 0 & 0 & \frac{X_{md}X_{fd}}{r_{fd}\omega_b} & \frac{X_{mq}^2}{r_{fd}\omega_b} \\ 0 & \frac{X_{md}}{\omega_b} & 0 & 0 & \frac{X_{md}}{\omega_b} & \frac{X_{kd}}{\omega_b} \end{bmatrix} \begin{bmatrix} i^{q} \\ i^{d} \\ i^{k1q} \\ i^{k2q} \\ i^{fd} \\ i^{kd} \end{bmatrix}^{\bullet} \tag{3.42b}$$

where • is the differential operator.

To develop a global reference frame when multiple synchronous generators exist, one of the buses of the microgrid (e.g., the bus to which the first synchronous generator is connected) is thought to have a voltage angle of zero; hence, other angles within the microgrid will be expressed versus that.

3.6.2 Converter based sources

The non-inertial DGs and BESs are assumed to be linked to the microgrid through a centre-tapped, three-legged voltage source converter, in which each leg is comprised of two insulated gate bipolar transistors and anti-parallel diodes as shown in Fig. 3.10. During unbalanced loading, this configuration creates a path for the current's zero sequence component to flow through. At the output of voltage source converter, a three-phase star-connected transformer (with a turns ratio of 1: *a*) provides voltage

boosting and galvanic isolation. An L_f - C_f - L_T filter at the output of the transformer suppresses the current and voltage harmonics and regulates the output power while resistance R_f denotes the total losses of transformer and voltage source converter. Each leg of the voltage source converter produces an output voltage with a square wave and a peak of uaV_{dc}, in which u represents the switching function (i.e., $u = +1$ when switch S_1 is closed and $u = -1$ when switch S_1' is closed for phase-a under a bipolar switching [167]).

The intended voltage magnitude across capacitors C_f is tracked using a voltage control technique in abc frame. Assuming a state vector of $\mathbf{z}(t) = [i_2(t) \;\; i_c(t) \;\; v_c(t)]^T$ for each phase, in which i_2 represents the current through L_T while v_c and i_c show the voltage across and current through C_f. Then, each leg of the voltage source converter and filter as shown in Fig. 3.9 can be expressed by the state-space explanation of [135]

$$\mathbf{z}^{\bullet}(t) = \mathbf{A}_z\,\mathbf{z}(t) + \mathbf{B}_z\,u_c(t) + \mathbf{C}_z v_t(t) \tag{3.43}$$

in which v_t refers to the terminal voltage and is a disturbance for the above system. Implementing a state feedback control, u_c can be expressed as

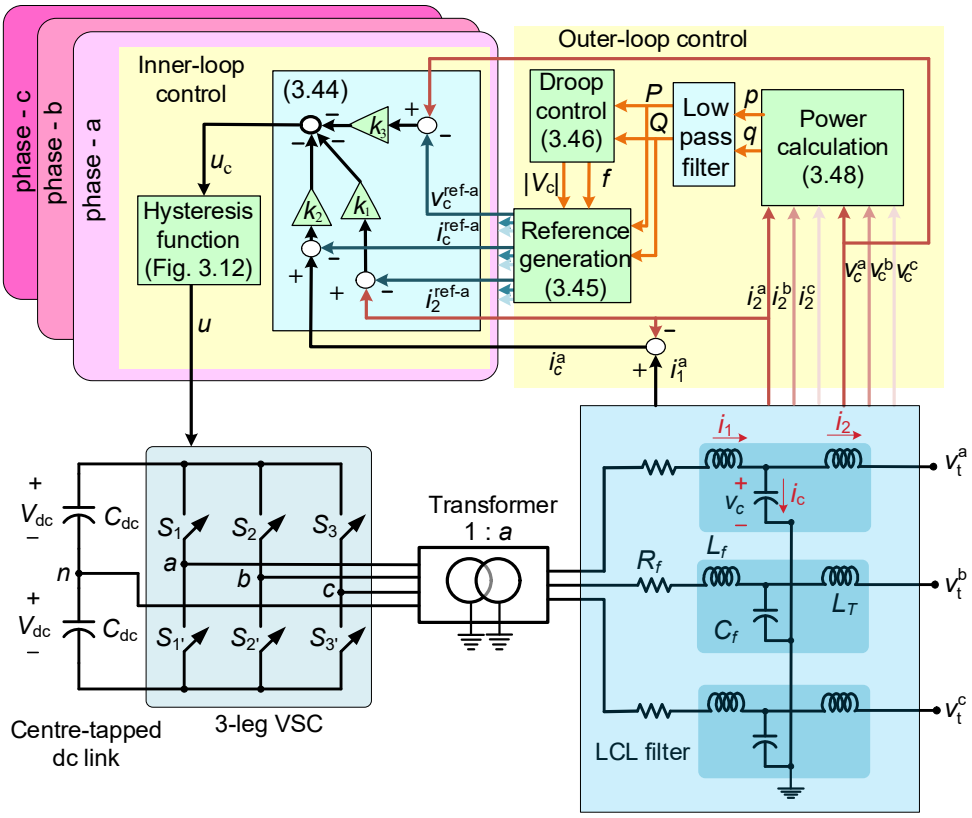

Figure 3.9 Voltage source converter and filter structure with the considered closed loop control for each non-inertial distributed generator

$$u_{\mathrm{c}}(t) = -\mathbf{k}\left[\mathbf{z}(t) - \mathbf{z}^{\mathrm{ref}}(t)\right]^{T} \tag{3.44}$$

where $\mathbf{z}_{\mathrm{ref}}$ is the reference of $\mathbf{z}$ and is given by [135]

$$v_{\mathrm{c}}(t)^{\text{ref-a}}_{\text{DG-}i} = \sqrt{2}\left|V_{\mathrm{c}}\right|_{\text{DG-}i}\cos\left(2\pi f_{\text{DG-}i}t\right) \tag{3.45a}$$

$$i_{\mathrm{c}}(t)^{\text{ref-a}}_{\text{DG-}i} = 2\sqrt{2}\pi f_{\text{DG-}i}C_{\mathrm{f}}\left|V_{\mathrm{c}}\right|_{\text{DG-}i}\cos\left(2\pi f_{\text{DG-}i}t + 90°\right) \tag{3.45b}$$

$$i_{2}(t)^{\text{ref-a}}_{\text{DG-}i} = \frac{\sqrt{2}}{3}\frac{\sqrt{P^{2}_{\text{DG-}i} + Q^{2}_{\text{DG-}i}}}{\left|V_{\mathrm{c}}\right|_{\text{DG-}i}}\cos\left(2\pi f_{\text{DG-}i}t - \gamma\right) \tag{3.45c}$$

for DG-i in which $\gamma = \tan^{-1}(Q_{\text{DG-i}}/P_{\text{DG-i}})$ while $\mathbf{k} = [k_1 \;\; k_2 \;\; k_3]$ represents the control variables vector determined by a linear quadratic regulator [135]. In (3.45a-c), f_{DG} and $|V_{\mathrm{c}}|_{\mathrm{DG}}$ respectively refer to frequency and magnitude of the voltage source converter's output voltage, determined from the droop equations of

$$f_{\text{DG-}i} = f^{\max} - m_{\text{DG-}i}P_{\text{DG-}i} \tag{3.46a}$$

$$\left|V_{\mathrm{c}}\right|_{\text{DG-}i} = V^{\max} - n_{\text{DG-}i}Q_{\text{DG-}i} \tag{3.46b}$$

in which $V^{\max}$ is the maximum permitted voltage magnitude in the microgrid, and n_{DG} represents the Q-V droop coefficient. When active and reactive powers of a DG decrease from the maximum values to zero, the frequency and voltage magnitude at its output increase from $f^{\min}$ to $f^{\max}$ and $V^{\min}$ to $V^{\max}$ around the base (nominal) frequency and voltage magnitudes of f^{b} and V^{b} as seen from Fig. 3.10 while $^{\min}$ denotes the least allowed limit. From (3.46a) and (3.46b), m_{DG} and n_{DG} can be expressed for a DG as

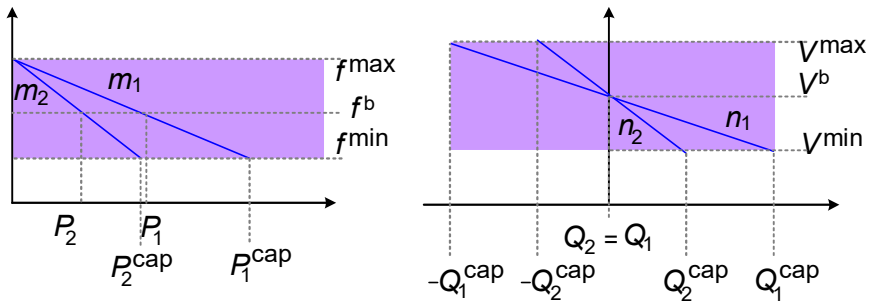

Figure 3.10 Considered droop characteristic

$$m_{\text{DG-}i} = \frac{f^{\max} - f^{\min}}{P^{\mathrm{cap}}_{\text{DG-}i}} \tag{3.47a}$$

$$n_{\text{DG-}i} = \frac{V^{\max} - V^{\min}}{2Q^{\text{cap}}_{\text{DG-}i}} \tag{3.47b}$$

in which cap represents the DGs' capacity. Thus, all DGs possess identical $\Delta f = f^{\max} - f^{\min}$ and $\Delta V = V^{\max} - V^{\min}$, albeit their capacities. The power generation ratios (both active and reactive) of two sources (e.g., DG-*i* and DG-*j*) are assumed equivalent to their power capacity ratios and are reciprocal to the ratio of their droop coefficients [168].

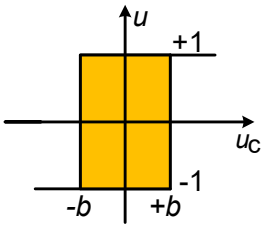

Figure 3.11 Assumed hysteresis function

Eq. (3.44) presents the input value to the voltage source converter's control system, which is the weighted sum of the tracking errors for **z**(t). A reduction in tracking error can be achieved if it is limited inside a tiny bandwidth of $b > 0$. From (3.44) and using a hysteresis function in the form of Fig. 3.11, switching function u can be generated for each leg of the voltage source converter. The same closed-loop control mechanism is applied to the remaining phases, considering ±120° phase shifts in the references of (3.45). The block diagram of the assumed closed-loop control of the voltage source converter is also presented in Fig. 3.10, which shows the switching as well as the droop control of the DG. The instantaneous values of active and reactive power generation (denoted by *p* and *q*) can be computed as [167]

$$p(t) = i_2^{\text{a}}(t)v_{\text{c}}^{\text{a}}(t) + i_2^{\text{b}}(t)v_{\text{c}}^{\text{b}}(t) + i_2^{\text{c}}(t)v_{\text{c}}^{\text{c}}(t) \tag{3.48a}$$

$$q(t) = \frac{1}{\sqrt{3}}\left[i_2^{\text{a}}(t)\left(v_{\text{c}}^{\text{b}}(t) - v_{\text{c}}^{\text{c}}(t)\right) + i_2^{\text{b}}(t)\left(v_{\text{c}}^{\text{c}}(t) - v_{\text{c}}^{\text{a}}(t)\right) + i_2^{\text{c}}(t)\left(v_{\text{c}}^{\text{a}}(t) - v_{\text{c}}^{\text{b}}(t)\right)\right] \tag{3.48b}$$

where phases a, b, and c are denoted by a, b and c respectively. A first-order low pass filter with a cut-off frequency of ω_{c} can then yield the average active and reactive powers.

It is to be noted that one may use the generalized droop control method or a cost-prioritized droop technique of [169-170] instead of (3.46). Also, DGs are assumed

dispatchable by being combined to suitably-sized local energy storage that acts as a power smoother; thereby, they are supposed to be having the capacity of injecting the powers as defined by their droop coefficient. When, because of the environmental reasons, the output power of a DG is saturated before reaching the desired value, the remaining DGs in the microgrid will contribute to share the load as defined by the ratio of their capacities.

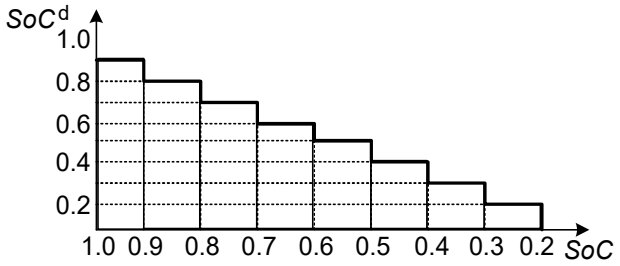

Figure 3.12 Discretised SoC for BESs

In this research, BESs are also converter-interfaced, and the above-mentioned voltage source converter and filter structure and control is also employed for them. The only dissimilarity is that a different droop coefficient is used in the form of

$$m_{\text{BES-}i} = \frac{f^{\max} - f^{\min}}{SoC^{\text{d}}_{\text{BES-}i}\, P^{\text{cap}}_{\text{BES-}i}} \tag{3.49}$$

in which $SoC^{\text{d}}_{\text{BES}}$ is a discrete number between 0.2 and 1 in steps of 0.1 as seen in Fig. 3.12 and is calculated from the BES's state of charge (SoC) [171] while $P^{\text{cap}}_{\text{BES}}$ denotes the BES's power charging and discharging capacity. Using (3.49), the share of power supplied by a BES is correlated with its SoC and when multiple BESs exist within the microgrid, their SoCs decline to the minimum acceptable SoC of $\text{SoC}^{\min}$ simultaneously. It is seen from 3.49 that as $SoC^{\text{d}}_{\text{BES}}$ becomes smaller, the injected active power by the BES also decreases. Hence, active power occupies a smaller share of the BES's converter capacity ($S^{\text{cap}}_{\text{BES}}$), and thereby, the remaining capacity is available for exchanging reactive power, based on which the BES-*i*'s *Q*-*V* droop coefficient (n_{BES}) can be updated as

$$n_{\text{BES-}i} = \frac{\Delta V}{2\sqrt{\left(S^{\text{cap}}_{\text{BES-}i}\right)^2 - \left(SoC^{\text{d}}_{\text{BES-}i} P^{\text{cap}}_{\text{BES-}i}\right)^2}} \tag{3.50}$$

It is noted that the exchange of reactive power between the microgrid and the BES's voltage source converter will not affect its SoC.

3.7 Holistic small-signal model a microgrid

A holistic small signal modelling of a microgrid is presented in this section which establishes a set of detailed system equations as a platform to accurately assess a microgrid's small signal stability, and to analyse sensitivity of the variations in its internal parameters.

Let SG-*i*'s state-space explanation in global dq setting be given as

$$\Delta \mathbf{x}_{\mathrm{SG}}^{\bullet i} = \mathbf{A}_{\mathrm{SG}}^{i} \Delta \mathbf{x}_{\mathrm{SG}}^{i} + \mathbf{B}_{\mathrm{SG}}^{i} \Delta \mathbf{u}_{\mathrm{SG}}^{i} + \mathbf{C}_{\mathrm{SG}}^{i} \Delta \mathbf{v}_{\mathrm{SG}}^{i} \tag{3.51a}$$

in which $\Delta \mathbf{u}_{\mathrm{SG}}^{i} = X_{\mathrm{md}}^{i}[\, i^{\mathrm{fd}} \;\; \mathbf{O}_{1\times 5}]^{T}$ designates the input control vector. The synchronous generator's matrices expressed in (3.51a) can be calculated and represented as [166]

$$\begin{aligned} \mathbf{A}_{\mathrm{SG}} &= \mathbf{T}^{-1}\, \mathbf{A}_{\mathrm{SG}}^{\mathrm{R}}\, \mathbf{T} - \mathbf{T}^{-1}\mathbf{T}^{\bullet} \\ \mathbf{B}_{\mathrm{SG}} &= \mathbf{T}^{-1}\, \mathbf{B}_{\mathrm{SG}}^{\mathrm{R}} \cos\delta \\ \mathbf{C}_{\mathrm{SG}} &= \mathbf{T}^{-1}\, \mathbf{C}_{\mathrm{SG}}^{\mathrm{R}}\, \mathbf{T} \end{aligned} \tag{3.51b}$$

where $\mathbf{A}_{\mathrm{SG}}^{\mathrm{R}} = -\mathbf{K}_{\mathrm{SG}}^{-1}\mathbf{L}_{\mathrm{SG}}$, $\mathbf{C}_{\mathrm{SG}}^{\mathrm{R}} = -\mathbf{K}_{\mathrm{SG}}^{-1}$, and $\mathbf{B}_{\mathrm{SG}}^{\mathrm{R}}$ which is equal to the 5th column of $\mathbf{C}_{\mathrm{SG}}^{\mathrm{R}}$ are the matrices in the synchronous generator's local reference frame, and δ is the angle between the global and the local reference frame. In (3.51b), $^{-1}$ denotes the matrix inverse operator while

$$\mathbf{T} = \begin{bmatrix} \cos\delta & -\sin\delta & 0 & 0 & 0 & 0 \\ \sin\delta & \cos\delta & 0 & 0 & 0 & 0 \\ 0 & 0 & \cos\delta & 0 & 0 & 0 \\ 0 & 0 & 0 & \cos\delta & 0 & 0 \\ 0 & 0 & 0 & 0 & \cos\delta & 0 \\ 0 & 0 & 0 & 0 & 0 & \cos\delta \end{bmatrix}$$

is the transformation matrix from the local frame of a synchronous generator to the global reference frame of the microgrid.

Similarly, let the state-space explanation of the converter based source, DG-*i* be given as

$$\Delta \mathbf{x}_{\mathrm{DG}}^{\bullet i} = \mathbf{A}_{\mathrm{DG}}^{i} \Delta \mathbf{x}_{\mathrm{DG}}^{i} + \mathbf{B}_{\mathrm{DG}}^{i} \Delta \mathbf{u}_{\mathrm{DG}}^{i} + \mathbf{C}_{\mathrm{DG}}^{i} \Delta \mathbf{v}_{\mathrm{DG}}^{i} \tag{3.52}$$

in which $\mathbf{x}_{\mathrm{DG}} = [i^{1\mathrm{d}}\ \ i^{1\mathrm{q}}\ \ i^{2\mathrm{d}}\ i^{2\mathrm{q}}\ \ v^{\mathrm{cd}}\ \ v^{\mathrm{cq}}\ ]^T$ and $\Delta\mathbf{u}_{\mathrm{DG}}^{i}$ denote the equivalent input control signal vector of (3.44) whereas $\Delta\mathbf{v}_{\mathrm{DG}}^{i}$ denotes the voltage vector of the DG bus in dq frame.

The expanded form of (3.52a) is

$$\Delta\begin{bmatrix} i_1^{\mathrm{d}} \\ i_1^{\mathrm{q}} \\ i_2^{\mathrm{d}} \\ i_2^{\mathrm{q}} \\ v_{\mathrm{c}}^{\mathrm{d}} \\ v_{\mathrm{c}}^{\mathrm{q}} \end{bmatrix}^{\bullet} = \begin{bmatrix} \frac{-R_{\mathrm{f}}}{L_{\mathrm{f}}} & \omega & 0 & 0 & \frac{-1}{L_{\mathrm{f}}} & 0 \\ -\omega & \frac{-R_{\mathrm{f}}}{L_{\mathrm{f}}} & 0 & 0 & 0 & \frac{-1}{L_{\mathrm{f}}} \\ 0 & 0 & 0 & \omega & \frac{1}{L_{\mathrm{f}}} & 0 \\ 0 & 0 & -\omega & 0 & 0 & \frac{1}{L_{\mathrm{f}}} \\ \frac{1}{C_{\mathrm{f}}} & 0 & \frac{-1}{C_{\mathrm{f}}} & 0 & 0 & \omega \\ 0 & \frac{1}{C_{\mathrm{f}}} & 0 & \frac{-1}{C_{\mathrm{f}}} & -\omega & 0 \end{bmatrix} \times \Delta\begin{bmatrix} i_1^{\mathrm{d}} \\ i_1^{\mathrm{q}} \\ i_2^{\mathrm{d}} \\ i_2^{\mathrm{q}} \\ v_{\mathrm{c}}^{\mathrm{d}} \\ v_{\mathrm{c}}^{\mathrm{q}} \end{bmatrix} + \frac{aV_{\mathrm{dc}}}{L_{\mathrm{f}}}\begin{bmatrix} 1 & 0 \\ 0 & 1 \\ 0 & 0 \\ 0 & 0 \\ 0 & 0 \\ 0 & 0 \end{bmatrix} \times \Delta\begin{bmatrix} u^{\mathrm{d}} \\ u^{\mathrm{q}} \end{bmatrix} - \frac{1}{L_{\mathrm{T}}}\begin{bmatrix} 0 & 0 \\ 0 & 0 \\ 1 & 0 \\ 0 & 1 \\ 0 & 0 \\ 0 & 0 \end{bmatrix} \times \Delta\begin{bmatrix} v_{\mathrm{t}}^{\mathrm{d}} \\ v_{\mathrm{t}}^{\mathrm{q}} \end{bmatrix} \tag{3.52b}$$

Assuming a BES has the same voltage source converter and filter structure and control of a DG, the state-space representation of BES-*i* will be

$$\Delta\mathbf{x}_{\mathrm{BES}}^{\bullet i} = \mathbf{A}_{\mathrm{BES}}^{i}\Delta\mathbf{x}_{\mathrm{BES}}^{i} + \mathbf{B}_{\mathrm{BES}}^{i}\Delta\mathbf{u}_{\mathrm{BES}}^{i} + \mathbf{C}_{\mathrm{BES}}^{i}\Delta\mathbf{v}_{\mathrm{BES}}^{i} \tag{3.53}$$

In the case voltage source converters with different control and structure are implemented for the DGs or BESs, the appropriate state-space explanation shall be used in place of (3.52) or (3.53).

Here, the loads are presumed to be RL constant-impedance type; thereby, load-*i*'s state-space description can be presented as

$$\Delta\mathbf{x}_{\mathrm{load}}^{\bullet i} = \mathbf{A}_{\mathrm{load}}^{i}\,\Delta\mathbf{x}_{\mathrm{load}}^{i} + \mathbf{C}_{\mathrm{load}}^{i}\Delta\mathbf{v}_{\mathrm{load}}^{i} \tag{3.54a}$$

as expanded in

$$\Delta\begin{bmatrix} i^{\mathrm{d}} \\ i^{\mathrm{q}} \end{bmatrix}^{\bullet} = \begin{bmatrix} -R_{\mathrm{load}}/L_{\mathrm{load}} & \omega \\ -\omega & -R_{\mathrm{load}}/L_{\mathrm{load}} \end{bmatrix} \times \Delta\begin{bmatrix} i^{\mathrm{d}} \\ i^{\mathrm{q}} \end{bmatrix} + \frac{1}{L_{\mathrm{load}}}\begin{bmatrix} 1 & 0 \\ 0 & 1 \end{bmatrix} \times \Delta\begin{bmatrix} v_{\mathrm{t}}^{\mathrm{d}} \\ v_{\mathrm{t}}^{\mathrm{q}} \end{bmatrix} \tag{3.54b}$$

while the method of [144-145] can be used if the loads are assumed to be constant-power or induction motor type. This study also assumes constant-impedance RL branches for the lines. Thus, line-*i*'s state-space explanation when connected between bus-*j* and bus-*k* can be given by

$$\Delta\mathbf{x}_{\mathrm{line}}^{\bullet i} = \mathbf{A}_{\mathrm{line}}^{i}\,\Delta\mathbf{x}_{\mathrm{line}}^{i} + \mathbf{C}_{\mathrm{line}}^{i}\,\Delta\mathbf{v}_{\mathrm{MG}} \tag{3.55a}$$

as expanded in

$$\Delta\begin{bmatrix} i^{\mathrm{d}} \\ i^{\mathrm{q}} \end{bmatrix}^{\bullet} = \begin{bmatrix} -R_{\mathrm{line}}/L_{\mathrm{line}} & \omega \\ -\omega & -R_{\mathrm{line}}/L_{\mathrm{line}} \end{bmatrix} \times \Delta\begin{bmatrix} i^{\mathrm{d}} \\ i^{\mathrm{q}} \end{bmatrix} + \frac{1}{L_{\mathrm{line}}}\begin{bmatrix} \overbrace{\mathbf{O}_2..\mathbf{O}_2}^{\mathrm{bus}(1)\ \mathrm{to}\ \mathrm{bus}(j-1)} & \overbrace{\mathbf{I}_2}^{\mathrm{bus}(j)} & \overbrace{\mathbf{O}_2..\mathbf{O}_2}^{\mathrm{bus}(j+1)\ \mathrm{to}\ \mathrm{bus}(k-1)} & \overbrace{-\mathbf{I}_2}^{\mathrm{bus}(k)} & \overbrace{\mathbf{O}_2..\mathbf{O}_2}^{\mathrm{bus}(k+1)\ \mathrm{to}\ \mathrm{bus}(N_{\mathrm{bus}})} \end{bmatrix} \times \Delta\begin{bmatrix} \overbrace{(v_{\mathrm{t}}^{\mathrm{d}})^1(v_{\mathrm{t}}^{\mathrm{q}})^1}^{\mathrm{bus}(1)} .. \overbrace{(v_{\mathrm{t}}^{\mathrm{d}})^{j-1}(v_{\mathrm{t}}^{\mathrm{q}})^{j-1}}^{\mathrm{bus}(j-1)} \overbrace{(v_{\mathrm{t}}^{\mathrm{d}})^{j}(v_{\mathrm{t}}^{\mathrm{q}})^{j}}^{\mathrm{bus}(j)} \overbrace{(v_{\mathrm{t}}^{\mathrm{d}})^{j+1}(v_{\mathrm{t}}^{\mathrm{q}})^{j+1}}^{\mathrm{bus}(j+1)} \dots \\ \underbrace{(v_{\mathrm{t}}^{\mathrm{d}})^{k-1}(v_{\mathrm{t}}^{\mathrm{q}})^{k-1}}_{\mathrm{bus}(k-1)} \underbrace{(v_{\mathrm{t}}^{\mathrm{d}})^{k}(v_{\mathrm{t}}^{\mathrm{q}})^{k}}_{\mathrm{bus}(k)} \underbrace{(v_{\mathrm{t}}^{\mathrm{d}})^{k+1}(v_{\mathrm{t}}^{\mathrm{q}})^{k+1}}_{\mathrm{bus}(k+1)} .. \underbrace{(v_{\mathrm{t}}^{\mathrm{d}})^{N_{\mathrm{bus}}}(v_{\mathrm{t}}^{\mathrm{q}})^{N_{\mathrm{bus}}}}_{\mathrm{bus}(N_{\mathrm{bus}})} \end{bmatrix} \tag{3.55b}$$

Merging the state-space explanation of microgrid's components from (3.51)-(3.55) yields the equivalent state-space equation of

$$\Delta\mathbf{x}_{\mathrm{MG}}^{\bullet 1} = \mathbf{A}_{\mathrm{MG}}^{1}\Delta\mathbf{x}_{\mathrm{MG}}^{1} + \mathbf{B}_{\mathrm{MG}}^{1}\Delta\mathbf{u}_{\mathrm{MG}} + \mathbf{C}_{\mathrm{MG}}^{1}\,\Delta\mathbf{v}_{\mathrm{MG}} \tag{3.56}$$

in which

$$\mathbf{x}_{\mathrm{MG}}^{1} = \begin{bmatrix} \overbrace{\mathbf{x}_{\mathrm{SG}}^{1} \dots \mathbf{x}_{\mathrm{SG}}^{N_{\mathrm{SG}}}}^{\mathrm{SGs}} & \overbrace{\mathbf{x}_{\mathrm{DG}}^{1} \dots \mathbf{x}_{\mathrm{DG}}^{N_{\mathrm{DG}}}}^{\mathrm{DGs}} & \overbrace{\mathbf{x}_{\mathrm{BES}}^{1} \dots \mathbf{x}_{\mathrm{BES}}^{N_{\mathrm{BES}}}}^{\mathrm{BESs}} & \overbrace{\mathbf{x}_{\mathrm{load}}^{1} \dots \mathbf{x}_{\mathrm{load}}^{N_{\mathrm{load}}}}^{\mathrm{Loads}} & \overbrace{\mathbf{x}_{\mathrm{line}}^{1} \dots \mathbf{x}_{\mathrm{line}}^{N_{\mathrm{line}}}}^{\mathrm{Lines}} \end{bmatrix}^{T}$$

$$\mathbf{A}_{\mathrm{MG}}^{1} = \mathrm{diag}\left(\overbrace{\mathbf{A}_{\mathrm{SG}}^{1} \dots \mathbf{A}_{\mathrm{SG}}^{N_{\mathrm{SG}}}}^{\mathrm{SGs}} \overbrace{\mathbf{A}_{\mathrm{DG}}^{1} \dots \mathbf{A}_{\mathrm{DG}}^{N_{\mathrm{DG}}}}^{\mathrm{DGs}} \overbrace{\mathbf{A}_{\mathrm{BES}}^{1} \dots \mathbf{A}_{\mathrm{BES}}^{N_{\mathrm{BES}}}}^{\mathrm{BESs}} \overbrace{\mathbf{A}_{\mathrm{load}}^{1} \dots \mathbf{A}_{\mathrm{load}}^{N_{\mathrm{load}}}}^{\mathrm{Loads}} \overbrace{\mathbf{A}_{\mathrm{line}}^{1}, \dots, \mathbf{A}_{\mathrm{line}}^{N_{\mathrm{line}}}}^{\mathrm{Lines}} \right)$$

$$\mathbf{B}_{\mathrm{MG}}^{1}=\begin{bmatrix}\mathrm{diag}\left(\overbrace{\mathbf{B}_{\mathrm{SG}}^{1}\ \ldots\ \mathbf{B}_{\mathrm{SG}}^{N_{\mathrm{SG}}}}^{\text{SGs}}\ \overbrace{\mathbf{B}_{\mathrm{DG}}^{1}\ \ldots\ \mathbf{B}_{\mathrm{DG}}^{N_{\mathrm{DG}}}}^{\text{DGs}}\ \overbrace{\mathbf{B}_{\mathrm{BES}}^{1}\ \ldots\ \mathbf{B}_{\mathrm{BES}}^{N_{\mathrm{BES}}}}^{\text{BESs}}\right)\\ \mathbf{O}_{2(N_{\mathrm{load}}+N_{\mathrm{line}})\times 6(N_{\mathrm{SG}}+N_{\mathrm{DG}}+N_{\mathrm{BES}})}\end{bmatrix}$$

$$\mathbf{C}_{\mathrm{MG}}^{1}=\begin{bmatrix}\mathrm{diag}\left(\overbrace{\mathbf{C}_{\mathrm{SG}}^{1}\ \ldots\mathbf{C}_{\mathrm{SG}}^{N_{\mathrm{SG}}}}^{\text{SGs}}\ \overbrace{\mathbf{C}_{\mathrm{DG}}^{1}\ \ldots\mathbf{C}_{\mathrm{DG}}^{N_{\mathrm{DG}}}}^{\text{DGs}}\ \overbrace{\mathbf{C}_{\mathrm{BES}}^{1}\ \ldots\mathbf{C}_{\mathrm{BES}}^{N_{\mathrm{BES}}}}^{\text{BESs}}\ \overbrace{\mathbf{C}_{\mathrm{load}}^{1}\ \ldots\mathbf{C}_{\mathrm{load}}^{N_{\mathrm{load}}}}^{\text{Loads}}\right)\\ \mathbf{C}_{\mathrm{line}}^{1}\\ \vdots\\ \mathbf{C}_{\mathrm{line}}^{N_{\mathrm{line}}}\end{bmatrix}$$

$$\Delta\mathbf{u}_{\mathrm{MG}}=\Delta\left[\mathbf{u}_{\mathrm{SG}}\ \ \mathbf{z}^{\mathrm{ref}}\right]^{T}=\Delta\left[\overbrace{\mathbf{u}_{\mathrm{SG}}^{1}\ldots\mathbf{u}_{\mathrm{SG}}^{N_{\mathrm{SG}}}}^{\text{SGs}}\ \overbrace{(\mathbf{z}_{\mathrm{DG}}^{1})^{\mathrm{ref}}\ldots(\mathbf{z}_{\mathrm{DG}}^{N_{\mathrm{DG}}})^{\mathrm{ref}}}^{\text{DGs}}\ \overbrace{(\mathbf{z}_{\mathrm{BES}}^{1})^{\mathrm{ref}}\ldots(\mathbf{z}_{\mathrm{BES}}^{N_{\mathrm{BES}}})^{\mathrm{ref}}}^{\text{BESs}}\right]^{T}$$

while $\mathbf{O}_{\mathrm{x\times y}}$ denotes a zero matrix with an order of x×y.

The missing components in (3.56) are the powers of synchronous generators, DGs and BESs, plus the angles of the bus voltages along with the SoCs of BESs. The output active power of a synchronous generator [166], as well as the output active and reactive power of a DG [135], can be calculated from

$$P_{\mathrm{SG}}=\frac{1.5N_{\mathrm{p}}\omega}{2\omega_{\mathrm{b}}}\left[X_{\mathrm{md}}i^{\mathrm{q}}\left(-i^{\mathrm{d}}+i^{\mathrm{fd}}+i^{\mathrm{kd}}\right)-X_{\mathrm{mq}}i^{\mathrm{d}}\left(-i^{\mathrm{q}}+i^{\mathrm{k1q}}+i^{\mathrm{k2q}}\right)\right] \tag{3.57a}$$

which can be linearised around their operating (equilibrium) points as

$$\Delta\dot{P}_{\mathrm{SG}}^{i}=\mathbf{B}_{\mathrm{P\text{-}SG}}^{i}\,\Delta\mathbf{x}_{\mathrm{SG}}^{i} \tag{3.57b}$$

as expanded in

$$\Delta\dot{P}=\frac{3\omega_{\circ}}{2\omega_{\mathrm{b}}}\left[\alpha_{1}\quad\alpha_{2}\quad-X_{\mathrm{mq}}(i^{\mathrm{d}})_{\circ}\quad-X_{\mathrm{mq}}(i^{\mathrm{d}})_{\circ}\quad X_{\mathrm{md}}(i^{\mathrm{q}})_{\circ}\quad X_{\mathrm{md}}(i^{\mathrm{q}})_{\circ}\right]\times$$
$$\Delta\left[i^{\mathrm{q}}\ \ i^{\mathrm{d}}\ \ i^{\mathrm{k1q}}\ \ i^{\mathrm{k2q}}\ \ i^{\mathrm{fd}}\ \ i^{\mathrm{kd}}\right]^{T} \tag{3.57c}$$

where $\alpha_{1}=X_{\mathrm{md}}\left((-i^{\mathrm{d}})_{\circ}+(i^{\mathrm{fd}})_{\circ}+(i^{\mathrm{kd}})_{\circ}\right)+X_{\mathrm{mq}}(i^{\mathrm{d}})_{\circ}$

$$\alpha_{2}=-X_{\mathrm{md}}(i^{\mathrm{q}})_{\circ}+X_{\mathrm{mq}}\left((i^{\mathrm{q}})_{\circ}-(i^{\mathrm{k1q}})_{\circ}-(i^{\mathrm{k2q}})_{\circ}\right)^{T}$$

Likewise, the output active power of a DG [135] can be calculated from

$$p_{\mathrm{DG}}=1.5\left(i_{2}^{\mathrm{d}}v_{\mathrm{c}}^{\mathrm{d}}+i_{2}^{\mathrm{q}}v_{\mathrm{c}}^{\mathrm{q}}\right) \tag{3.58a}$$

which can be linearized around their operating (equilibrium) points as

$$\Delta\dot{P}_{\mathrm{DG}}^{i}=-\omega_{\mathrm{c}}^{i}\,\Delta P_{\mathrm{DG}}^{i}+\mathbf{B}_{\mathrm{P\text{-}DG}}^{i}\,\Delta\mathbf{x}_{\mathrm{DG}}^{i} \tag{3.58b}$$

as expanded in

$$\Delta\dot{P} = -\omega_c \Delta P + \frac{3}{2}\omega_c \left[0 \quad 0 \quad (v_c^d)_o \quad (v_c^q)_o \quad (i_2^d)_o \quad (i_2^q)_o\right] \times \Delta\left[i_1^d \quad i_1^q \quad i_2^d \quad i_2^q \quad v_c^d \quad v_c^q\right]^T \tag{3.58c}$$

the reactive power of a DG [135] can be calculated from

$$q_{DG} = 1.5\left(i_2^d v_c^q - i_2^q v_c^d\right) \tag{3.59a}$$

which can be linearized around their operating (equilibrium) points as

$$\Delta\dot{Q}_{DG}^{\,i} = -\omega_c^i \, \Delta Q_{DG}^i + \mathbf{B}_{P\text{-}DG}^i \, \Delta\mathbf{x}_{DG}^i \tag{3.59b}$$

as expanded in

$$\Delta\dot{Q} = -\omega_c \Delta Q + \frac{3}{2}\omega_c \left[0 \quad 0 \quad (v_c^q)_o \quad -(v_c^d)_o \quad -(i_2^q)_o \quad (i_2^d)_o\right] \times \Delta\left[i_1^d \quad i_1^q \quad i_2^d \quad i_2^q \quad v_c^d \quad v_c^q\right]^T \tag{3.59c}$$

It is to be noted that when calculating (3.58b) from (3.58a) and (3.59b) from (3.59a), the impact of the assumed low pass filter with a cut-off frequency of ω_c has been taken into account. The output active and reactive power of a BES is same as that for a DG; thus,

$$\Delta\dot{P}_{BES}^{\,i} = -\omega_c^i \, \Delta P_{BES}^i + \mathbf{B}_{P\text{-}BES}^i \, \Delta\mathbf{x}_{BES}^i \tag{3.60a}$$

$$\Delta\dot{Q}_{BES}^{\,i} = -\omega_c^i \, \Delta Q_{BES}^i + \mathbf{B}_{P\text{-}BES}^i \, \Delta\mathbf{x}_{BES}^i \tag{3.60b}$$

Also, the voltage angles at the output of each synchronous generator, DG and BES can be derived from its angular frequency ω against a global (common) angular frequency of ω_{com} as [133-134]

$$\delta = \int(\omega - \omega_{com})\,dt \tag{3.61}$$

in which $\omega_{com} = m_{com}P_{com}$ is the angular frequency of one of the sources (e.g., $\omega_{com} = \omega_1$). Differentiating (3.61) and linearizing that for every synchronous generator, DG and BES yields

$$\Delta\dot{\delta}_{SG}^{\,i} = -m'^{\,i}_{SG} \, \Delta P_{SG}^i + m'_{com} \, \Delta P_{com} \tag{3.62a}$$

$$\Delta\dot{\delta}_{DG}^{\,i} = -m'^{\,i}_{DG} \, \Delta P_{DG}^i + m'_{com} \, \Delta P_{com} \tag{3.62b}$$

$$\Delta\dot{\delta}_{BES}^{\,i} = -m'^{\,i}_{BES} \, \Delta P_{BES}^i + m'_{com} \, \Delta P_{com} \tag{3.62c}$$

in which $m' = 2\pi m$.

On the other hand, a BES is characterized by its SoC value, which can be calculated from [135]

$$SoC = SoC^{\text{int}} - \int p_{\text{BES}} dt \Big/ E^{\text{cap}} \tag{3.63}$$

in which SoC^{int} and E^{cap} are respectively the BES's initial SoC, and capacity of energy storage. Differentiating (3.63) and linearising that, one gets

$$\Delta \dot{SoC}^{\,i}_{\text{BES}} = \mathbf{B}^{i}_{\text{SoC-BES}}\, \Delta \mathbf{x}^{i}_{\text{BES}} \tag{3.64a}$$

as expanded in

$$\Delta \dot{SoC} = \frac{-3}{2E^{\text{cap}}} \begin{bmatrix} 0 & 0 & (v_{\text{c}}^{\text{d}})_{\text{o}} & (v_{\text{c}}^{\text{q}})_{\text{o}} & (i_2^{\text{d}})_{\text{o}} & (i_2^{\text{q}})_{\text{o}} \end{bmatrix} \times \Delta \begin{bmatrix} i_1^{\text{d}} & i_1^{\text{q}} & i_2^{\text{d}} & i_2^{\text{q}} & v_{\text{c}}^{\text{d}} & v_{\text{c}}^{\text{q}} \end{bmatrix}^T \tag{3.64b}$$

Now, merging (3.57b), (3.58b), (3.59b), (3.60), (3.62) and (3.64a) one gets

$$\Delta \mathbf{x}^{\bullet 2}_{\text{MG}} = \mathbf{A}'^{2}_{\text{MG}} \Delta \mathbf{x}^{2}_{\text{MG}} + \mathbf{B}^{2}_{\text{MG}}\, \Delta \mathbf{x}^{1}_{\text{MG}} + \mathbf{D}^{2}_{\text{MG}}\, \Delta P_{\text{com}} \tag{3.65}$$

in which

$$\mathbf{x}^{2}_{\text{MG}} = \Big[\overbrace{P^1_{\text{SG}} \dots P^{N_{\text{SG}}}_{\text{SG}}}^{\text{SGs}} \overbrace{P^1_{\text{DG}} \dots P^{N_{\text{DG}}}_{\text{DG}}}^{\text{DGs}} \overbrace{P^1_{\text{BES}} \dots P^{N_{\text{BES}}}_{\text{BES}}}^{\text{BESs}} \overbrace{Q^1_{\text{DG}} \dots Q^{N_{\text{DG}}}_{\text{DG}}}^{\text{DGs}} \overbrace{Q^1_{\text{BES}} \dots Q^{N_{\text{BES}}}_{\text{BES}}}^{\text{BESs}} \overbrace{\delta^1_{\text{SG}} \dots \delta^{N_{\text{SG}}}_{\text{SG}}}^{\text{SGs}} \overbrace{\delta^1_{\text{DG}} \dots \delta^{N_{\text{DG}}}_{\text{DG}}}^{\text{DGs}} \overbrace{\delta^1_{\text{BES}} \dots \delta^{N_{\text{BES}}}_{\text{BES}}}^{\text{BESs}} \overbrace{SoC^1_{\text{BES}} \dots SoC^{N_{\text{BES}}}_{\text{BES}}}^{\text{BESs}} \Big]^T$$

$$\mathbf{A}'^{2}_{\text{MG}} = \text{diag}\Big(\overbrace{\mathbf{O}_{N_{\text{SG}} \times N_{\text{SG}}}}^{\text{SGs}} \overbrace{-\omega^1_{\text{c}} \dots -\omega^{N_{\text{DG}}}_{\text{c}}}^{\text{DGs}} \overbrace{-\omega^1_{\text{c}} \dots -\omega^{N_{\text{BES}}}_{\text{c}}}^{\text{BESs}} \overbrace{-\omega^1_{\text{c}} \dots -\omega^{N_{\text{DG}}}_{\text{c}}}^{\text{DGs}} \overbrace{-\omega^1_{\text{c}} \dots -\omega^{N_{\text{BES}}}_{\text{c}}}^{\text{BESs}} \overbrace{-m'^{1}_{\text{SG}} \dots -m'^{N_{\text{SG}}}_{\text{SG}}}^{\text{SGs}} \overbrace{-m'^{1}_{\text{DG}} \dots -m'^{N_{\text{DG}}}_{\text{DG}}}^{\text{DGs}} \overbrace{-m'^{1}_{\text{BES}} \dots -m'^{N_{\text{BES}}}_{\text{BES}}}^{\text{BESs}} \overbrace{\mathbf{O}_{N_{\text{BES}} \times N_{\text{BES}}}}^{\text{BESs}} \Big)$$

$$\mathbf{B}^{2}_{\text{MG}} = \text{diag}\Big(\overbrace{\mathbf{B}^1_{\text{P-SG}} \dots \mathbf{B}^{N_{\text{SG}}}_{\text{P-SG}}}^{\text{SGs}} \overbrace{\mathbf{B}^1_{\text{P-DG}} \dots \mathbf{B}^{N_{\text{DG}}}_{\text{P-DG}}}^{\text{DGs}} \overbrace{\mathbf{B}^1_{\text{P-BES}} \dots \mathbf{B}^{N_{\text{BES}}}_{\text{P-BES}}}^{\text{BESs}} \overbrace{\mathbf{B}^1_{\text{Q-DG}} \dots \mathbf{B}^{N_{\text{DG}}}_{\text{Q-DG}}}^{\text{DGs}} \overbrace{\mathbf{B}^1_{\text{Q-BES}} \dots \mathbf{B}^{N_{\text{BES}}}_{\text{Q-BES}}}^{\text{BESs}} \overbrace{\mathbf{O}_{(N_{\text{SG}}+N_{\text{DG}}+N_{\text{BES}}) \times 6(N_{\text{SG}}+N_{\text{DG}}+N_{\text{BES}})}}^{\text{SGs \& DGs \& BESs}} \overbrace{\mathbf{B}^1_{\text{SoC-BES}} \dots \mathbf{B}^{N_{\text{BES}}}_{\text{SoC-BES}}}^{\text{BESs}} \Big)$$

$$\mathbf{D}^{2}_{\text{MG}} = \begin{bmatrix} \mathbf{O}_{(N_{\text{SG}}+2(N_{\text{DG}}+N_{\text{BES}})) \times 1} & \overbrace{m'_{\text{com}} \dots m'_{\text{com}}}^{N_{\text{SG}}+N_{\text{DG}}+N_{\text{BES}}} & \mathbf{O}_{N_{\text{BES}} \times 1} \end{bmatrix}$$

Since $\Delta P_{\text{com}} = \Delta P_1$, $\mathbf{D}^2_{\text{MG}}$ will be added to column-1 of $\mathbf{A'}^2_{\text{MG}}$ to form $\mathbf{A}^2_{\text{MG}}$. Consequently, (3.65) becomes

$$\Delta \mathbf{x}^{\bullet 2}_{\text{MG}} = \mathbf{A}^2_{\text{MG}} \Delta \mathbf{x}^2_{\text{MG}} + \mathbf{B}^2_{\text{MG}} \Delta \mathbf{x}^1_{\text{MG}} \tag{3.66}$$

Two matrices of $\Delta \mathbf{u}_{\text{SG}}$ and $(\Delta \mathbf{z})^{\text{ref}}$ were not defined in (3.56). To determine $(\Delta \mathbf{z})^{\text{ref}}$, (3.45) can be stated in dq frame, transformed into the global dq frame and then linearized to yield $\left(\Delta \mathbf{z}^i_{\text{DG}}\right)^{\text{ref}}$ and $\left(\Delta \mathbf{z}^i_{\text{BES}}\right)^{\text{ref}}$ as [135]

$$(\Delta \mathbf{z}^i_{\text{DG}})^{\text{ref}} = [\mathbf{M}^i_{\text{1-DG}} \quad \mathbf{M}^i_{\text{2-DG}} \quad \mathbf{M}^i_{\text{3-DG}}] \times \Delta \mathbf{x'}^i_{\text{DG}} \tag{3.67a}$$

$$(\Delta \mathbf{z}^i_{\text{BES}})^{\text{ref}} = [\mathbf{M}^i_{\text{1-BES}} \quad \mathbf{M}^i_{\text{2-BES}} \quad \mathbf{M}^i_{\text{3-BES}}] \times \Delta \mathbf{x'}^i_{\text{BES}} \tag{3.67b}$$

where $\Delta \mathbf{x}'_{\text{DG}} = \Delta\left[P^i_{\text{DG}} \;\; Q^i_{\text{DG}} \;\; \delta^i_{\text{DG}}\right]^T$ and $\Delta \mathbf{x}'_{\text{BES}} = \Delta\left[P^i_{\text{BES}} \;\; Q^i_{\text{BES}} \;\; \delta^i_{\text{BES}}\right]^T$ and are expanded in

$$\mathbf{M}_1 = \begin{bmatrix} \dfrac{2\sin\delta_{\text{o}}}{3V_{\text{co}}} \\ \dfrac{-2\cos\delta_{\text{o}}}{3V_{\text{co}}} \\ 0 \\ 0 \\ 0 \\ 0 \end{bmatrix}, \quad \mathbf{M}_2 = \begin{bmatrix} \dfrac{-2\left[V_{\text{co}}\cos\delta_{\text{o}} + n\left(Q_{\text{o}}\cos\delta_{\text{o}} - P_{\text{o}}\sin\delta_{\text{o}}\right)\right]}{3V^2_{\text{co}}} \\ \dfrac{-2\left[V_{\text{co}}\sin\delta_{\text{o}} + n\left(Q_{\text{o}}\sin\delta_{\text{o}} + P_{\text{o}}\cos\delta_{\text{o}}\right)\right]}{3V^2_{\text{co}}} \\ -C_{\text{f}} n\omega\cos\delta_{\text{o}} \\ -C_{\text{f}} n\omega\sin\delta_{\text{o}} \\ -n\sin\delta_{\text{o}} \\ n\cos\delta_{\text{o}} \end{bmatrix}, \tag{3.67c}$$

$$\mathbf{M}_3 = \begin{bmatrix} \dfrac{2\left(Q_{\text{o}}\sin\delta_{\text{o}} + P_{\text{o}}\cos\delta_{\text{o}}\right)}{3V_{\text{co}}} \\ \dfrac{-2\left(Q_{\text{o}}\cos\delta_{\text{o}} - P_{\text{o}}\sin\delta_{\text{o}}\right)}{3V_{\text{co}}} \\ -C_{\text{f}} V_{\text{co}}\omega\sin\delta_{\text{o}} \\ C_{\text{f}} V_{\text{co}}\omega\cos\delta_{\text{o}} \\ V_{\text{co}}\cos\delta_{\text{o}} \\ V_{\text{co}}\sin\delta_{\text{o}} \end{bmatrix}$$

where $_{\text{o}}$ represents the value of each state at the operating point, and $V_{\text{co}} = (|V_{\text{c}}|_{\text{DG}})_{\text{o}}$ is calculated from (3.46b), while $P_{\text{o}} = (P_{\text{DG}})_{\text{o}}$ and $Q_{\text{o}} = (Q_{\text{DG}})_{\text{o}}$ are calculated from (3.58a) and (3.59a) respectively,

In a more inclusive form, (3.67) becomes

$$(\Delta \mathbf{z})^{\text{ref}} = \mathbf{M}\, \mathbf{x}^2_{\text{MG}} \tag{3.68}$$

Considering all DGs and BESs of the microgrid in which

$$\mathbf{M}=\begin{bmatrix} \overbrace{\text{diag}\left(\mathbf{M}_{\text{1-DG}}^{1},...,\mathbf{M}_{\text{1-DG}}^{N_{\text{DG}}}\right)}^{\text{DGs}} & \overbrace{\text{diag}\left(\mathbf{M}_{\text{1-BES}}^{1},...,\mathbf{M}_{\text{1-BES}}^{N_{\text{BES}}}\right)}^{\text{BESs}} & \overbrace{\text{diag}\left(\mathbf{M}_{\text{2-DG}}^{1},...,\mathbf{M}_{\text{2-DG}}^{N_{\text{DG}}}\right)}^{\text{DGs}} \\ \overbrace{\text{diag}\left(\mathbf{M}_{\text{2-BES}}^{1},...,\mathbf{M}_{\text{2-BES}}^{N_{\text{BES}}}\right)}^{\text{BESs}} & \overbrace{\text{diag}\left(\mathbf{M}_{\text{3-DG}}^{1},...,\mathbf{M}_{\text{3-DG}}^{N_{\text{DG}}}\right)}^{\text{DGs}} & \overbrace{\text{diag}\left(\mathbf{M}_{\text{3-BES}}^{1},...,\mathbf{M}_{\text{3-BES}}^{N_{\text{BES}}}\right)}^{\text{BESs}} \end{bmatrix}$$

Furthermore, $\Delta\mathbf{u}_{\text{SG}}=\mathbf{X}_{\text{R}}\,\Delta\mathbf{x}_{\text{SG}}$ in which $\mathbf{X}_{\text{R}}=\text{diag}(\mathbf{X}_{\text{R}}^{1}\ldots\mathbf{X}_{\text{R}}^{N_{\text{SG}}})$; $\mathbf{X}_{\text{R}}^{i}$ being a zero matrix of order 6 in which the corresponding component to i_{fd} in $\mathbf{x}_{\text{SG}}$ (i.e., the array in the first row and the 5th column) is replaced by X_{md}^{i}. Thereby, $\Delta\mathbf{u}_{\text{MG}}$ in (3.56) can be rewritten as B' $\Delta\mathbf{u}'_{\text{MG}}$, where

$$\mathbf{B}'=\begin{bmatrix}\mathbf{X}_{\text{R}} & \mathbf{O}_{6N_{\text{SG}}\times 3(N_{\text{DG}}+N_{\text{BES}})}\\ \mathbf{O}_{6N_{\text{SG}}\times 6N_{\text{SG}}} & \mathbf{M}\end{bmatrix},\quad \mathbf{u}'_{\text{MG}}=\begin{bmatrix}\mathbf{x}_{\text{SG}}\\ \mathbf{x}_{\text{MG}}^{2}\end{bmatrix}$$

On the other hand, $\mathbf{B}_{\text{MG}}^{1}$ in (3.56) is in the form of

$$\mathbf{B}_{\text{MG}}^{1}=\begin{bmatrix}\mathbf{B}_{\text{SG}}^{1} & \mathbf{O}_{6N_{\text{SG}}\times(N_{\text{t}}-6N_{\text{SG}})}\\ \mathbf{O}_{(N_{\text{t}}-6N_{\text{SG}})\times 6N_{\text{SG}}} & \mathbf{B}_{\text{DG}}^{1}\end{bmatrix}$$

in which $N_{\text{t}}=6N_{\text{SG}}+6N_{\text{DG}}+6N_{\text{BES}}+2N_{\text{load}}+2N_{\text{line}}$. Thereby, the microgrid's overall linearized state-space explanation, consisting of all states, can be achieved by merging (3.56) and (3.65) as

$$\Delta\dot{\mathbf{x}}_{\text{MG}}=\mathbf{A}_{\text{MG}}\Delta\mathbf{x}_{\text{MG}}+\mathbf{C}_{\text{MG}}\Delta\mathbf{v}_{\text{MG}} \tag{3.69}$$

in which

$$\mathbf{x}_{\text{MG}}=\begin{bmatrix}\mathbf{x}_{\text{MG}}^{1}\\ \mathbf{x}_{\text{MG}}^{2}\end{bmatrix},\mathbf{A}_{\text{MG}}=\begin{bmatrix}\mathbf{A}_{\text{MG}}^{1}+\mathbf{B}_{\text{SG}}^{1}\mathbf{X}_{\text{R}} & \mathbf{B}_{\text{DG}}^{1}\mathbf{M}\\ \mathbf{B}_{\text{MG}}^{2} & \mathbf{A}_{\text{MG}}^{2}\end{bmatrix},\mathbf{C}_{\text{MG}}=\begin{bmatrix}\mathbf{C}_{\text{MG}}^{1}\\ \mathbf{O}_{(2N_{\text{SG}}+3N_{\text{DG}}+4N_{\text{BES}})\times 2N_{\text{bus}}}\end{bmatrix}$$

To further simplify (3.69), $\Delta\mathbf{v}_{\text{MG}}$ has to be expressed as a function of $\mathbf{x}_{\text{MG}}$. To this end, one can presume a large virtual resistance of $R_{\text{v}}=10^{4}$ between the ground and the microgrid's buses. Based on this assumption, the voltage at microgrid's bus-j can be given by

$$\Delta\mathbf{v}_{\text{bus}}^{j}=R_{\text{v}}\times\left(\begin{array}{l}\displaystyle\sum_{i=1}^{N_{\text{SG}}}\boldsymbol{\mu}_{\text{SG}}^{i}\Delta\begin{bmatrix}i^{\text{d}}\\ i^{\text{q}}\end{bmatrix}_{\text{SG}}^{i}+\sum_{i=1}^{N_{\text{DG}}}\boldsymbol{\mu}_{\text{DG}}^{i}\Delta\begin{bmatrix}i_{2}^{\text{d}}\\ i_{2}^{\text{q}}\end{bmatrix}_{\text{DG}}^{i}+\sum_{i=1}^{N_{\text{BES}}}\boldsymbol{\mu}_{\text{BES}}^{i}\Delta\begin{bmatrix}i_{2}^{\text{d}}\\ i_{2}^{\text{q}}\end{bmatrix}_{\text{BES}}^{i}\\ \qquad+\displaystyle\sum_{i=1}^{N_{\text{load}}}\boldsymbol{\mu}_{\text{load}}^{i}\Delta\begin{bmatrix}i^{\text{d}}\\ i^{\text{q}}\end{bmatrix}_{\text{load}}^{i}+\sum_{i=1}^{N_{\text{line}}}\boldsymbol{\mu}_{\text{line}}^{i}\Delta\begin{bmatrix}i^{\text{d}}\\ i^{\text{q}}\end{bmatrix}_{\text{line}}^{i}\end{array}\right) \tag{3.70a}$$

in which

$$\boldsymbol{\mu}_{\mathrm{SG}}^{i}=\begin{cases}\begin{bmatrix}0 & 1\\ 1 & 0\end{bmatrix} & \text{when SG-}i\text{ is attached to bus-}j\\ \mathbf{O}_2 & \text{else}\end{cases}$$

$$\boldsymbol{\mu}_{\mathrm{DG}}^{i}=\begin{cases}\mathbf{I}_2 & \text{when DG-}i\text{ is attached to bus-}j\\ \mathbf{O}_2 & \text{else}\end{cases}$$

$$\boldsymbol{\mu}_{\mathrm{load}}^{i}=\begin{cases}-\mathbf{I}_2 & \text{when load-}i\text{ is attached to bus-}j\\ \mathbf{O}_2 & \text{else}\end{cases} \tag{3.70b}$$

$$\boldsymbol{\mu}_{\mathrm{line}}^{i}=\begin{cases}\mathbf{I}_2 & \text{when line-}i\text{ enters bus-}j\\ -\mathbf{I}_2 & \text{when BES-}i\text{ leaves bus-}j\\ \mathbf{O}_2 & \text{else}\end{cases}$$

$$\boldsymbol{\mu}_{\mathrm{BES}}^{i}=\begin{cases}\mathbf{I}_2 & \text{when BES-}i\text{ is attached to bus-}j\text{ and is being discharge}\\ -\mathbf{I}_2 & \text{when BES-}i\text{ is attached to bus-}j\text{ and is being charged}\\ \mathbf{O}_2 & \text{else}\end{cases}$$

where $\mathbf{I}_2$ and $\mathbf{O}_2$ respectively symbolize an identity and square zero matrix of order 2. Calculating (3.70) for every bus within the microgrid, $\Delta\mathbf{v}_{\mathrm{MG}}$ can be presented by

$$\Delta\mathbf{v}_{\mathrm{MG}}=\mathbf{N}_{\mathrm{MG}}\,\Delta\mathbf{x}_{\mathrm{MG}} \tag{3.71}$$

in which $\mathbf{N}_{\mathrm{MG}}=[\mathbf{N}_{\mathrm{bus}}^{1}\ldots\mathbf{N}_{\mathrm{bus}}^{N_{\mathrm{bus}}}]^{T}$ while

$$\mathbf{N}_{\mathrm{bus}}^{j}=\Big[\overbrace{[\boldsymbol{\mu}^{\text{SG-1}}\ \mathbf{O}_{2\times4}]\ldots[\boldsymbol{\mu}^{\text{SG-}N_{\mathrm{SG}}}\mathbf{O}_{2\times4}]}^{\text{SGs}}\ \overbrace{[\mathbf{O}_2\ \boldsymbol{\mu}^{\text{DG-1}}\ \mathbf{O}_2]\ldots[\mathbf{O}_2\ \boldsymbol{\mu}^{\text{DG-}N_{\mathrm{DG}}}\mathbf{O}_2]}^{\text{DGs}}$$
$$\overbrace{[\mathbf{O}_2\ \boldsymbol{\mu}^{\text{BES-1}}\ \mathbf{O}_2]\ldots[\mathbf{O}_2\ \boldsymbol{\mu}^{\text{BES-}N_{\mathrm{BES}}}\mathbf{O}_2]}^{\text{BESs}}\overbrace{\boldsymbol{\mu}^{\text{load-1}}\ldots\boldsymbol{\mu}^{\text{load-}N_{\mathrm{load}}}}^{\text{loads}}$$
$$\overbrace{\boldsymbol{\mu}^{\text{line-1}}\ldots\boldsymbol{\mu}^{\text{line-}N_{\mathrm{line}}}}^{\text{lines}}\ \mathbf{O}_{2\times\left(2N_{\mathrm{SG}}+3N_{\mathrm{DG}}+4N_{\mathrm{BES}}\right)}\Big]$$

Substituting (3.71) in (3.69) yields

$$\Delta\mathbf{x}_{\mathrm{MG}}^{\bullet}=\mathbf{A}_{\mathrm{MG}}^{\mathrm{H}}\,\Delta\mathbf{x}_{\mathrm{MG}} \tag{3.71}$$

in which $\mathbf{A}_{\mathrm{MG}}^{\mathrm{H}}=\mathbf{A}_{\mathrm{MG}}+\mathbf{C}_{\mathrm{MG}}\mathbf{N}_{\mathrm{MG}}$ based on which the eigenvalues of the microgrid (λ) can be determined as the roots of $\det(\lambda\mathbf{I}-\mathbf{A}_{\mathrm{MG}}^{\mathrm{H}})$ in which det(.) represents the determinant function and $\mathbf{I}$ denotes the identity matrix of order $\mathbf{A}_{\mathrm{MG}}^{\mathrm{H}}$ [172]. The characteristics of the eigenvalues is presented in the section 7.3.

A sensitivity-type analysis is performed then in which m is increased from $0.1m_{\mathrm{o}}$ to $10m_{\mathrm{o}}$ around the operating point m_{o} to determine the very first m for which the

microgrid becomes marginally stable (denoted by m_{critical}) from which the microgrid's frequency stability index (FSI) can be defined as

$$FSI = \frac{m_{\text{critical-}i} P_{\text{DG-}i}^{\text{cap}}}{f^{\text{b}}} \tag{3.72}$$

Each synchronous generator possesses 6 current states, one power state, and one angle state, each DG exhibits 4 current states, two voltage states, two power states and one angle state, and each BES has an SoC state on the top of similar states to that of DGs while each load and line hold 2 states of currents. These total states correspond to the eigenvalues of the microgrid. The microgrid's stability can be assessed by spotting the trajectory of the eigenvalues on the *s*-plane based on which the microgrid can be classified as stable when all eigenvalues are situated on the left of the s-plane's imaginary axis [9]. The dominant eigenvalues are those situated in the proximity of the imaginary axis [133-134].

3.8 Summary

This chapter has presented the modelling of various power system components along with their detailed mathematical explanations, as well as the key employed analysis techniques. These components include conventional synchronous generators, DFIG-based wind generators, loads, FACTS based shunt and series devices, HVDC links and power oscillation damping controllers. Similarly, a microgrid network model is formulated with its sources like conventional synchronous generators, converter based DGs and BESs, lines and loads. These power system building components are explained and presented as detailed voltage and power equations so as to use for stability studies in the later chapters. Small signal model of a power system can be expressed in the form of nonlinear differential equations. The eigenvalues of the state matrix developed, provide dynamic behaviour of the power system under study. Among the eigenvalues, the complex pairs exhibit oscillatory modes existing in the power system. A participation factor analysis can be conducted, which gives the contribution of state variables to the oscillatory modes. This study helps to identify whether a particular state variable is contributing to an oscillatory mode. The techniques derived in this Chapter are used in Chapters 4 to 8 when demonstrating and validating the stability of a power system with a penetration of wind power.

Chapter 4 Voltage stability analysis of a distribution system

In this chapter, steady state and transient voltage stability issues of a weak distribution system with a remote DFIG-based wind farm is analysed. For the steady state voltage stability analysis of the distribution network, bus voltage analysis and active power-voltage analysis technique are used. From the study, it is observed that a wind farm can contribute enhancing maximum loading margin of distribution buses indicating an improvement in the voltage stability. Time domain simulation is conducted for the transient voltage stability analysis.

4.1 Test system

A modified 16-bus, 23 kV, 100 MVA distribution test system [173] as in Fig. 4.1 is used for the voltage stability analysis. The modification made to the test system is presented in Table 4.1-4.3. The distribution system is connected to a 23 kV, 50 Hz external grid through bus-1. As the influence of a wind farm into the distribution system stability is of the concern of this study, the loads (total of 28.7 MW and 17.3 MVAr) are modelled as constant impedance loads to achieve simplicity in the analysis. The test system is modified with an addition of three induction motors at bus-16 of capacity 1 MW each. The added motor loads simulate a remotely located large industrial/commercial load such as a mining company, agro-farm, etc., which are usually located far from the distribution load center in the real distribution network. This modified test system is considered as the base case for the study. At the base case, the system voltages are observed to be very low, with 0.9123 per unit (pu) at bus-16 and 0.9149 pu at bus-15.

A further modification to the test distribution system is made with an integration of a

wind farm. The wind farm consists of six DFIG-based wind turbines, each with 1.5 MW (total 9 MW capacity), operated at power factor control mode, and are connected to bus-16 through a 15 km cable. The wind farm is connected to the same bus at which the motor loads are connected so as to observe the effect of the wind farm on the large industrial load connected distribution network.

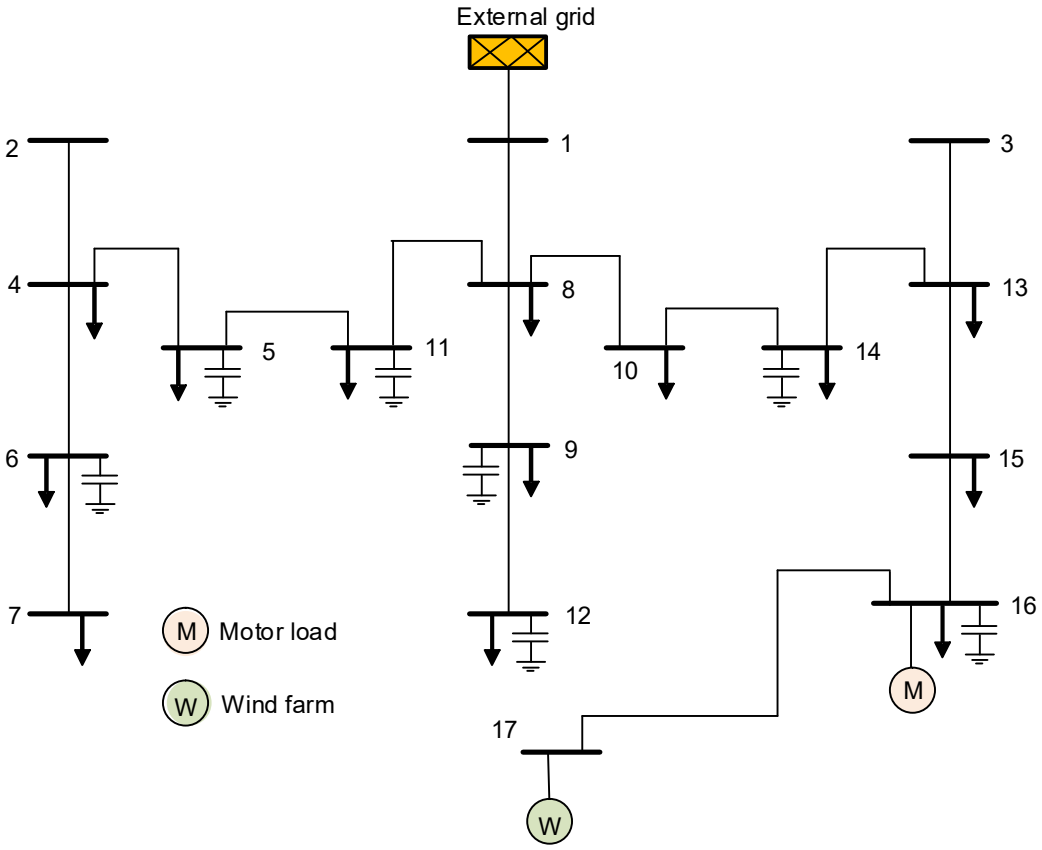

Figure 4.1 Modified distribution test system

Table 4.1 Parameters of the modified lines

Line	Resistance, Ω	Reactance, Ω	Capacitance, μF
bus-8 - bus-11	0.5819	0.5819	-
bus-16 - bus-17	1.47	1.71	0.302

Table 4.2 Parameters of wind farm

Power rating, S_n, MVA (6 units)	1.5
Stator resistance, r_s, Ω	0.0
Stator reactance, x_s, Ω	0.529
Rotor resistance, r_R, Ω	0.297
Rotor reactance, x_R, Ω	0.165
Magnetizing reactance, x_m, Ω	19.255

Table 4.3 Parameters of motor load

Power rating, S_n, MVA (3 units)	1.0
Stator resistance, r_s, Ω	0.0
Stator reactance, x_s, Ω	0.052
Rotor resistance, r_R, Ω	0.105
Rotor reactance, x_R, Ω	0.999
Magnetizing reactance, x_m, Ω	15.393

4.2 Steady state voltage stability analysis

In a weak distribution system, voltage instability may be originated by the lack of reactive power support and system characteristics. Bus voltage analysis and active power-voltage characteristic are studied with and without a remote DFIG-based wind farm to observe the effect of the wind farm in the steady state voltage stability of the distribution system.

4.2.1 Bus voltages analysis

Bus voltages are observed at the base case and with the integration of wind farm into the distribution network. An increase in the bus voltages is an indicator of the distribution system moving away from voltage instability point for steady state operation whereas a decrease in bus voltages indicates steady state voltage instability condition in the network. Fig. 4.2 shows that the voltages at all the buses are improved after the inclusion of the wind farm. It is worth mentioning that the voltage values shown in Figure 4.2 are a bit low for a normal distribution system. In reality, for the most distribution networks, the bus (substation) voltage values are higher than 1.0 pu. However, as the objective of the research is to study the impact of wind farms on the voltage stability of a weak distribution network, the bus voltages of below 1.0 pu are selected for this research. The voltage of bus-15 is improved from 0.9149 pu at base case to 0.9746 pu with the wind power integration. Similarly, the voltage of bus-7 is improved from 0.9178 pu at base case to 0.9343 pu. It is observed that the buses near the wind farm show better voltage improvement compared to the buses further away. For the study, the wind farm is considered to be operated at power factor control mode (0.95 lagging).

The overall voltage improvement of the distribution system, with the wind power

penetration, is an indication of the enhancement in the steady state voltage stability of the power network, which is further observed and verified in the section below through the active power-voltage characteristics analysis of the candidate buses in the network.

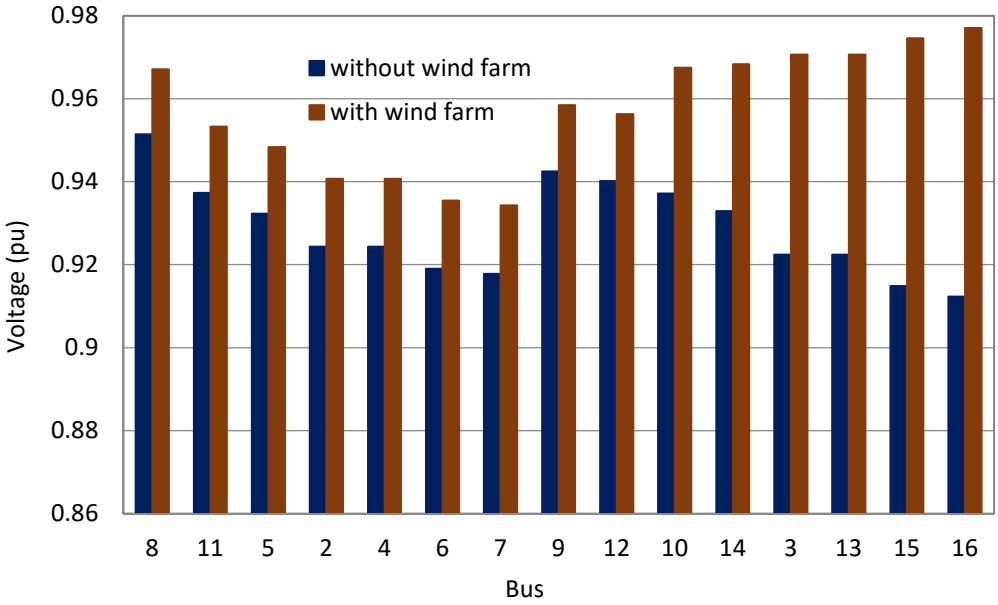

Figure 4.2 Bus voltages of the distribution system

4.2.2 Active power-voltage characteristics analysis

Voltage instability is a localized problem, however, can have a widespread impact. The voltage related stability situation in a power system is governed by the association among the transmitted active power, injected reactive power and receiving end voltage. This relationship holds an essential role in the voltage stability, and it can be represented graphically through an active power-voltage curve [9, 174]. At the knee point of the active power-voltage curve, the bus voltage rapidly drops with an increase in the load demand, and the power flow solution fails to converge indicating the voltage instability condition [9]. The active power-voltage analysis technique is used to assess the voltage stability of the considered distribution network in order to observe whether the wind farm has a contribution in the voltage stability enhancement.

Fig. 4.3 shows that the maximum loading margin of bus-6 is increased from 28.41 MW at base case to 29.46 MW with the presence of the wind farm. As presented in Fig. 4.4,

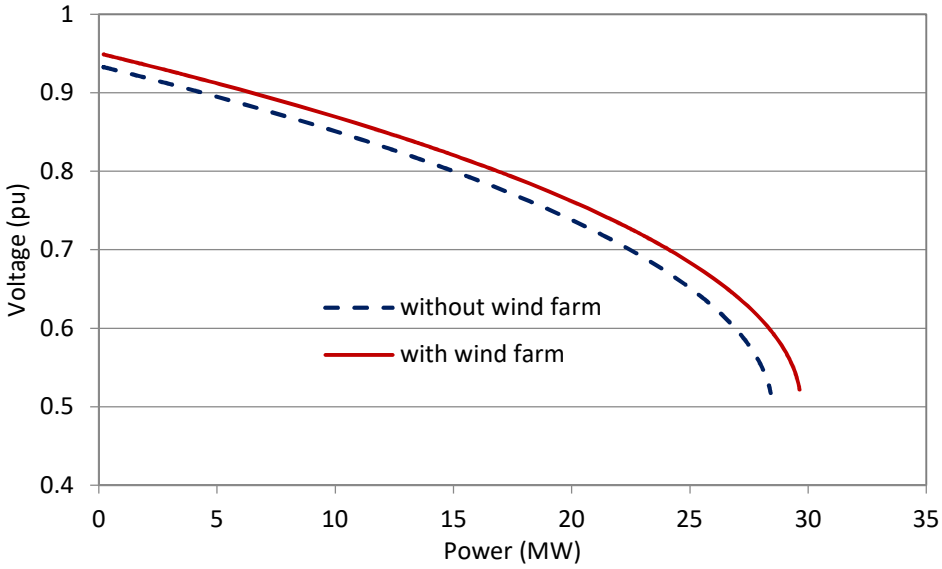

Figure 4.3 Active power-voltage curves of bus-6

a similar improvement in the loading margin are observed for bus-8. The bus-8 shows an increment from 103.41 MW to 112.42 MW from the base case to the wind power integrated case. This suggests that the wind farm can contribute enhancing the maximum loading margin of the distribution buses, which are far from the point of connection of the wind farm. This observation indicates that a wind farm connected to a weak distribution network not just only support voltages at the local buses but also assists to improve the overall voltage stability of the network.

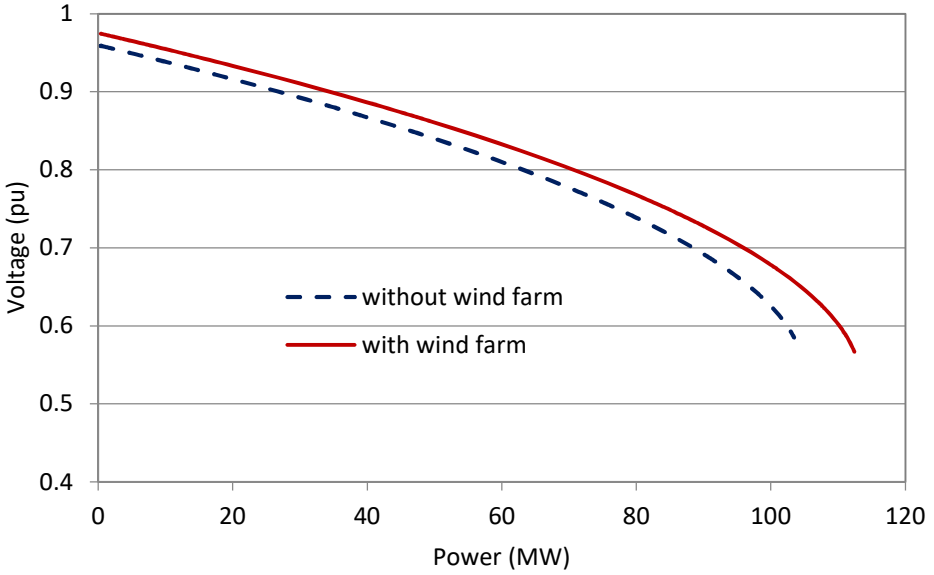

Figure 4.4 Active power-voltage curves for bus-8

In Fig. 4.5, the active power-voltage characteristic is plotted for bus-15 to observe the effect of the wind farm to a bus close to the point of interconnection. It is worth noting that the buses near the point of connection of the wind farm show a higher improvement in the maximum loading margins. As can be observed from Fig. 5.5, the bus-15 shows an improvement from 21.06 MW at the base case to 26.26 MW with the wind farm connected case. This analysis indicates that a wind farm can provide an increment in the voltage stability margin of a weak part of the distribution network.

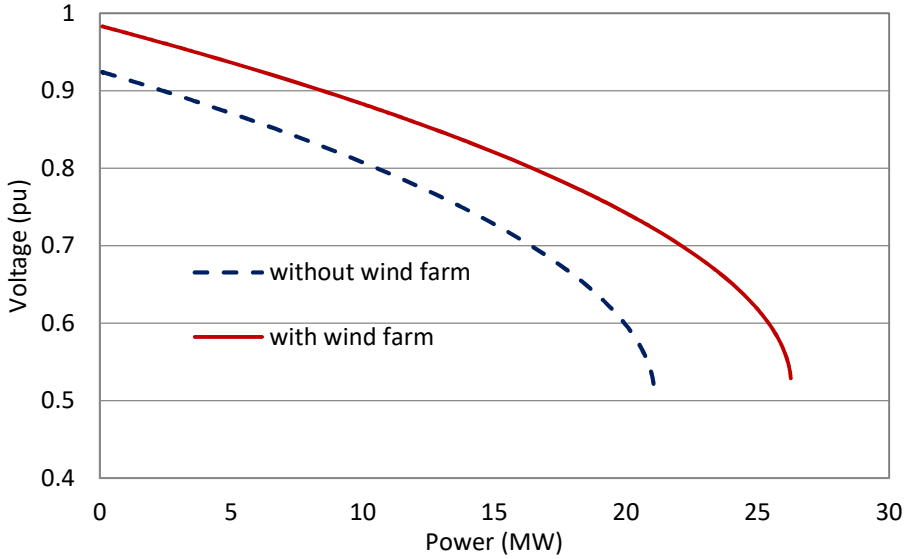

Figure 4.5 Active power - voltage curves for bus-15

From the active power-voltage analysis, it can be observed that the buses near the wind farm have a higher increment in the maximum loading margin as compared to the buses further away. Hence, these studies show that the DFIG-based wind farm can contribute to increasing the maximum loading margin of distribution system buses increasing the steady state voltage stability condition.

4.3 Transient voltage stability analysis

For the transient voltage stability analysis, time domain simulations are conducted following system disturbances, and the voltage and power flow oscillations are observed. The fault scenarios that are commonly occurring in a practical distribution network are created and analysed to observe the transient voltage responses of the wind

farm connected distribution system. The different case studies observed are

- 10-cycle, 3-phase faults at different buses.
- Sudden loss of motor load.
- Motor starting.

4.3.1 A three phase fault

A 3-phase 10-cycle zero impedance fault was initiated at 0.2 sec on bus-15, and the fault is cleared at 0.4 sec. The voltage and power transients are plotted for both the study scenarios, with and without the wind farm. The active power drawn from the external grid for the 3-phase fault at bus-15 is plotted in Fig. 4.6. During the fault, the wind integrated distribution system draws 55.94 MW compared to 53.35 MW in base case. This shows that a wind farm contributes to the fault scenarios, burdening less to the power grid the distribution network is connected to.

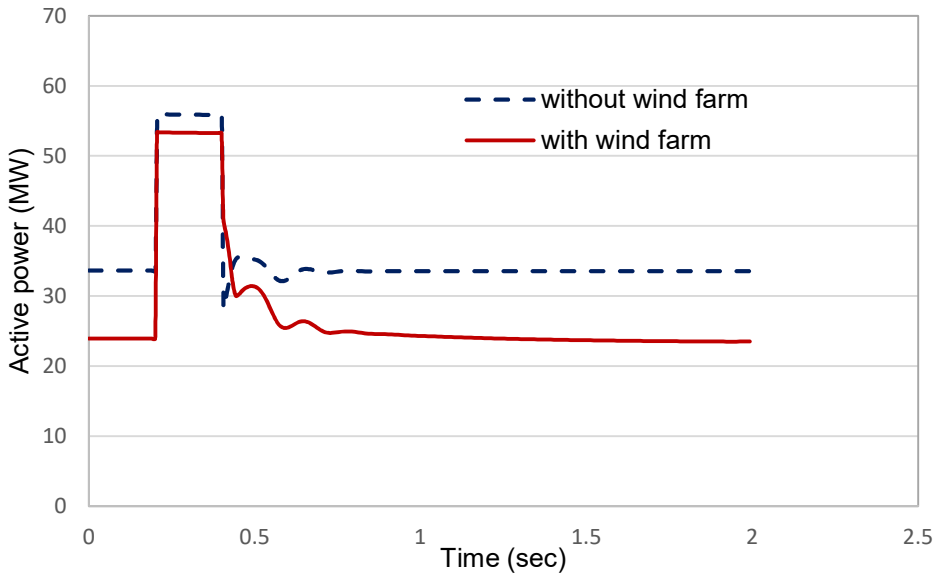

Figure 4.6 Active power from the external grid for 3-phase fault at bus-15

The transient response after the fault clearing is also better damped with the wind integration. This indicates that a local wind farm at a weak part of the network can contribute to damp power oscillations, following a transient fault condition in the distribution system.

Similarly, during the fault, the wind integrated distribution system draws 54.77 MVAr as compared to 57.32 MVAr in the base case as seen in Fig. 4.7. The reduction in the

reactive power requirement from the external grid shows that the DFIG can provide reactive support during the fault. It is further observed that the reactive power is better damped in the wind integrated cases.

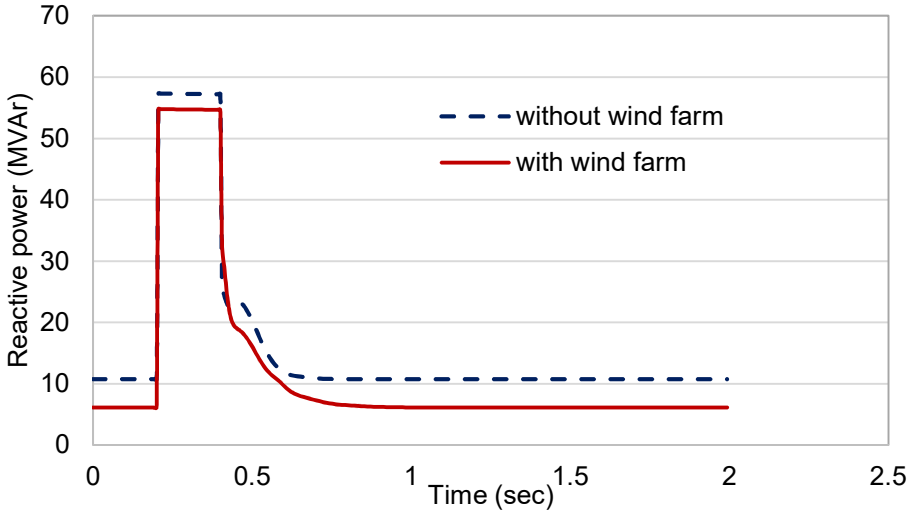

Figure 4.7 Reactive power from the external grid for 3-phase fault at bus-15

Fig. 4.8 shows the reactive power drawn by one of the motors for base case and with the wind farm. The reactive power demand of the motor following the 3-phase fault has shown an overshoot up to 5.25 MVAr in the base case scenario, whereas, with the wind farm, the reactive power demand is reduced and peaked at 4.76 MVAr. This observation shows that a local wind farm can support local loads in minimizing transient behaviour experienced during system disturbances.

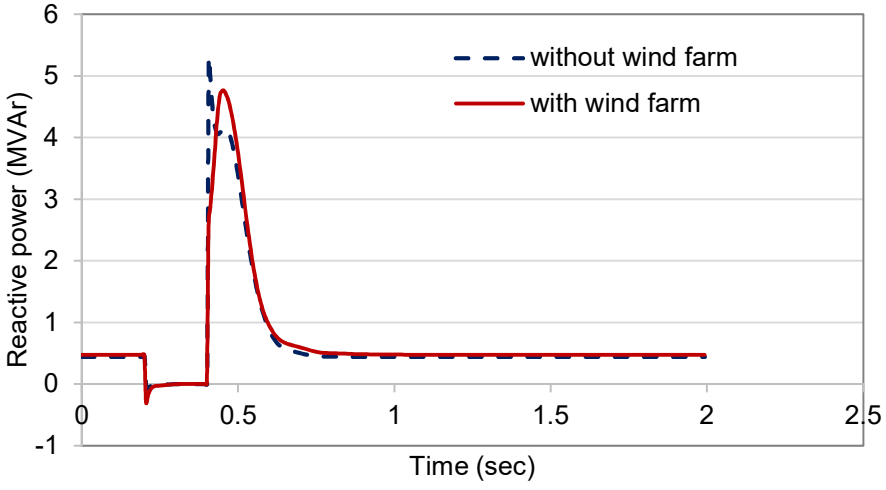

Figure 4.8 Reactive power drawn by a motor for 3-phase fault at bus-15

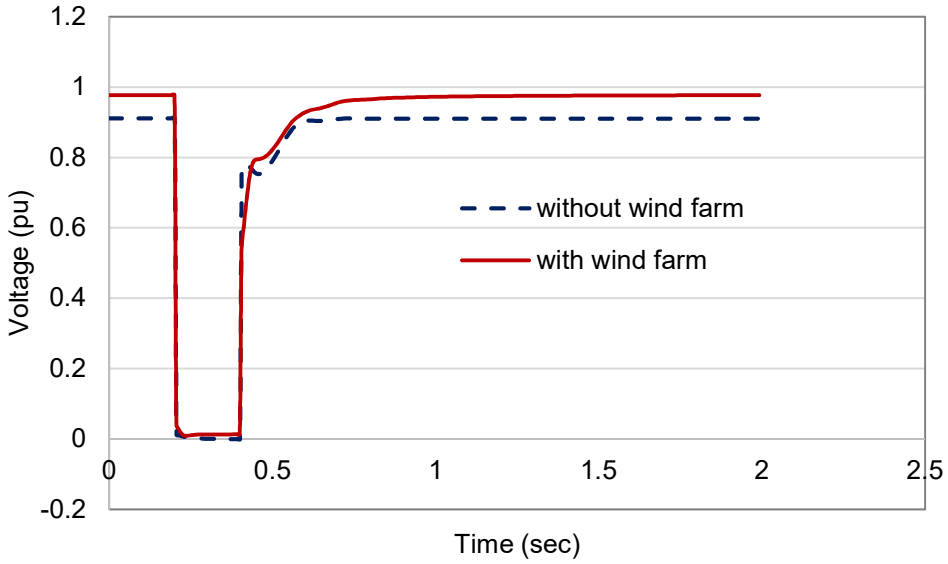

Figure 4.9 Voltage at bus-16 for 3-phase fault at bus-15

The voltage at bus-16 shows an improvement for 3-phase fault with the wind farm connected to the distribution system compared to the base case scenario as shown in Fig. 4.9. Similarly, the voltage transient following the fault clearance is better damped when the wind farm is connected.

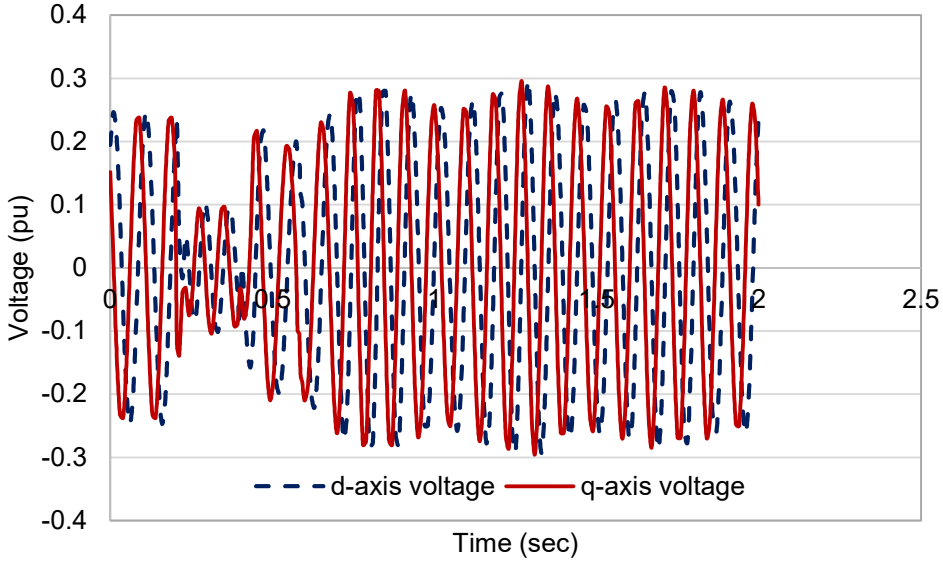

Figure 4.10 Rotor voltage variation of a DFIG unit for 3-phase fault at bus-15

The d-axis and q-axis rotor voltages of the DFIG-based wind farm for the 3-phase fault at bus-15 are plotted in Fig. 4.10. The plot shows the voltage recovery after the fault

is cleared as observed in the rotor voltage oscillations.

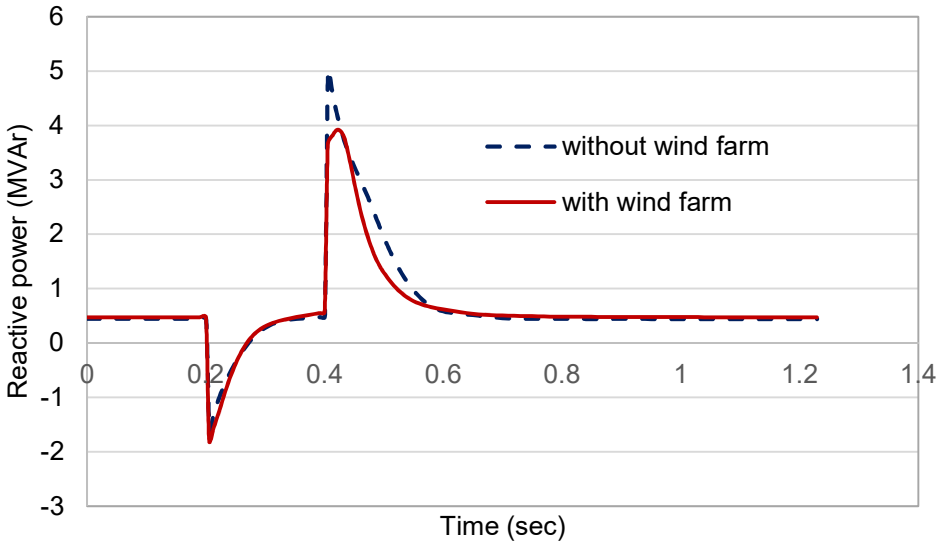

Figure 4.11 Reactive power drawn by a motor for a 3-phase fault at bus-5

Next, the voltage stability analysis is performed to study the response of the wind farm to a distant fault. For this study, the 3-phase fault is simulated at bus-5, and the reactive power demand of a motor and voltage at bus-16 are observed. Fig. 4.11 and Fig. 4.12 respectively show the reactive power drawn by the motor load and the voltage the bus. The first figure shows an overshoot at the base case scenario for the reactive power response. The response is observed to be improved when a similar fault scenario is simulated for the wind farm connected network.

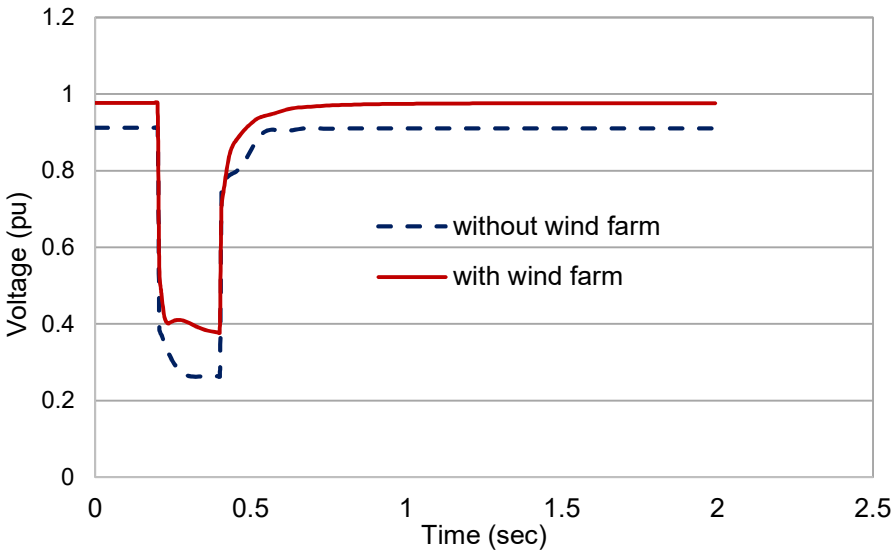

Figure 4.12 Voltage at bus-16 for 3-phase fault at bus-5

Similarly, the voltage dip magnitude at bus-16 is improved when the power system is simulated for the wind farm connected case compared to the base case as seen in the latter figure. Therefore, the DFIG-based wind farm integrated distribution system shows an improved voltage stability condition as compared to the base case. This observation indicates that the wind farm is capable of supporting a remote fault to provide a better voltage stability performance of the power system.

4.3.2 Sudden loss of motor load

Another study is conducted to observe the impact of the sudden loss of a motor load on the stability of the distribution system for both the base case and wind farm connected scenarios. Out of the three motor loads at bus-16, one motor unit is suddenly tripped at 0.2 sec, and the apparent power oscillation is observed for one of the remaining motor units. In Fig. 4.13, it is observed that the power oscillation with the DFIG-based wind farm integrated distribution system shows less oscillation as compared to the base case. This simulation shows that even in the case of a sudden loss of a large load, a wind farm can support the power network to better damp the power oscillations for the better transient voltage recovery experience.

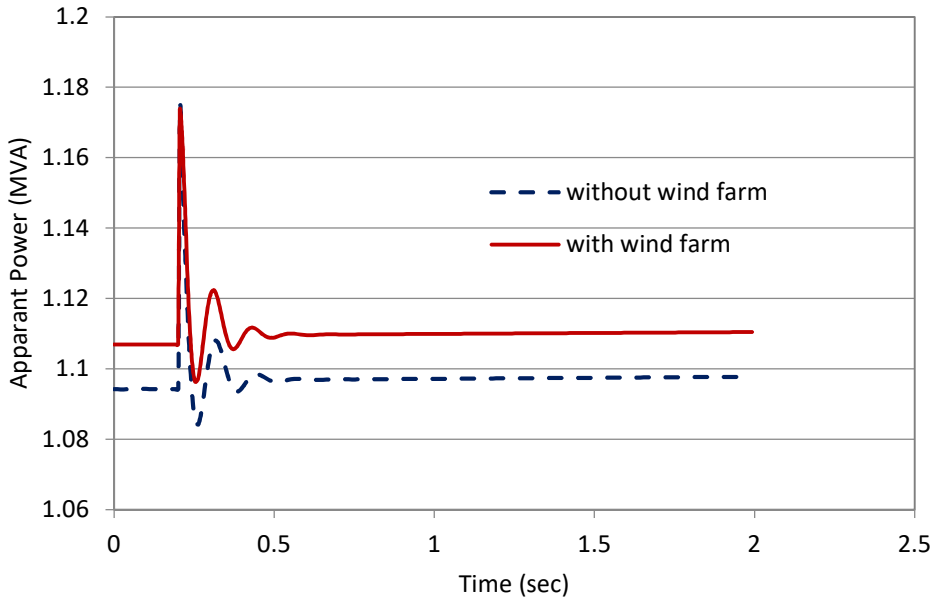

Figure 4.13 Power fluctuation at a motor for tripping of another motor

4.3.3 Motor starting

To observe the effect of motor starting on the voltage stability of the distribution system, one of the motors is started with the remaining two in operating condition. The condition with two motors running and starting the third motor is considered as the worst case for starting motor load. The other assumption is that only one motor is started at a time. With the wind integrated system, the voltage at bus-16 is dropped down only to 0.910 pu, whereas, at the base case the bus voltage drops to 0.855 pu as shown in Fig. 4.14 This study indicates that the wind farm could help to maintain the voltage of a weak voltage bus within an acceptable voltage range during starting of a large motor load. The recovery in the voltage dip condition is due to the ability of the wind farm to locally support reactive power demand during the motor starting.

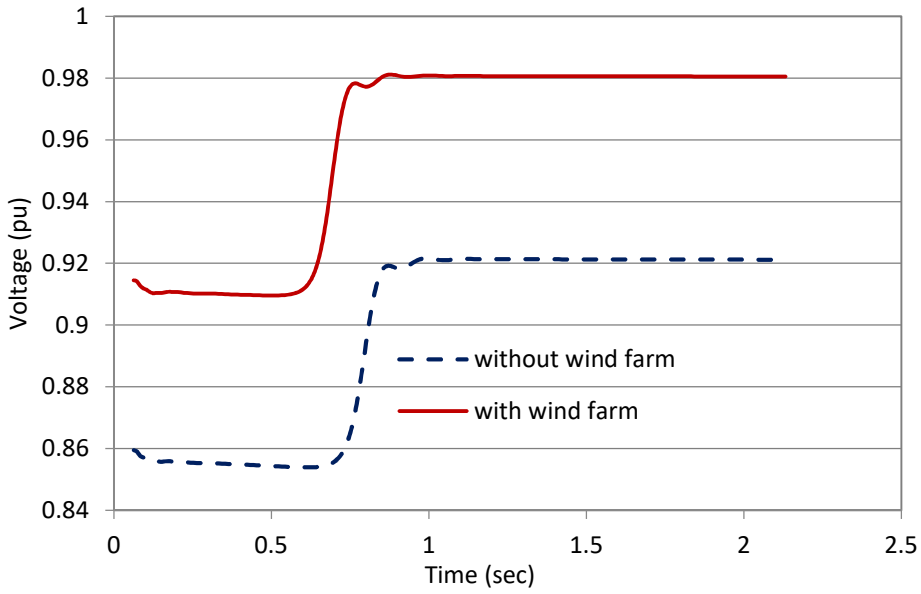

Figure 4.14 Voltage dip at the motor terminal during motor starting

Hence, from this observation, it can be concluded that a wind farm assists in the voltage recovery at the remote weak part of the distribution network, and assists to minimize the voltage dip problems, bringing the voltage fluctuation to an acceptable limit during a large motor starting.

4.4 Summary

The steady state and transient voltage stability of a distribution system with and without a remote DFIG-based wind farm is analysed and presented in this chapter. The wind farm is operated at power factor control mode of 0.95 lagging to support reactive power to the network when required.

The bus voltage analysis shows an improvement in the system bus voltages at all the buses of the distribution system with the wind farm integration. The buses in the proximity of the wind farm show higher improvement in the bus voltages as compared to that of the remote buses. The active power-voltage characteristics analysis shows that the maximum loading margin of all the buses is enhanced with the wind farm. Hence the study indicates that a remote DFIG-based wind farm in power factor-controlled mode, due to its ability to provide reactive power support can improve the steady state voltages of a weak distribution system.

Transient voltage stability analysis for different fault scenarios such as a 3-phase fault, sudden loss of motor load and motor starting show that the wind farm can contribute to improving the voltages and power oscillations during and following the studied transient conditions. In this study, it is observed that a remote DFIG-based wind farm can be connected to a weak distribution system without losing the voltage stability.

Chapter 5 Stability improvement by a static var compensator

In this chapter, an SVC based supplementary controller is designed and implemented in a DFIG-based wind farm connected power system to enable additional damping of power system oscillations. Firstly, a weak bus is identified from the voltage stability perspective at which SVC is installed. Finally, a suitable signal is selected for the controller input, which provides enhanced damping of the low frequency oscillations observed in the power system.

5.1 Test system

Due to the unavailability of a real study case, a modified institute of electrical and electronics engineers (IEEE) 14-bus test system [151] as given in Fig. 5.1 is used for this study. Table 5.1-5.3 present the modified data of the test system. The test power system has 66, 18 and 13.8 kV voltage levels. The total system generation is 389 MW and the load is 362.60 MW. The 66 kV network has total load of 239.82 MW, and 13.8 kV network has of 122.78 MW. A DFIG-based wind farm is connected to the low voltage network at bus-12, and an analysis is conducted for 20 and 60 MW penetrations of the wind power. The 20 MW wind penetration accounts for about 16% penetration of the total load of the low voltage network, and is considered as the optimal penetration as many power networks around the world have already seen or about to have around that level of wind penetration. The 60 MW, wind power penetration, accounts for about 50% penetration in the low voltage network and is considered as the high wind penetration for this study. As discussed below, the bus-14 is identified as a voltage weak bus. Therefore, SVC is connected to the bus so as to provide voltage support to the power system. A supplementary controller is designed

and implemented with the SVC to provide further damping of the low frequency power oscillations.

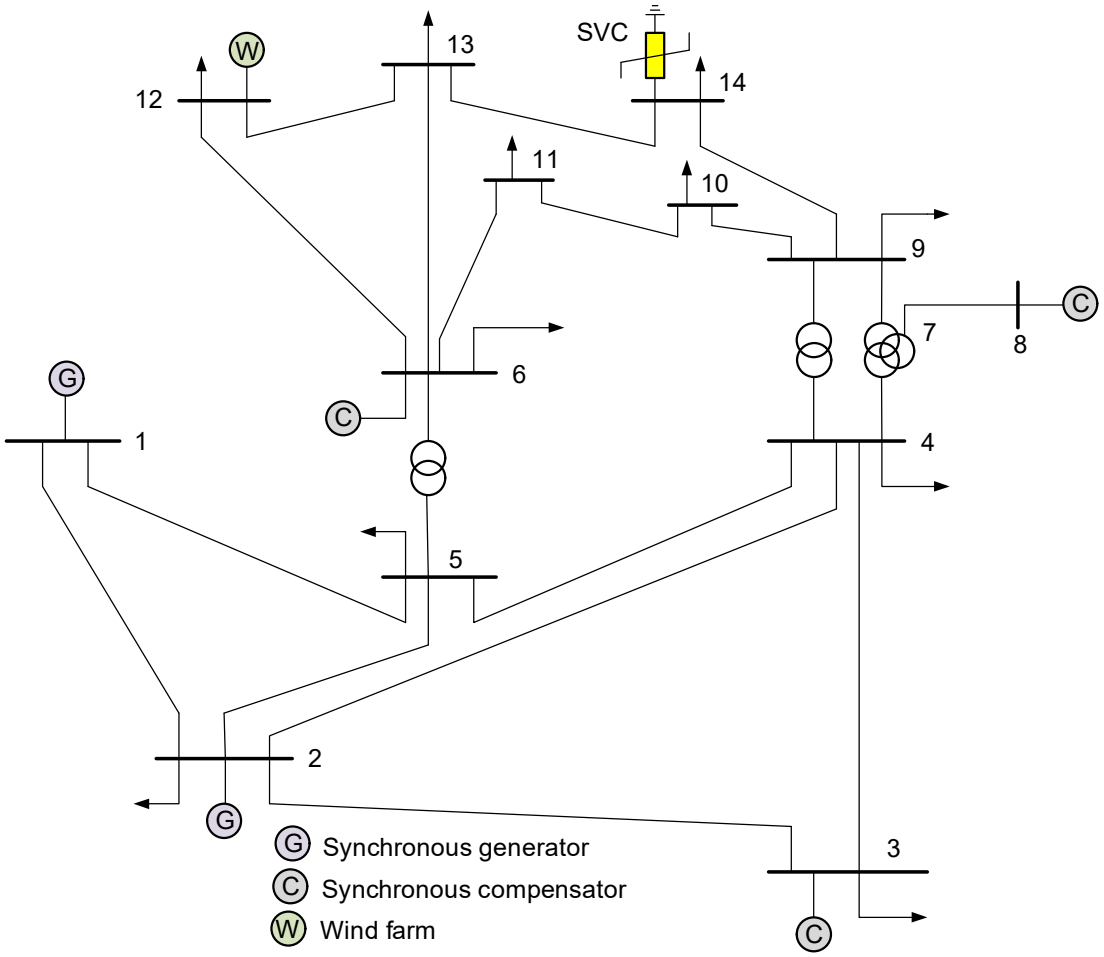

Figure 5.1 Modified IEEE 14-bus system

Table 5.1 Parameters of the wind farm at bus-12

Power rating, S_n, MVA	20	60
Stator resistance, r_s, Ω	0.095	0.031
Stator reactance, x_s, Ω	0.952	0.317
Rotor resistance, r_R, Ω	0.095	0.031
Rotor reactance, x_R, Ω	0.761	0.253
Magnetizing reactance, x_m, Ω	28.566	9.522

Table 5.2 Parameters of the SVC device at bus-14

Power rating, S_n, MVA	10
Regulator gain, K_r	10
Time constant, T_g, s	0.02

5.2 Identification of weak bus

The research work identifies 14 modes of voltage instability as shown in Fig. 5.2. Mode 7 is observed to be the weakest mode with the magnitude of 0.794 at 20 MW wind power penetration. Bus participation to the weakest mode is found, and presented in Fig. 5.3. Bus-14 exhibits the highest participation factor of 0.153 to the mode.

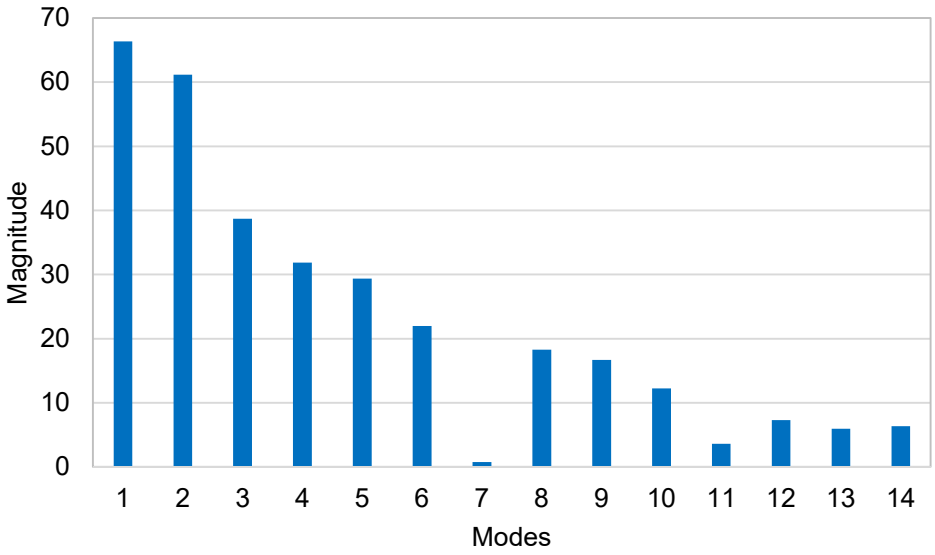

Figure 5.2 Modes of voltage instability

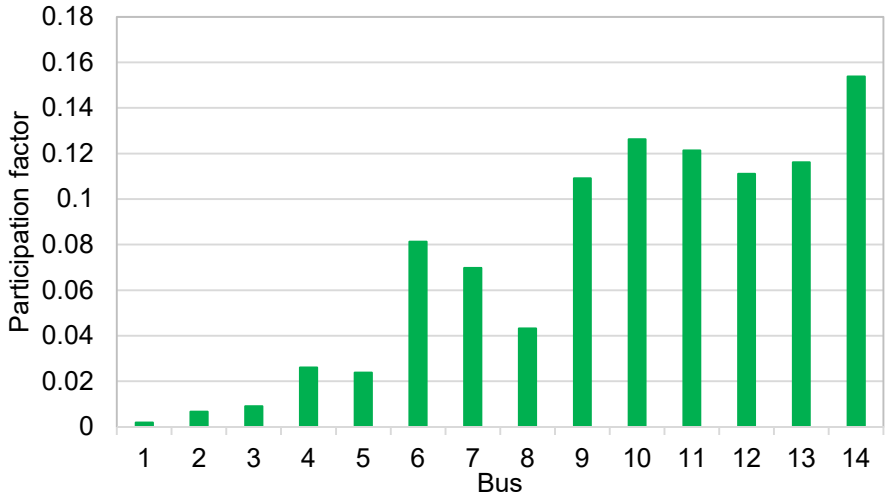

Figure 5.3 Bus participation factor of the weakest mode

This study indicates that the region of bus-9 to bus-14 is the weak part of the test power

system from the voltage stability perspective. Within the region, bus-14 is identified as the weakest voltage stability point. Therefore, the bus is selected as the best location for SVC placement.

Table 5.3 The weakest mode present in the power system

Wind farm location	Wind farm type	Wind power penetration	Magnitude of the weakest mode	Bus with the highest participation
No wind farm		-	0.749	bus-14
bus-12	DFIG	20 MW	0.794	bus-14
		60 MW	0.790	bus-14

Table 5.3 shows the magnitude of the weakest mode in the power system network. It is observed that the magnitude is increased with the installation of the wind farm at bus-12 at both the penetration levels of 20 and 60 MW. The bus-14 is perceived to have the highest participation to the weakest mode, so selected for the SVC installation.

5.3 Small signal stability without SVC

To understand the impact of different penetration levels of wind power on the small signal stability of a power system, it is essential to analyse the behaviour of the oscillation damping with those penetration levels. A comparative analysis of the oscillatory modes and their damping is conducted for 20 and 60 MW wind power penetrations at bus-12 by a DFIG-based wind farm.

From this study, 12 low frequency oscillatory modes are observed which are presented in Table 5.4 and Table 5.5. The mode with the lowest damping ratio is the critical mode of the system [175]. The oscillatory mode (5, 6) has very poor damping of damping ratio 2.07% at 20 MW wind power penetration, and 4.08% at 60 MW wind power penetration respectively. So, this mode is considered as the critical mode, whereas, the rest of the modes show significant oscillation damping with all of them having the damping ratio of about and over 30%. A comparative analysis of Table 5.4 and Table 5.5 shows that the damping ratios of some of the oscillatory modes are increased whereas the remaining show decrement of their damping performance with the increase in wind power penetration. However, most importantly the damping ratio

of the critical mode is increased at the increased wind penetration. The oscillatory frequencies are observed about and below 2 Hz for all the modes existing in the power system at both wind power penetration levels.

Table 5.4 Low frequency oscillatory modes at 20 MW wind penetration

Modes	Real part (1/s)	Imaginary part (rad/s)	Damping ratio (%)	Frequency (Hz)
1,2	–43.889	8.073	98.35	1.28
3,4	–4.938	12.025	37.99	1.91
5,6	–0.190	9.202	2.07	1.46
7,8	–3.671	10.872	31.99	1.73
9,10	–3.291	9.807	31.81	1.56
11,12	–2.661	8.657	29.39	1.38
13,14	–10.327	0.193	99.98	0.03
15,16	–0.718	1.426	44.96	0.23
17,18	–1.149	1.333	65.28	0.21
19,20	–1.384	0.730	88.43	0.12
21,22	–0.591	0.756	61.61	0.12
23,24	–0.640	0.359	87.23	0.06

The participation factor analysis evaluates the contribution of power system components to a particular mode of oscillation. The critical mode has the participation of various power system components with significant participation of the synchronous generator at bus-1. This signifies that the synchronous generator is crucial to the critical mode of oscillation observed in the studied power system.

5.4. Small signal stability with SVC

An SVC is connected at bus-14, which is identified as the weakest bus from the voltage stability point of view. Small signal stability is analysed with the shunt compensation device for different wind power penetration from the DFIG-based wind farm at bus-12. The damping ratio of the critical mode is increased to 4.09% at 20 MW penetration, and 5.24% at 60 MW penetration. Hence, the shunt compensation aids to improve the small signal stability of the power system with the wind farm. Another observation

shows that the oscillatory frequency for the mode remains almost unaffected with the compensation device.

Table 5.5 Low frequency oscillatory modes at 60 MW wind penetration

Modes	Real part (1/s)	Imaginary part (rad/s)	Damping ratio (%)	Frequency (Hz)
1,2	–43.920	8.117	98.33	1.29
3,4	–4.476	12.634	33.39	2.01
5,6	–0.377	9.233	4.08	1.47
7,8	–3.593	10.872	31.38	1.73
9,10	–3.309	9.579	32.66	1.52
11,12	–2.574	8.700	28.38	1.38
13,14	–10.402	0.148	99.99	0.02
15,16	–0.926	1.156	62.52	0.18
17,18	–1.148	1.332	65.28	0.21
19,20	–1.405	0.720	88.98	0.11
21,22	–0.591	0.752	61.81	0.12
23,24	–0.628	0.356	86.97	0.06

5.5. Small signal stability with a supplementary controller

In the end, a supplementary controller is designed to observe its effectiveness in damping oscillation of the critical mode. To ensure that the best responsive input signal is selected, multiple signal selection techniques like residue method, Hankel singular value, and right-hand plane zeros are used. The choice of the input signal is not limited to the locally available signals but extended to a wide range of global signals. The line current, active power, and reactive power signals are studied to pick the final input signal for the controller device.

5.5.1 Residue analysis method

Residue analysis method is carried out for different signal groups, line current, active power and reactive power for all the lines in the test power system. Candidate signals

are selected from each signal groups using relative residue ratio (RRR_i) [176]. For a particular signal group,

$$RRR_i = |R_i|/(\sum_{i=1}^{N} |\mathrm{R}_i|) \tag{5.1}$$

where R_i is the residue of the signal in line i and N is the total number of lines in the power system.

Firstly, the local current flowing through the line connected to the SVC bus (bus-14) are analysed for the possible input signal. It is observed that the current flowing through 'line 9-14' (I_8) has higher residue value for both the studied scenarios as compared to the current flowing through 'line 14-13' (I_9). Similarly, when global signals are analysed, the current through line 1-2 is ranked to have the highest residue magnitude of all the signals in the network, therefore, is selected for further assessment. The RRR_i value of the local current signals and global candidate current signals are presented in Table 5.6. Even though, all the line currents in the power system are considered for the residue analysis method, only the local signals and top three global signals having the highest residue values are presented in the table for comparison. The RRR_i values in the table indicate that the global signals have higher residue values as compared to the local signals, making them suitable candidate for input signal of the supplementary controller.

Table 5.6 Ranking of line currents based on RRR_i values

Signal type	Line (bus-*m* - bus-*k*)	Line current (I)	The wind farm at bus-12 with penetration of			
			20 MW		60 MW	
			RRR_i	Signal Rank	RRR_i	Signal rank
Local	9-14	I_8	0.034	1	0.023	1
Local	14-13	I_9	0.018	2	0.008	2
Global	1-2	I_{11}	0.307	1	0.317	1
Global	3-2	I_{12}	0.114	2	0.113	2
Global	1-5	I_{14}	0.110	3	0.113	3

A similar assessment is conducted for signal groups active power (P_i) and reactive power (Q_i) as shown in Table 5.7 and Table 5.8 respectively. This assessment also

gives similar observation as that of the current signals. Active power flowing through the line 1-2 is ranked to have the highest magnitude of RRR_i, therefore, is selected for further assessment.

Table 5.7 Ranking of active power based on RRR_i values

Signal type	Line (bus-*m* - bus-*k*)	Active power (P)	The wind farm at bus-12 with a penetration of			
			20 MW		60 MW	
			RRR_i	ranking	RRR_i	ranking
Local	9-14	P_8	0.002	2	0.001	2
Local	14-13	P_9	0.003	1	0.002	1
Global	1-2	P_{11}	0.345	1	0.345	1
Global	3-2	P_{12}	0.106	3	0.104	3
Global	1-5	P_{14}	0.116	2	0.116	2

Similarly, the reactive power signal flowing through line 1-2 shows the highest magnitude for RRR_i value, therefore, is selected for the possible feedback signal for further assessment.

Table 5.8 Ranking of reactive power based on RRR_i values

Signal type	Line (bus-*m* - bus-*k*)	Reactive power (Q)	The wind farm at bus-12 with a penetration of			
			20 MW		60 MW	
			RRR_i	ranking	RRR_i	ranking
Local	9-14	Q_8	0.069	1	0.052	1
Local	14-13	Q_9	0.047	2	0.030	2
Global	1-2	Q_{11}	0.279	1	0.303	1
Global	3-2	Q_{12}	0.082	3	0.072	3
Global	1-5	Q_{14}	0.105	2	0.098	2

With the residue method, three candidate signals having the highest magnitude in their respective group are selected for further evaluation. The local signals, due to their low relative residue values, are not considered for further assessment as candidate input signals. The candidate signals presented in this section shows that the best local and global signals are independent of the wind penetration level.

5.5.2 Hankel singular values analysis

Hankel singular value analysis is performed for the three candidate signals filtered through the residue method. Table 5.9 shows the Hankel singular values of the candidate signals, the values (the first 10 states are presented for the comparison) are ordered in their descending order. The signal P_{11} has higher Hankel singular values compared to the other candidates. These signals are further assessed with right hand plane zero in the next section.

Table 5.9 Hankel singular values

Values	Candidate signals		
	I_{11}	P_{11}	Q_{11}
1	3.037	3.234	1.574
2	3.032	3.158	1.455
3	0.304	0.358	0.349
4	0.234	0.277	0.329
5	0.090	0.053	0.097
6	0.036	0.035	0.075
7	0.018	0.017	0.047
8	0.015	0.016	0.023
9	0.005	0.007	0.003
10	0.003	0.003	0.002

5.5.3 Right hand plane zero method

The candidate signal in each group is further assessed using right hand plane zero method. The right hand plane zeros are calculated for each candidate signals as shown in the Table 5.10. The signal P_{11} doesn't produce a right hand plane zero, therefore, is

selected for the feedback signal. As $I_{11,}$ creates a right hand zero, hence, is eliminated, and the signal Q_{11} is the next best signal.

Table 5.10 Right hand plane zeros of the candidate signals

Signal group	Candidate signals	RHP-zeros
I	I_{11}	8.11+-j8.23
P	P_{11}	none
Q	Q_{11}	none

5.5.4 Supplementary controller design

With the selection of the active power P_{11} as the input signal, the transfer function is analysed for the controller design. Table 5.11 presents the controller parameters to provide the desired damping of the critical mode for 20 and 60 MW wind power penetration cases.

The washout time constant (T_ω) is assumed as 10 sec [9]. It is observed that at 20 MW wind penetration, a controller gain of value 0.777 is required to provide damping ratio of 15% to the critical mode, whereas, at 60 MW wind penetration a gain value of 0.483 is sufficient to provide the desired damping. So, the controller parameters of 20 MW wind penetration case presented in the table is selected as the final controller parameters to provide the desired damping ratio of 15% at both the penetration levels. Hence, putting the values of the controller parameters, (3 28) becomes

$$POD(s) = 0.777\left(\frac{10s}{10s+1}\right)\left(\frac{0.1313s+1}{0.0926s+1}\right)^2 \tag{5.2}$$

Table 5.11 Controller parameters

Wind penetration (MW)	Gain (K_ω)	Time constant (sec)	
		First time constant, T_1	Second time constant, T_2
20	0.777	0.1313	0.0926
60	0.483	0.1319	0.0920

Thus, it is observed that a supplementary controller can be designed to damp critical mode for different penetration of wind farms by varying the gain of the controller. The damping ratio of the critical mode is presented in Fig. 5.4, for all the studied scenarios.

It is observed that an SVC can provide enhanced damping of the critical mode. However, a supplementary controller can be designed to provide significant enhancement in the damping of the mode.

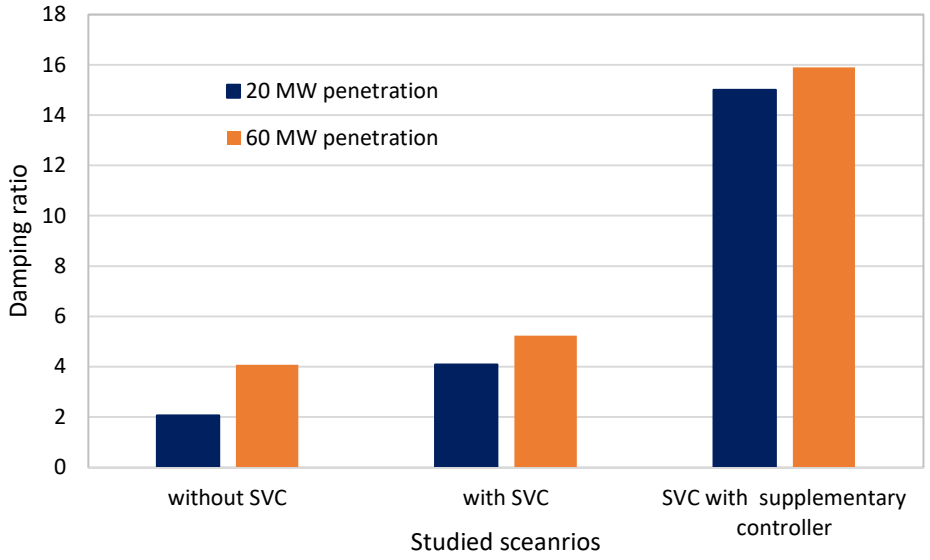

Figure 5.4 Damping ratio of the critical eigenvalue

5.6 Sensitivity analysis

In this study, the percentage change in wind power penetration, in total generation, and in total load of the power system are chosen as sensitivity parameters. As the real part of an eigenvalue determines the stability of the associated mode, the sensitivity of the real part with respect to the change in sensitivity parameters is observed. Hence, the sensitivity of the critical mode with respect to the sensitivity parameters are examined in this section. The sensitivities are evaluated for 1% increase and decrease in the sensitivity parameters. The eigenvalue sensitivity can be calculated numerically by performing two eigenvalue calculations with the system parameter, and at slightly perturbed values [176]. The positive real part sensitivity indicates that with the change in the sensitivity parameter, the critical mode will move further left in the left half plane making the system more stable and vice-versa.

In this work, the real part sensitivity of eigenvalue is calculated for 20 MW wind penetration from DFIG-based wind farm by performing two eigenvalue calculations with the assumed sensitivity parameter at perturbed values of $K \pm \Delta K$. With 1% increase in wind penetration, the critical mode (–0.19022 ± j9.2029) is moved to (–

0.21041 ± j9.2056), which gives a positive real part sensitivity of 0.02019 as shown in Table 5.12. Whereas with 1% decrease in wind penetration the mode moves to (–0.16967±j9.2003) giving a negative real part sensitivity of 0.02055. This indicates that the critical mode is sensitive to the change in wind penetration level. Similarly, the sensitivity analysis is performed for a change in system load. For the study all, the loads in the power system are increased by 1%. With the increase in the total system load, the mode shows a negative sensitivity of 0.11349 which means the real part moves 59.66% towards the imaginary axis making the power system unstable. However, for the 1% decrease in the total system load, the critical mode shows a positive real part sensitivity of 0.22933 which is 120.56% further shift to the left in the left half plane. Finally, the sensitivity is observed for total system generation. The increase in the total generation gives a positive real part sensitivity, and a decrease in the total generation gives a negative real part sensitivity. The study shows that the mode is more sensitive to the change in the system loads as compared to the other cases studied.

Table 5.12 Real part sensitivity for 1% change in sensitivity parameter

Sensitivity parameter	Increase in the sensitivity parameter		Decrease in the sensitivity parameter	
	Shift in real part ($\Delta\alpha$)	Sensitivity (%)	Shift in real part ($\Delta\alpha$)	Sensitivity (%)
Wind penetration	0.0201	10.61	–0.0205	10.8
System load	–0.1134	59.66	0.2293	120.56
System generation	0.0377	19.83	–0.0421	22.14

5.7 Time domain analysis

As observed in the earlier section, the best input signal is independent of the wind penetration level. Hence, the time domain simulation is used to observe the effectiveness of the designed supplementary controller. A disturbance was created by tripping of line 6-13 at 0.1 sec till 0.3 sec. The response of the voltage of bus-2 was observed in Fig. 5.5 for the 20 MW power penetration case. It is noted that the supplemenary controller provides an increased damping to the voltage oscillations as

compared to the system without it. Hence, it can be concluded that the supplementary controller, added to the shunt compensation, can provide effective damping control.

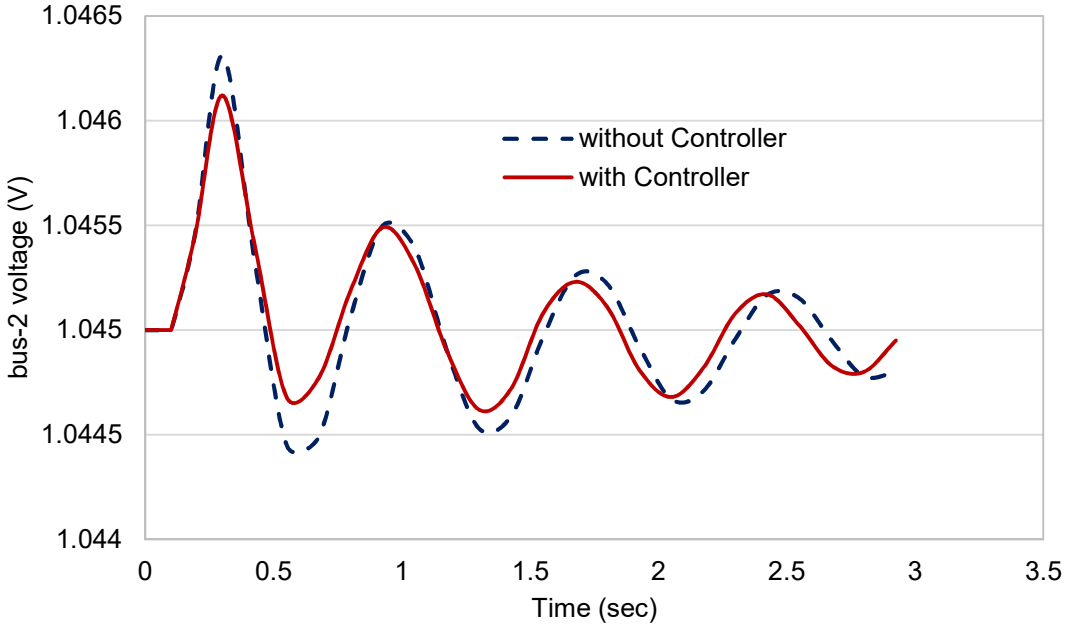

Figure 5.5 Variation in bus-2 voltage for 20 MW wind penetration

The effect of the input signal to the supplementary controller is presented in Fig. 5.6. For the same fault, as described above, the swinging of delta of generator 2 is observed for the best signal selected (P_{11}) and the next candidate signal (Q_{11}). It is observed that the signal (P_{11}) provides better damping, which indicates the supplementary controller with a suitable input signal can provide effective damping to the power oscillations.

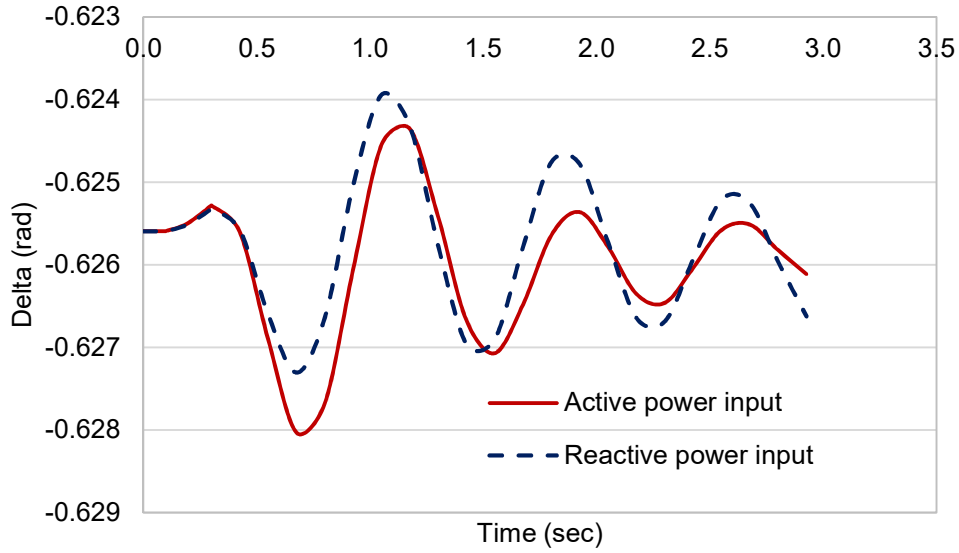

Figure 5.6 Swing curve of the generator-2 for the change in controller input

5.8 Summary

This chapter presents an approach to enhance the small signal stability of a power system with the penetration of wind power from a DFIG-based wind farm. A critical oscillatory mode is identified, and a supplementary controller is designed enhancing damping of the mode. A methodology has been proposed to select an appropriate input signal for the controller to enhance the damping performance. A sensitivity analysis is performed to observe the sensitivity of the mode to the selected sensitivity parameters such as wind penetration, system load, and generation change.

A shunt compensation is installed at the most suitable location selected for the voltage support. Modal analysis and participation factor analysis are used for the selection of the location. The damping capability of the shunt device is evaluated using eigenvalue analysis. The shunt device is found to be effective in enhancing damping of the oscillatory mode. Finally, a supplementary damping controller is added to the shunt device which significantly increases the damping of the mode by shifting the eigenvalues to the desired location. An appropriate input signal for the supplementary controller is selected using multiple signal selection techniques. The local and global signals are examined to achieve an increased damping capability of the controller. The values of the time constants and gain of the controller are calculated to achieve a damping ratio of 15% for both penetration levels. Hence, in a power system with a wind farm, a supplementary controller can be designed to significantly enhance the damping of the critical mode, thereby, improving the overall stability of the power system.

Chapter 6 Stability improvement by a high voltage dc link

In this chapter, an eigenvalue analysis method is implemented to identify the oscillatory modes existing in the power system, and the contribution of different state variables to those modes. A wind farm connected power system is analysed for the stability of the study cases, the power system with and without an HVDC link. The penetration level of the wind power from the wind farm is varied from 5 to 20 % in order to observe the influence of the variation to the power system stability. Additionally, the stability impact at the different wind power penetration levels is observed and analysed.

6.1 Test system

This study is carried out on a modified 14-bus IEEE system as in Fig. 6.1 [177]. The test power system has 66 kV, 18 kV, and 13.8 kV voltage levels. A bus-15 is added and connected to bus-5 by a line 5-15. A wind farm is connected to bus-15, and an HVDC link is implemented between bus-5 and bus-4. A small signal stability analysis is performed for 5, 10, 15 and 20 % penetration levels of the wind power for the cases of with and without the HVDC link in the power system. The impact of the variation in the degree of penetration levels is compared and analysed for an understanding of the impact of the wind power penetration on the small signal stability. The technical data of the test system is presented in the Table 6.1- 6.3, where Table 6.1 presents the parameters of the line from bus-5 to bus-15, the Table 6.2 covers the parameters of the wind farm at bus-5, and Table 6.3 presents the parameters of the HVDC line implemented for the stability study.

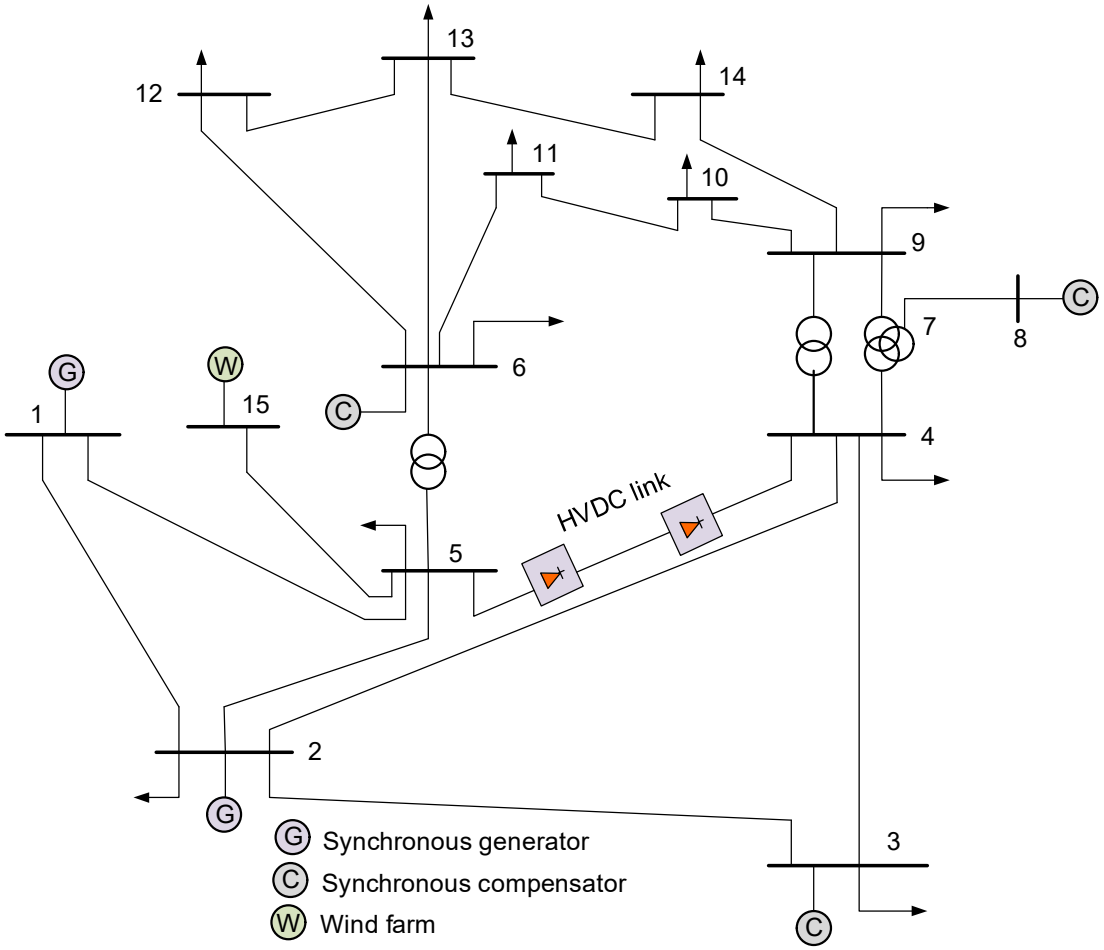

Figure 6.1 Modified IEEE 14-bus system

Table 6.1 Parameters of the line from bus-5 to bus-15

Line	Resistance, Ω	Reactance, Ω	Susceptance, F
bus-5 - bus-15	0.05403	0.22304	0.0492

Table 6.2 Parameters of the wind farm at bus-5

Power rating, S_n, MVA	100
Stator resistance, r_s, Ω	0.019
Stator reactance, x_s, Ω	0.190
Rotor resistance, r_R, Ω	0.019
Rotor reactance, x_R, Ω	0.121
Magnetizing reactance, x_m, Ω	5.712

Table 6.3 Parameters of HVDC line

Power Rating, S_n, MVA	100
DC voltage rating V_{ndc}, kV	300
Transformer reactance (rectifier), X_{tR}, Ω	6.403
Transformer reactance (inverter), X_{tI}, Ω	5.984
Integral gain, K_I	20
Proportional gain, K_P	25
Resistance of DC connection, R_{dc}, Ω	0.0625
Inductance of DC connection, L_{dc}, H	0.2

6.2 Small signal stability analysis without HVDC

The studied power system is linearized around a stable operating point, which gives a close approximation of the nonlinear system. The linearized system is presented using differential and algebraic equations. The dynamic behaviours are determined by the stable operating point and the parameters of the dynamic components. A wind farm can be modelled as a single equivalent machine to reduce computational burden. This assumption is valid as the purpose of this study is to observe the effect of wind power penetration on the power system network rather within the wind farm [22].

For the understanding of the impact of different penetration levels of the DFIG-based wind farm on the power system stability, it is essential to understand the change in the behaviour of the oscillation damping with a change in penetration levels. A comparative study is conducted for 5, 10, 15 and 20 % penetration levels of the wind power from a DFIG-based wind farm. Voltage gain is set at 10 and 20 to study the impact of the variation of the voltage gain of the wind farm on the small signal stability. A wind farm is connected to bus-15, and the small signal stability is carried out for the different penetration levels of wind power. From the analysis, 11 pairs of complex low frequency oscillatory modes are observed.

Fig. 6.2 shows the complex eigenvalues existing in the power system at the different penetration levels of the DFIG-based wind farm. At the 5 and 10 % penetration levels, a pair of eigenvalues is observed in the right half of the complex plane representing an unstable power system operation. According to [175], the excitation system of a synchronous machine reduces the damping ratio of the critical mode by pushing the

mode towards the imaginary axis. At 15 and 20 % penetration levels, all the eigenvalues are shifted to the left half of the complex plane making the power system stable. This study shows that some of the oscillatory modes on the left half of the complex plane are adversely affected by the increasing wind power penetration. However, the most of the oscillatory modes are shifted further left, thereby, enhancing the power system stability.

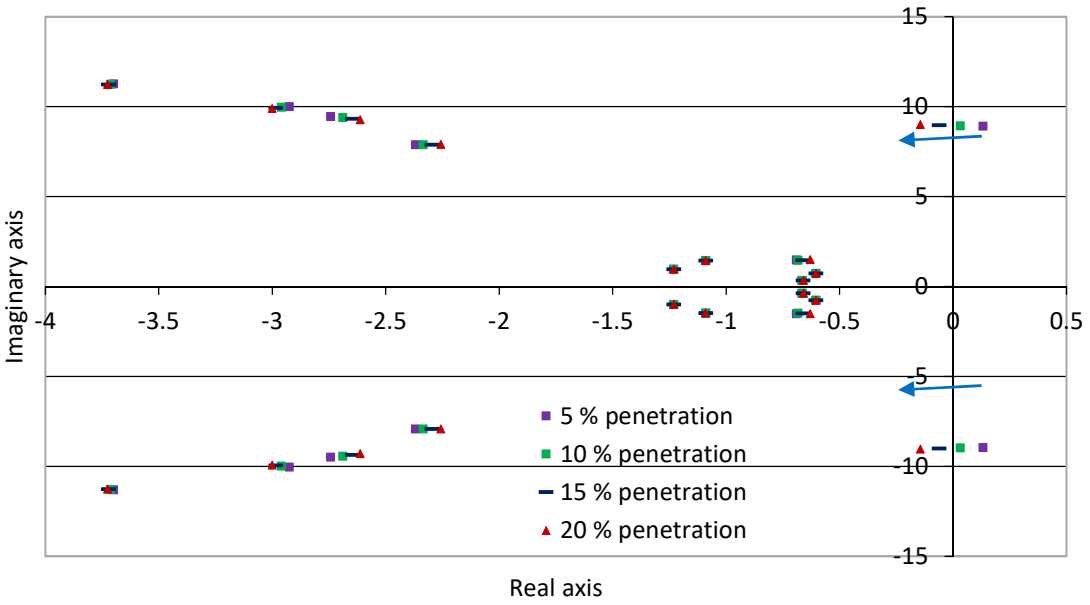

Figure 6.2 Movement of complex eigenvalues for the variation in wind penetration in the power system without HVDC link

Table 6.4 shows the critical mode existing in the power system for different penetration levels of the DFIG-based wind power system without an HVDC link for voltage gain values of 10 and 20. At the voltage gain values of 10, the power system exhibits negative damping of the critical mode for up to 10% of the wind power penetration, whereas, when the voltage gain was set at 20, the critical mode exhibits positive damping, beyond 5% of the wind penetration. This shows that a wind farm operated at a higher voltage gain can contribute higher to the small signal stability enhancement. Another observation shows that the damping ratio is improved with an increase in the wind power penetration. This exhibits that a higher wind power penetration contributes to an improvement in the damping of the critical oscillatory mode.

6.3 Small signal analysis with HVDC

An HVDC link is implemented between bus-4 and bus-5 by removing the existing ac line, and a wind farm is connected at bus-15. A comparative study of the small signal stability of the power system is conducted for 5, 10, 15 and 20 % penetration of the DFIG-based wind farm for the voltage gain values of 10 and 20. The study shows 11 pairs of complex low frequency oscillatory modes existing in the power system.

Table 6.4 Critical eigenvalue in the power system without HVDC link

Wind penetration			Real part (1/s)	Imaginary part (rad/s)	Damping ratio (%)	Frequency (Hz)
MW	Percent	Voltage gain				
18	5	10	0.132	8.931	–1.47	1.421
		20	0.039	8.947	–0.43	1.424
36	10	10	0.031	8.955	–0.34	1.425
		20	–0.063	8.969	0.70	1.428
54	15	10	–0.062	8.985	0.69	1.430
		20	–0.158	8.997	1.76	1.432
72	20	10	–0.146	9.022	1.61	1.436
		20	–0.247	9.031	2.73	1.437

Fig. 6.3 shows the complex eigenvalues existing in the power system at the different penetration levels of the DFIG-based wind farm. At the low penetration level of 5%, a pair of complex low frequency oscillatory mode is observed in the right half of the complex plane. However, when the penetration level reaches 10, 15 and 20 %, all the complex eigenvalues are shifted to the stable region of the eigenvalue plot. Some of the oscillatory modes are observed to be unaffected with the change in the penetration levels, whereas, the remaining of the oscillatory modes are adversely affected showing a slight reduction in their damping. This shows that at the higher wind penetration level, the power system shows better stability.

Table 6.5 shows the low frequency oscillatory mode existing in the power system with an HVDC link for different penetration levels of DFIG-based wind power for the voltage gain values of 10 and 20. At the voltage gain value of 10 and the wind power penetration of 5%, an oscillatory mode shows to have a negative damping ratio. With

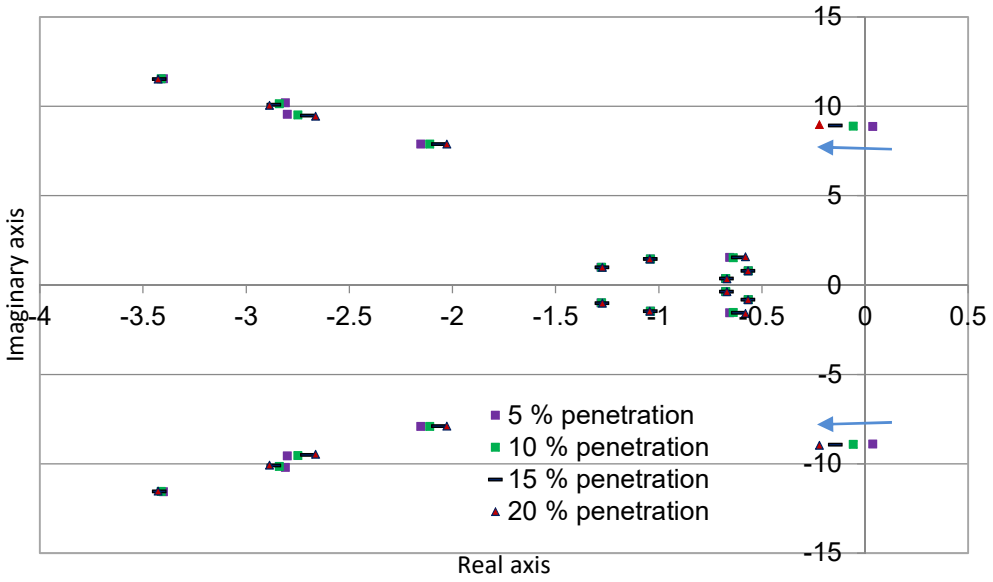

Figure 6.3 Movement of complex eigenvalues for the variation in wind penetration in the power system with HVDC link

the increased wind penetration the damping ratio is observed to be increased, contributing to the enhancement in the power system stability. However, with the voltage gain value of 20, the critical mode is seen to be located in the left side of the complex plane indicating stability of power system at all the penetration levels of the wind power. The critical mode exhibits a positive damping behaviour at all the penetration levels. Another observation shows that the damping of the critical mode

Table 6.5 Critical eigenvalue in the power system with HVDC link

Wind penetration			Real part (1/s)	Imaginary part (rad/s)	Damping ratio (%)	Frequency (Hz)
MW	Percent	Voltage gain				
18	5	10	0.038	8.880	–0.42	1.413
		20	–0.060	8.868	0.68	1.411
36	10	10	–0.058	8.901	0.65	1.417
		20	–0.157	8.887	1.77	1.414
54	15	10	–0.145	8.930	1.62	1.421
		20	–0.247	8.913	2.77	1.419
72	20	10	–0.222	8.968	2.47	1.427
		20	–0.331	8.947	3.69	1.424

increases as the penetration level of the wind farm increases.

From Fig. 6.4 it is observed that the HVDC link has contributed to the improvement of the damping ratio of the critical oscillatory mode. It is further observed that, even in the power system with the HVDC link, the higher voltage gain of the DFIG-based wind farm contributes to the improvement in the damping ratio of the critical mode. This observation is in line with the observation in the case of the power system without the HVDC link. At 5% penetration level, the oscillatory mode has a negative damping ratio of –0.0042 at the voltage gain value of 10 which increases to 0.0068 as the voltage gain increased to 20. Similarly, at 15% penetration level, the oscillatory mode has a damping ratio of 0.0162 at the voltage gain value of 10 which increases to 0.0277 when the voltage gain is increased to 20. Hence, it is observed that the DFIG-based wind farm increases the stability for increased wind penetration.

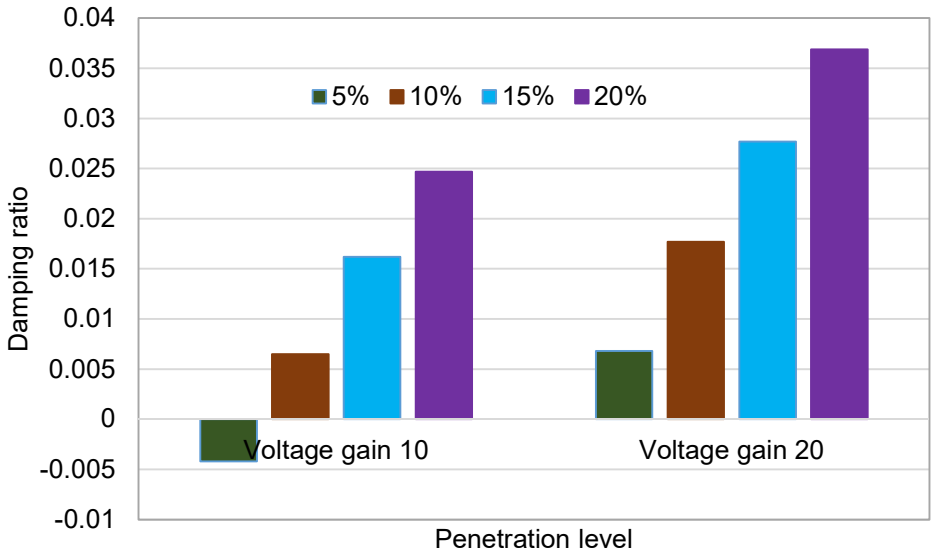

Figure 6.4 Change in the damping ratio of the critical eigenvalue for the variation in wind penetration in the power system with HVDC link

6.4 Comparative analysis and discussion

This section provides a comparative analysis of the complex eigenvalues in the power system at the 10% wind power penetration from the wind farm. Table 6.6 presents eigenvalues of the power system without an HVDC link. One of the complex eigenvalues has a positive real part making the power system unstable. The study is again performed with an HVDC link between bus-4 and bus-5, and the result is shown

Table 6.6 Complex eigenvalues in the power system without HVDC link

Complex eigenvalues	Real part (1/s)	Imaginary part (rad/s)	Damping ratio (%)	Frequency (Hz)
1	–43.817	8.014	0.984	1.276
2	–3.713	11.270	0.313	1.794
3	0.031	8.955	–0.003	1.425
4	–2.960	9.976	0.284	1.588
5	–2.689	9.410	0.275	1.498
6	–2.335	7.901	0.283	1.258
7	–0.683	1.469	0.422	0.234
8	–1.090	1.461	0.598	0.233
9	–1.232	0.984	0.781	0.157
10	–0.604	0.752	0.626	0.120
11	–0.664	0.360	0.879	0.057

Table 6.7 Complex eigenvalue in the power system with HVDC link

Complex eigenvalue	Real part (1/s)	Imaginary part (rad/s)	Damping ratio (%)	Frequency (Hz)
1	–43.799	8.064	0.983	1.283
2	–3.412	11.538	0.284	1.836
3	–0.058	8.901	0.007	1.417
4	–2.839	10.137	0.270	1.613
5	–2.749	9.522	0.277	1.516
6	–2.111	7.895	0.258	1.257
7	–0.640	1.534	0.385	0.244
8	–1.041	1.458	0.581	0.232
9	–1.277	1.000	0.787	0.159
10	–0.567	0.805	0.576	0.128
11	–0.674	0.362	0.881	0.058

in Table 6.7. It is observed that the HVDC contributes to the shifting of all the complex eigenvalues to the left half of the complex plane making the power system stable. The eigenvalues movement is shown in the Fig. 6.5. The figure demonstrates that the

critical eigenvalue moves to the stable region of the plot when the HVDC link replaces the line between bus-4 and bus-5. This study, thereby, shows that an HVDC link in a power system can contribute to increasing the small signal stability of a power system with a wind farm.

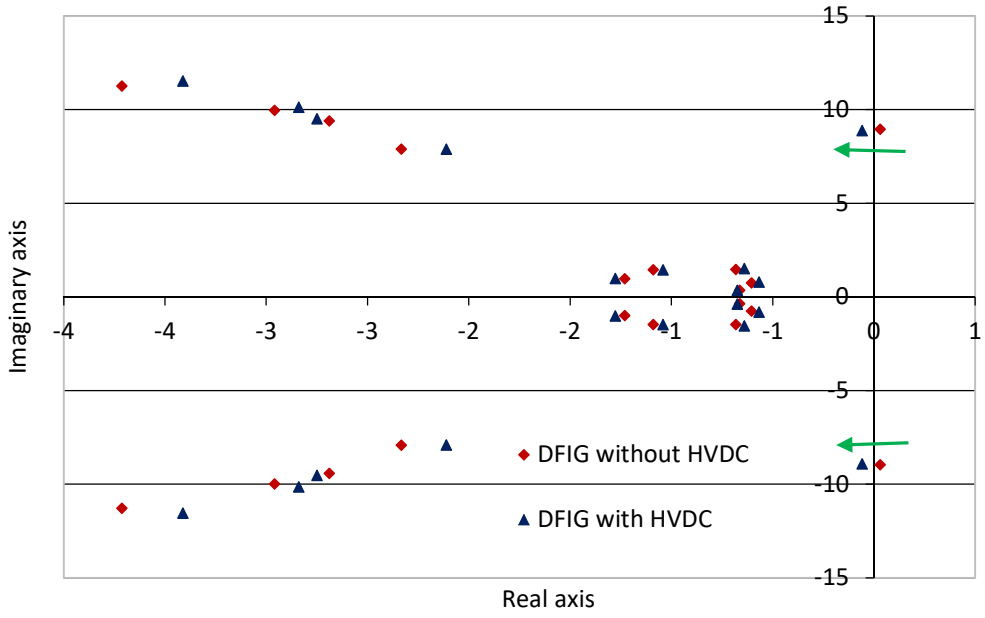

Figure 6.5 Movement of complex eigenvalues for the power system with and without HVDC link

6.5 Summary

The small signal stability of a power system for the different penetration levels of a DFIG-based wind farm is analysed and presented in this chapter. The study is conducted for the scenarios with and without an HVDC link in the test power system. The study shows that the power system with the DFIG-based wind farm improves the stability for 15 to 20 % penetration of the wind power. Another observation indicates that the voltage gain of the wind farm can contribute to improving the small signal stability of power system for different penetration levels of wind power. The small signal stability analysis performed with an HVDC connections shows that the power system with such dc links can exhibit improved stability for an increased wind power penetration from a DFIG-based wind farm.

Chapter 7 Stability improvement by a static synchronous series compensator

In this chapter, the stability of a power system with a DFIG-based wind farm is investigated and presented. The impact of a series FACTS device on the small signal and transient stability is demonstrated for different wind power penetration levels. In addition, eigenvalue sensitivity analysis for the degree of compensation and voltage gain is explored in this chapter. Time domain simulations are carried out to validate the study results.

7.1 Test system

The study is carried out on a modified 14-bus IEEE system [151] as shown in Fig. 7.1. The test power system has 66 kV, 18 kV, and 13.8 kV voltage levels. A bus-15 is added and connected to bus-5 via a line 5-15. A 60 MVA DFIG-based wind farm is connected at bus-15. An SSSC is installed at the line 5-15, and the stability analysis of the wind farm connected power system is conducted for the cases with and without the series compensation. The power system without the series device is considered as the base case of study. A sensitivity analysis is conducted to study the effect of the change in the degree of compensation of the SSSC device on the stability. The test system data is presented in Table 7.1 - 7.3. For the stability analysis, the wind farm is modelled as a single equivalent machine at bus-15.

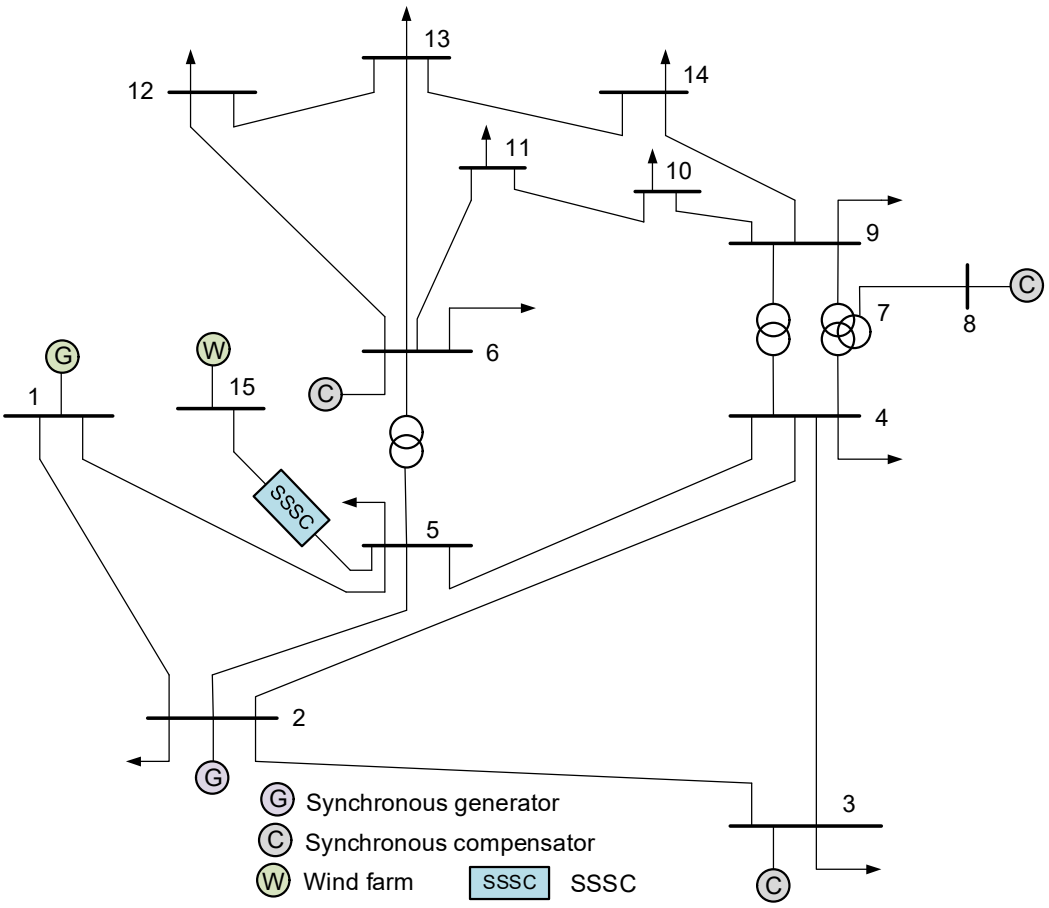

Figure 7.1 Modified IEEE 14-bus system

Table 7.1 Parameters of the new line

Line	Resistance, Ω	Reactance, Ω	Susceptance, F
bus-5 - bus-15	0.05403	0.22304	0.0492

Table 7.2 Parameters of the wind farm

Power rating, S_n, MVA	60
Stator resistance, r_s, Ω	0.031
Stator reactance, x_s, Ω	0.317
Rotor resistance, r_R, Ω	0.031
Rotor reactance, x_R, Ω	0.253
Magnetizing reactance, x_m, Ω	9.522

Table 7.3 Parameters of the SSSC device

Power rating, S_n, MVA	100
Operating mode	Constant voltage
Series compensation	23%

7.2 Small signal analysis without SSSC

At the base case, a wind farm is connected to the power system through a long line. This scenario assumes that a wind farm may be remotely located due to the availability of wind, and is connected to the power system through a long uncompensated line. The small signal analysis is carried out to observe the oscillation modes present in the power system, and the participation of the state variables on the oscillatory modes. There are 60 eigenvalues identified, and one complex pair lies in the right half of the imaginary axis. Hence, the system is unstable. The eigenvalues present in the power system is shown in Fig. 7.2.

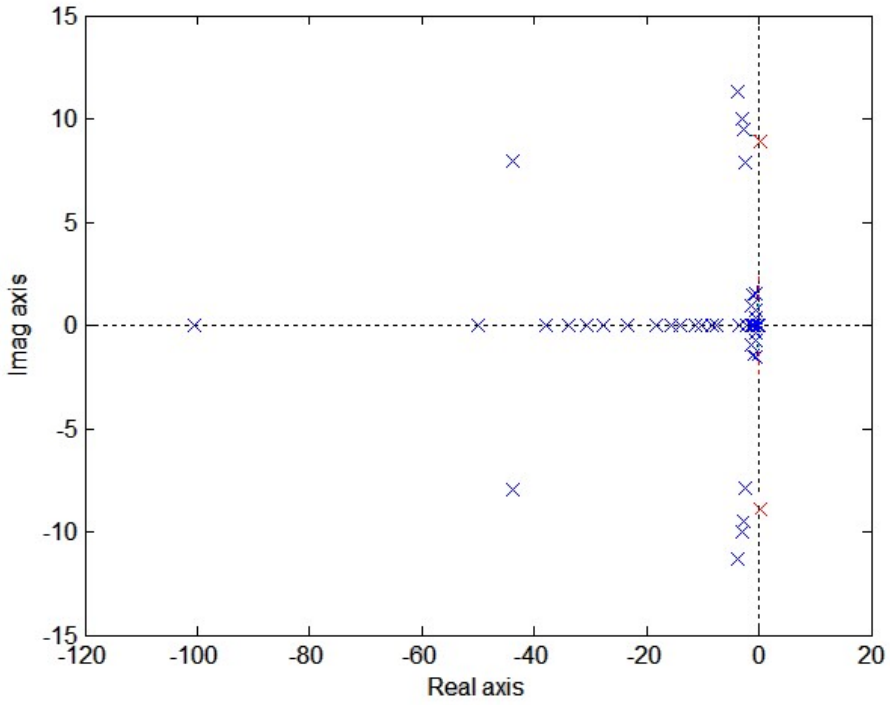

Figure 7.2 Eigenvalues of the uncompensated power system

From the analysis, 11 pairs of complex low frequency oscillatory modes are observed and are summarized in Table 7.4. The synchronous machine at bus-1 has the highest participation in the critical oscillatory mode, which is observed on the right half of the imaginary plane. The modes (1, 2), (15, 16), (17, 18), (19, 20) and (21, 22) are significantly damped. However, the oscillatory mode (5, 6) has negative damping with a positive real part magnitude of 0.015 and an imaginary part magnitude of 8.973. This means the power system has an oscillatory mode of increasing amplitude leading

power system to instability. This mode is critical to the power system stability and is referred to as the critical mode. Whereas, the remaining oscillatory modes have negative real parts, representing the damped oscillations. The frequencies of the oscillations are observed in the range of 0.057 to 1.793 Hz for all oscillatory modes existing in the power system.

Table 7.4 Oscillatory modes in uncompensated power system

Modes	Real part (1/s)	Imaginary part (rad/sec)	Damping ratio (%)	Frequency (Hz)
1,2	–43.817	8.023	98.40	1.277
3,4	–3.715	11.265	31.30	1.793
5,6	0.015	8.973	–0.20	1.428
7,8	–2.965	9.966	28.50	1.586
9,10	–2.679	9.397	27.40	1.496
11,12	–2.327	7.902	28.20	1.258
13,14	–0.694	1.364	45.30	0.217
15,16	–1.09	1.46	59.80	0.232
17,18	–1.231	0.984	78.10	0.157
19,20	–0.604	0.751	62.70	0.120
21,22	–0.662	0.359	87.90	0.057

Table 7.5 Participation of the state variables for uncompensated power system

Modes	Most associated states and values				
1,2	3 (0.322)	18 (0.449)	19 (0.114)	-	-
3,4	15 (0.281)	16 (0.282)	25 (0.161)	-	-
5,6	2 (0.248)	19 (0.200)	-	-	-
7,8	8 (0.156)	9 (0.158)	11 (0.180)	12 (0.181)	14 (0.099)
9,10	8 (0.164)	9 (0.166)	-	-	-
11,12	4 (0.259)	5 (0.260)	7 (0.119)	-	-
13,14	1 (0.333)	24 (0.215)	-	-	-
15,16	13 (0.334)	17 (0.124)	22 (0.315)	23 (0.116)	-
17,18	13 (0.121)	17 (0.364)	22 (0.114)	23 (0.338)	-
19,20	6 (0.423)	21 (0.402)	-	-	-
21,22	10 (0.438)	20 (0.414)	-	-	-

Table 7.5 summarizes the participation factors of the most associated states variables for the oscillatory modes. The state variables are represented by the numbers which are explained in section 7.6. The oscillatory mode (1, 2) has the dominant participation of the synchronous generator at bus-1, and the mode (3, 4) has that of the synchronous generator at bus-5. It is observed that the most associated state variables for the oscillatory mode (1, 2) are 3, 18 and 19, and their participation factors are 0.322, 0.449 and 0.114 respectively. The most associated state variables for the oscillatory mode (3, 4) are 15, 16 and 25, and their participation factors are 0.281, 0.282 and 0.161 respectively. Other states are also observed to have participated in these oscillatory modes, but the state variables with the dominant participation are only shown in the table.

7.3 Small signal analysis with SSSC

As a series compensation increases the transfer capacity of a line, the implementation of a solid state series FACTS device on a line connecting remotely located wind farm may be of interest to power producers, electric utilities and system operators. In such a context, the impact of a series FACTS device on the stability of a wind connected power system is of great importance. In this study, an SSSC is implemented on line 5-15, and its impact on the power system stability is studied. A series compensation usually lies between 20 to 70 % of the line inductive reactance [178]. However, for this study, the degree of series compensation is selected as 23% of the line reactance. This study shows 61 eigenvalues, and 11 pairs are the complex low frequency oscillatory modes. The eigenvalues present in the compensated power system is shown in Fig. 7.3. All the complex eigenvalues lie on the left half of the imaginary axis. Hence, the power system becomes stable with the implementation of the compensating device. The oscillatory modes are summarized in Table 7.6. The oscillatory mode (5, 6) has a negative real part of –0.090 and has a positive damping ratio of magnitude 0.010. With the compensation, the most of the oscillatory modes shift further left in the left plane, and corresponding frequencies of the oscillation are decreased. This results in an increased damping ratio of those oscillatory modes making the power system more stable. However, the mode (17, 18) and mode (21, 22) show a slightly decrease in damping ratio. Whereas for the mode (1, 2), the impact of the compensation is insignificant, and their damping ratio remains unchanged. The frequencies of the

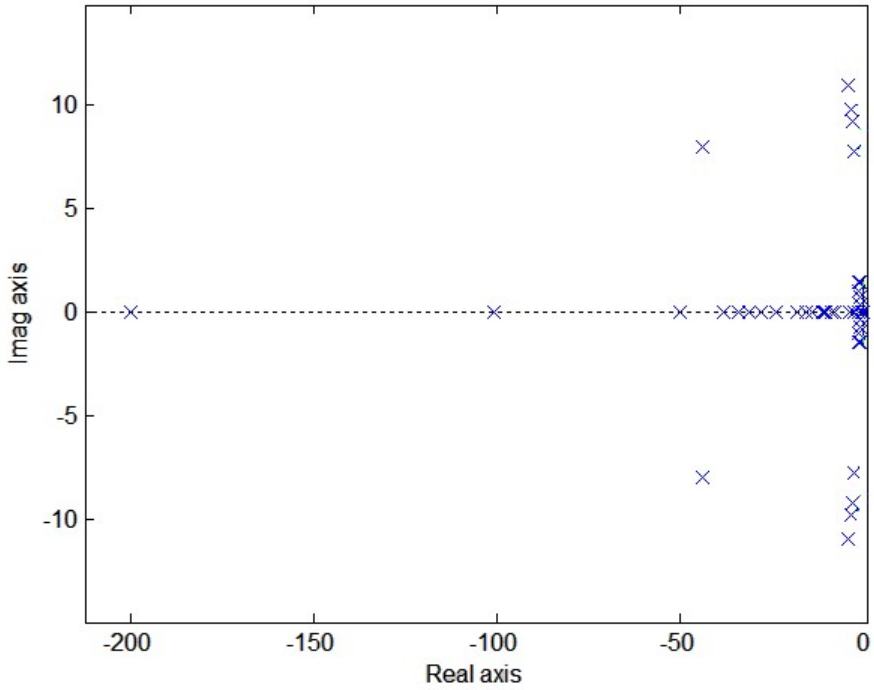

Figure 7.3 Eigenvalues of the compensated power system

oscillations are in the range of 0.057 to 1.741 Hz for all the oscillatory modes present in the compensated power system.

Table 7.7 shows the participation of the highly associated states to the oscillatory modes in the compensated power system. A comparison of Table 7.4 and 7.6 shows that in the mode (1, 2), the participation of the most associated states 3 and 19 remain unchanged. However, the state 18 indicates an increase from magnitude 0.449 to 0.45 as the compensation is implemented. The generator at bus-1 has dominant participation in the mode (1, 2), and the participation of the state variable remains unaffected with the compensation. In the mode (9, 10), the participation of the most associated states 8 and 9 increase their magnitude from 0.164 to 0.203, and from 0.166 to 0.205 respectively. This shows that increased participation of generator at bus-3 results in the damping of this mode. On the mode (21, 22), the participation of the most associated state ten increases from magnitude 0.438 to 0.44, and state 20 increases from 0.414 to 0.416. The increased involvement of these state variables results in the increased oscillation of that particular mode.

Table 7.6 Oscillatory modes in the compensated power system

Modes	Real part (1/s)	Imaginary Part (rad/sec)	Damping Ratio (%)	Frequency (Hz)
1,2	–43.857	8.017	98.40	1.276
3,4	–3.925	10.938	33.80	1.741
5,6	–0.090	9.022	1.00	1.436
7,8	–3.089	9.742	30.20	1.551
9,10	–2.668	9.164	28.00	1.459
11,12	–2.418	7.799	29.60	1.241
13,14	–0.753	1.296	50.20	0.206
15,16	–1.087	1.451	60.00	0.231
17,18	–1.218	0.986	77.70	0.157
19,20	–0.603	0.747	62.80	0.119
21,22	–0.650	0.357	87.60	0.057

Table 7.7 Participation factor of the state variables for the compensated power system

Modes	Most associated states and values				
1,2	3 (0.322)	18 (0.450)	19 (0.114)	-	-
3,4	15 (0.269)	16 (0.271)	25 (0.171)	-	-
5,6	2 (0.258)	19 (0.209)	-	-	-
7,8	8 (0.106)	9 (0.107)	11 (0.207)	12 (0.208)	14 (0.116)
9,10	8 (0.203)	9 (0.205)	-	-	-
11,12	4 (0.258)	5 (0.260)	7 (0.124)	-	-
13,14	1 (0.334)	24 (0.236)	-	-	-
15,16	13 (0.338)	17 (0.123)	22 (0.318)	23 (0.116)	-
17,18	13 (0.122)	17 (0.364)	22 (0.114)	23 (0.339)	-
19,20	6 (0.427)	21 (0.406)	-	-	-
21,22	10 (0.440)	20 (0.416)	-	-	-

7.4 Sensitivity analysis

For the sensitivity analysis, the degree of compensation (K_c) and voltage gain (K_v) are chosen as sensitivity parameters. The sensitivity of the real parts of the oscillatory

modes is studied in this chapter. Hence, the sensitivity of the different modes with respect to the compensation degree and voltage gain is obtained. The sensitivity is evaluated for a 0.5% increase and decrease in the sensitivity parameters. As the real part of an eigenvalue determines the stability of that mode, the sensitivity of the real part with respect to the change in sensitivity parameters is examined. The positive real part sensitivity indicates that with the change in the degree of compensation, the mode will move further left in the left half plane making the system more stable, and vice versa. In this study, the sensitivity is calculated by performing two eigenvalue calculations, one at the assumed degree of compensation, other at the perturbed values of the degree of compensation (K_c–ΔK_c).

Table 7.8 Eigenvalue sensitivity for the change in the degree of compensation

Modes	(K_c–ΔK_c)	(K_c+ΔK_c)
1,2	–0.000696	0.000696
3,4	–0.004000	0.004174
5,6	–0.003513	0.003565
7,8	–0.002435	0.002435
9,10	0.000435	–0.000522
11,12	–0.001478	0.001478
13,14	–0.000643	0.000652
15,16	–0.000087	0.000087
17,18	0.000174	–0.000174
19,20	0.000070	–0.000070
21,22	0.000383	–0.000400

The corresponding real part sensitivity values for each of the oscillatory mode, for an increased and decreased in the degree of compensation, are shown in Table 7.8. The result shows that with the increase in the compensation degree, the most of the oscillatory modes move further left in the left half plane making the power system more stable, and vice versa. The modes (3, 4), (5, 6), (7, 8) and (11, 12) are more sensitive to the change in the compensation degree as compared to the rest of the modes. This shows that the increase in the degree of compensation contributes to an increment in the power system stability. Likewise, another sensitivity analysis is performed with the change in the voltage gain of the DFIG as the sensitivity parameter.

In this study, the sensitivity is calculated by performing two eigenvalue calculations with voltage gain and at the perturbed values of the voltage gain ($K_v \pm \Delta K_v$).
Table 7.9 shows the eigenvalue sensitivities for an increase and decrease of the voltage gain of the DFIG based wind farm for the compensated and uncompensated power systems. In the uncompensated case, with the increase in the voltage gain, some of the oscillatory modes moves toward the right half plane making the power system unstable and vice versa. The modes (7, 8) and (9, 10) are more sensitive than the rest of the modes for the change in the voltage gain. In the compensated case, the most of the

Table 7.9 Eigenvalue sensitivity for the change in the voltage gain

Modes	Without compensation		With compensation	
	(K_v–ΔK_v)	(K_v+ΔK_v)	(K_v–ΔK_v)	(K_v+ΔK_v)
1,2	0	–0.0001	0.0001	0
3,4	0	0	0	0
5,6	0.00049	–0.00050	–0.00050	0.00051
7,8	0.001	0	0	0
9,10	–0.001	0.001	–0.0001	0.0001
11,12	0	0	0	0
13,14	0.0001	-0.0001	0.0001	0
15,16	0	0	0	0
17,18	0	0	0	0
19,20	0.0002	–0.0001	0.0001	–0.0001
21,22	0	–0.00001	0	0

oscillatory modes are insensitive to the change in the voltage gain. The modes (3, 4), (11, 12), (15, 16) and (17, 18) are insensitive to the change in voltage gain for both the uncompensated and compensated cases.

7.5 Analysis of transient stability

Transient stability indices (TSI) are calculated for the compensated and uncompensated cases. From the Table 7.10, it can be seen that with the implementation of the SSSC, the transient stability of the power system is improved. The increased

value of the TSI signifies an improvement in the transient stability of the power system with the compensation.

Table 7.10 Transient stability indices

Scenario	TSI
Without SSSC	6.6
With SSSC	9.5

The transient stability analysis is carried out to find the stability of the power system following a 3-phase fault. For the analysis, a 3-phase fault is simulated at time 0.0 sec on the line 2-5 near bus-5, and the fault is cleared by isolating the faulty line in 0.25 sec. The fault is simulated for the uncompensated and compensated cases. In the compensated case, a series FACTS device is implemented in the line 5-15, and the same fault is applied for both the cases to compare the impact of the series compensation on the transient stability. The swinging of the delta of the synchronous generators at bus-2 and bus-3 is shown in the Fig. 7.4. The difference in the rotor angles of the generators at bus-2 and bus-3 with respect to the generator at bus-1 shows improved damping for the compensated case. It signifies that the SSSC suppresses the swings in the rotor angle of the synchronous generators, and provides better damping characteristics to the oscillations by stabilizing the power system.

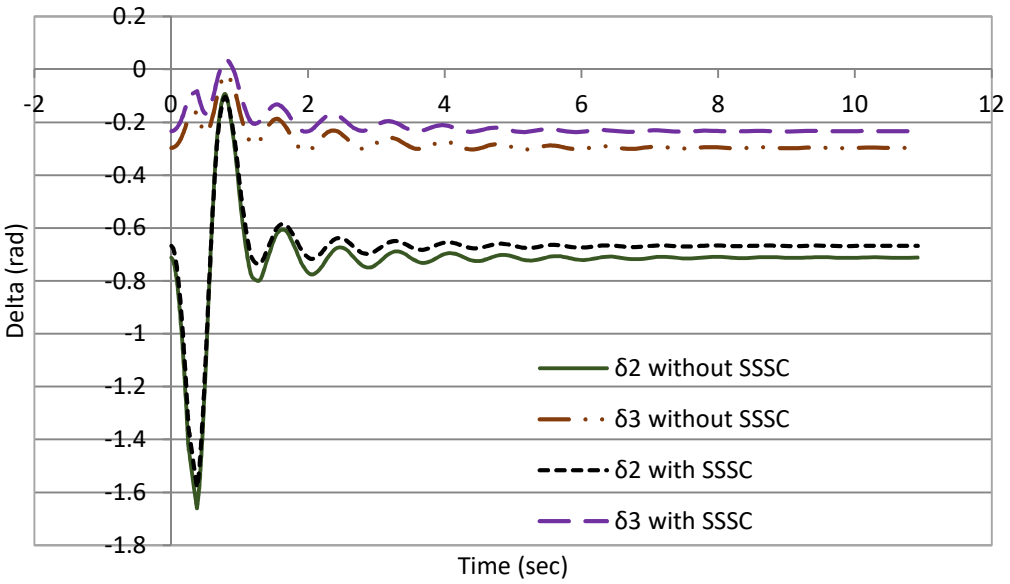

Figure 7.4 Swing curves of the generators at bus-2 and bus-3

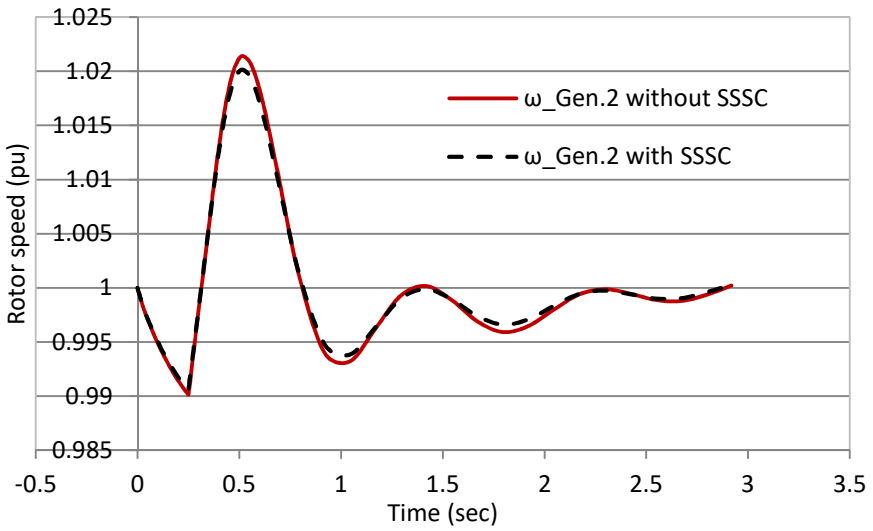

Figure 7.5 Response of the rotor speed of generator-2

Fig. 7.5 shows the rotor speed variation of the generator at bus-2. It is observed that the damping of the oscillation is improved with the series compensation of the line 5-15 as compared to the uncompensated power system. This shows that an SSSC can significantly improve speed oscillation damping of a synchronous generator during disturbances. Fig. 7.6 shows the voltage variations at bus-5 and bus-6 for the compensated and uncompensated cases. It is observed that with the compensation, the

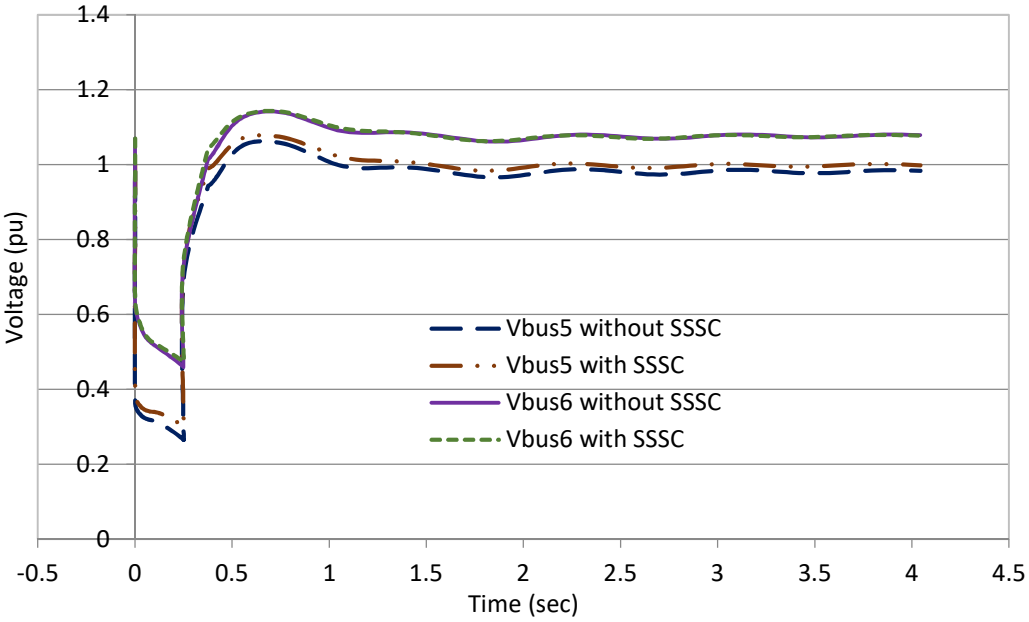

Figure 7.6 Response of the voltages of bus-5 and bus-6

voltages at both the buses are improved. Fig. 7.7 shows the terminal voltage at bus-15

for the compensated and uncompensated cases. Due to the compensation, the terminal voltage of bus-15 has been improved during and after the transient period, showing an improvement in the voltage stability of the power system. It shows that the SSSC has contributed in the voltage recovery performance of the power system following the disturbances. From the study, it is observed that the series compensation of the line connecting DFIG-based wind farm has a significant influence on the damping of the power system oscillations. Fig. 7.8 shows the rotor speed variation of the DFIG. It is observed that the rotor speed of the DFIG has shown an improved damping with the compensation.

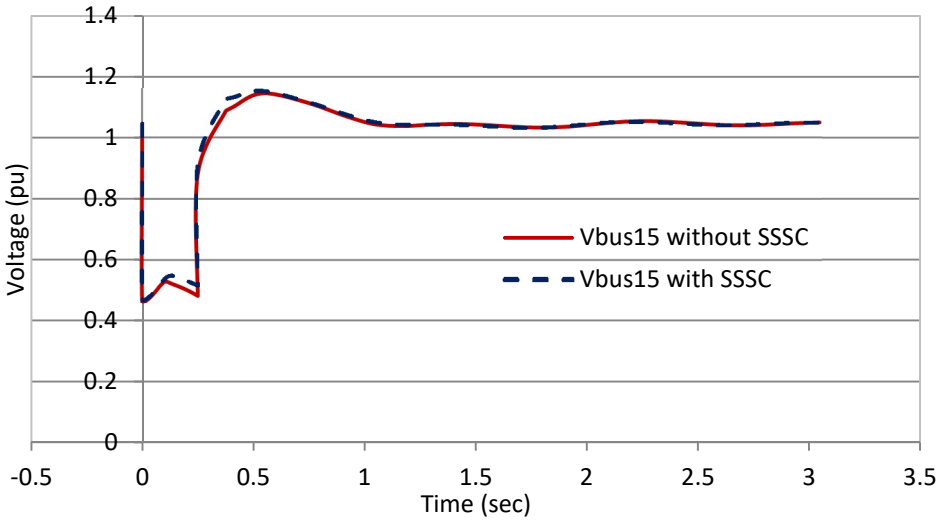

Figure 7.7 Response of the terminal voltage of the DFIG

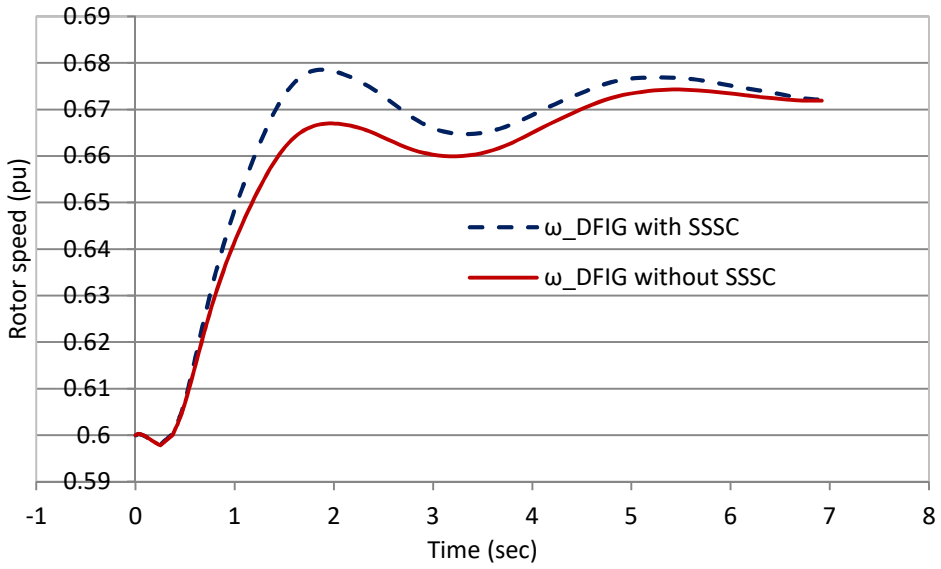

Figure 7.8 Response of the rotor speed of the DFIG

7.6 State variables

State variables listed in Table 7.11 exhibit a dominant association with the oscillatory modes. Sections 7.2 and 7.3 explain their participation on the oscillatory modes.

Table 7.11 State variables participated in the oscillatory modes

State numbering	State variables
1	ω of the synchronous generator at bus-1
2	e'_{q} of the synchronous generator at bus-1
3	e''_{q} of the synchronous generator at bus-1
4	δ of the synchronous generator at bus-2
5	ω of the synchronous generator at bus-2
6	e'_{q} of the synchronous generator at bus-2
7	e''_{d} of the synchronous generator at bus-2
8	δ of the synchronous generator at bus-3
9	ω of the synchronous generator at bus-3
10	e'_{q} of the synchronous generator at bus-3
11	δ of the synchronous generator at bus-4
12	ω of the synchronous generator at bus-4
13	e'_{q} of the synchronous generator at bus-4
14	e''_{d} of the synchronous generator at bus-4
15	δ of the synchronous generator at bus-5
16	ω of the synchronous generator at bus-5
17	e'_{q} of the synchronous generator at bus-5
18	e'_{d} of the synchronous generator at bus-1
19	v_{fd} of the synchronous generator at bus-1
20	v_{fd} of the synchronous generator at bus-2
21	v_{fd} of the synchronous generator at bus-3
22	v_{fd} of the synchronous generator at bus-4
23	v_{fd} of the synchronous generator at bus-5
24	δ at the synchronous generator at bus-1
25	e''_{d} of the synchronous generator at bus-5

7.7 Summary

The impact of the series FACTS device on the stability of the modified IEEE 14-bus power system is studied in this chapter. The line connecting remote the wind farm to the power system is compensated with a series FACTS for the study. An eigenvalue sensitivity is conducted with respect to the variation in the degree of compensation, and the voltage gain of the DFIG based wind farm as the sensitivity parameters. The small signal analysis shows 11 pairs of oscillatory modes in the power system. The low frequency oscillatory modes are observed to be of the frequency range of 0.057 to 1.793 Hz. The implementation of the series FACTS device shows an improvement in the damping ratio and the frequency of oscillations of the most of the oscillatory modes. The transient stability analysis shows an improved oscillation of the rotor angles. Similarly, the rotor speed of the synchronous generators shows an improvement in their damping performance for the compensated power system as compared to the uncompensated case power system.

Chapter 8 Stability analysis of a microgrid

In this chapter, a holistic small signal stability analysis of is performed to assess the impact of the quantities, ratings, and characteristics of a microgrid's building components on its stability. To this end, a frequency stability index metric is formulated and employed to express the microgrid's stability variation by conducting a sensitivity type analysis. Furthermore, both radial and loop configurations of a microgrid are focused and conducted a comparative analysis.

8.1 Test system

The study is carried out on a test microgrid system for its radial and loop configurations as shown in Fig. 8.1a-b. Both of these microgrids are presumed to have a synchronous generator, DG, BES and load (respectively connected to bus-1 to bus-4) with those structures and internal controllers discussed in Section 3.6 of chapter 3. Table 8.1 lists the assumed technical data of the microgrid system components.

For a real microgrid hosting multiple quantities of synchronous generators, DGs, BESs and loads, their internal parameters might differ from each other; however, for the sake of simplicity, these internal parameters are assumed similar in the studies of this chapter. To neutralise the impact of a relatively large or small source, the synchronous generators, DG and BES are assumed to have the same rating. Thereby, the microgrid's stability will not be biased towards one specific source type. This can be seen in the technical data of Table 8.1. Based on this assumption, the droop coefficients of the sources are determined and provided in this table. However, the BES has an extra parameter of the SoC that will affect its droop coefficient as given by 3.49 and 3.50 (refer section 3.6.2). To consider this impact, the BES's SoC is assumed as 50% and based on that the droop coefficients of the BES are determined. Later, another study is conducted to evaluate the microgrid's stability when the SoC varies.

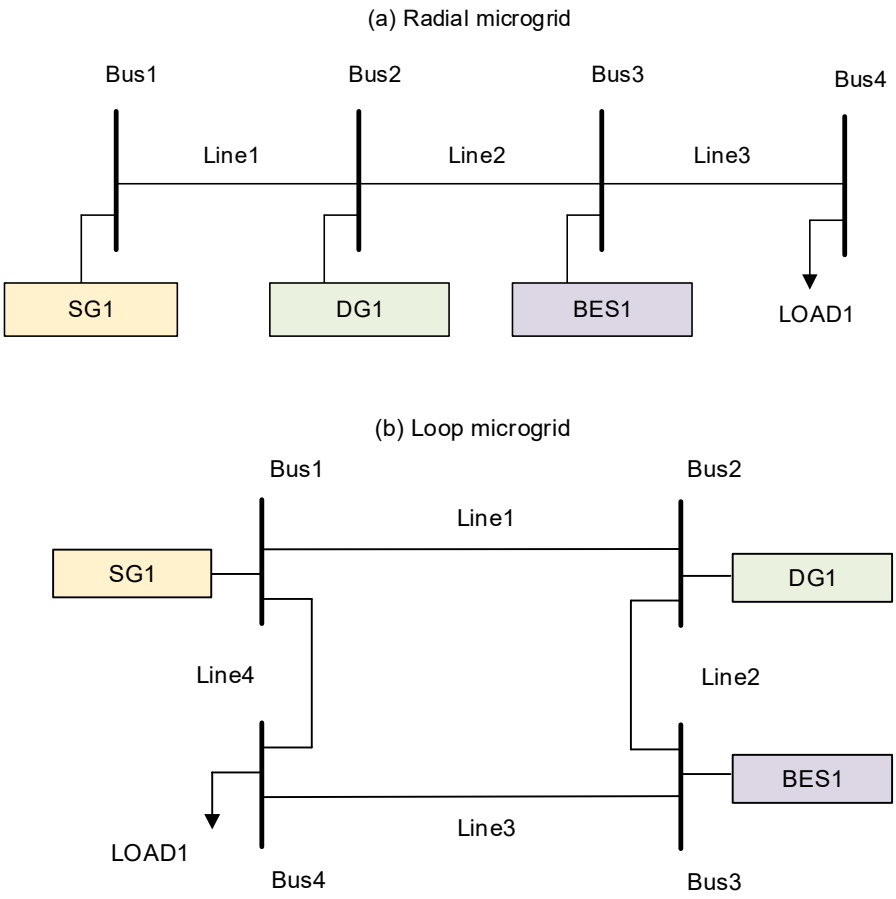

Figure 8.1 Considered radial and loop configurations of microgrid

Table 8.1 Assumed technical parameters

Voltage and frequency: V^{b} = 230 V, V^{max} = 235.75 V, V^{min} = 224.25 V, f^{b} = 50 Hz, f^{max} = 50.5 Hz, f^{min} = 49.5 Hz
Ratings of synchronous generator, DG and BES: $S_{SG}^{cap} = S_{DG}^{cap} = S_{BES}^{cap} = 5.3$ kVA, $P_{SG}^{cap} = P_{DG}^{cap} = 4$ kW, E^{cap} = 5 kWhr
Parameters of synchronous generator: N_p = 2, r_s = 0.0952 Ω, r_{k1q} = 0.0565 Ω, r_{k2q} = 0.2669 Ω, r_{kd} = 0.4234 Ω, $X_d = X_q$ = 57.132 Ω, $X_{md} = X_{mq}$ = 51.1014 Ω; X_{k1q} = 76.8902 Ω, X_{k2q} = 54.0818 Ω, X_{kd} = 53.6803 Ω
Parameters of VSCs of DG and BES: V_{dc} = 400 V, a = 2, R_f = 0.1 Ω, L_f = 0.367 mH, C_f = 50 μF, L_T = 13.6 mH, k_1 = 6.18, k_2 = 2.29, k_3 = 22.96, ω_c = 31.4159 rad
Droop coefficients: $m_{SG} = m_{DG}$ = 0.25 Hz/kW, m_{BES} = 0.5 Hz/kW, $n_{SG} = n_{DG}$ = 0.285 V/kVar, n_{BES} = 0.14 V/kVar
SoC of BES: SoC = 50%
Load: Z_{load} = 100 + j 3.5 Ω/phase
Line: Z_{line} = 0.2 + j 2 Ω/phase

8.2 Microgrid's stability analysis

The stability of microgrid is analysed with the variation of the quantity and the rating of its building components.

8.2.1 Base case

Assuming *P-f* operating point droop coefficients for synchronous generator, DG and BES respectively as 0.25, 0.25 and 0.5 Hz/kW while their *Q-V* operating point droop coefficients are respectively 0.285, 0.285 and 0.14 Hz/kVar, the formulated SSS technique determines the FSI of the radial and loop microgrids as respectively 8.55 and 7.35 %. It can be observed that a microgrid with a loop configuration has a slightly lower frequency deviation stability margin versus a radial one with the same building components. Fig. 8.2 presents the dominant eigenvalue trajectories of the radial and loop microgrids whereas Table 8.2 provides the characteristics of those eigenvalues including their real and imaginary parts and those state variables that have a strong influence on them (see Section 7.3). It is seen from this table and that the radial microgrid has a complex-conjugate dominant eigenvalues pair that is considerably affected by the output current states of the DG and BES, as well as the current flowing through line-2 (i.e., the interlinking line between them). On the other hand, it is seen that the loop microgrid exhibits two complex-conjugate dominant eigenvalues pairs that are strongly affected by the output current states of all sources as well as the current states of line-3 (i.e., the interlinking line between the load and BES). Fig. 8.3 illustrates the overall influence of each state variable of the microgrid (i.e., $\mathbf{x}_{MG}$) on each eigenvalue for the radial microgrid from which the percentages of influence are given in Table 8.2 for each dominant eigenvalue.

Table 8.2 Critical eigenvalues and their characteristics

Microgrid	Real part (1/s)	Imaginary part (rad/s)	Damping Ratio (%)	Frequency (rad/s)	Effective states (%)
Radial	–17.47	321.23	5.43	321.70	$(i_2^d, i_2^q)_{BES}$ 39%, $(i_2^d, i_2^q)_{DG}$ 33%, $(i^d, i^q)_{line\text{-}2}$ 09%
Loop	–9.00	315.40	2.85	315.53	$(i^d, i^q)_{SG}$ 52%, $(i_2^d, i_2^q)_{BES}$ 34%, $(i_2^d, i_2^q)_{DG}$ 11%,
	–16.66	321.61	5.17	322.04	$(i_2^d, i_2^q)_{BES}$ 40%, $(i_2^d, i_2^q)_{DG}$ 36%, $(i^d, i^q)_{line\text{-}3}$ 10%

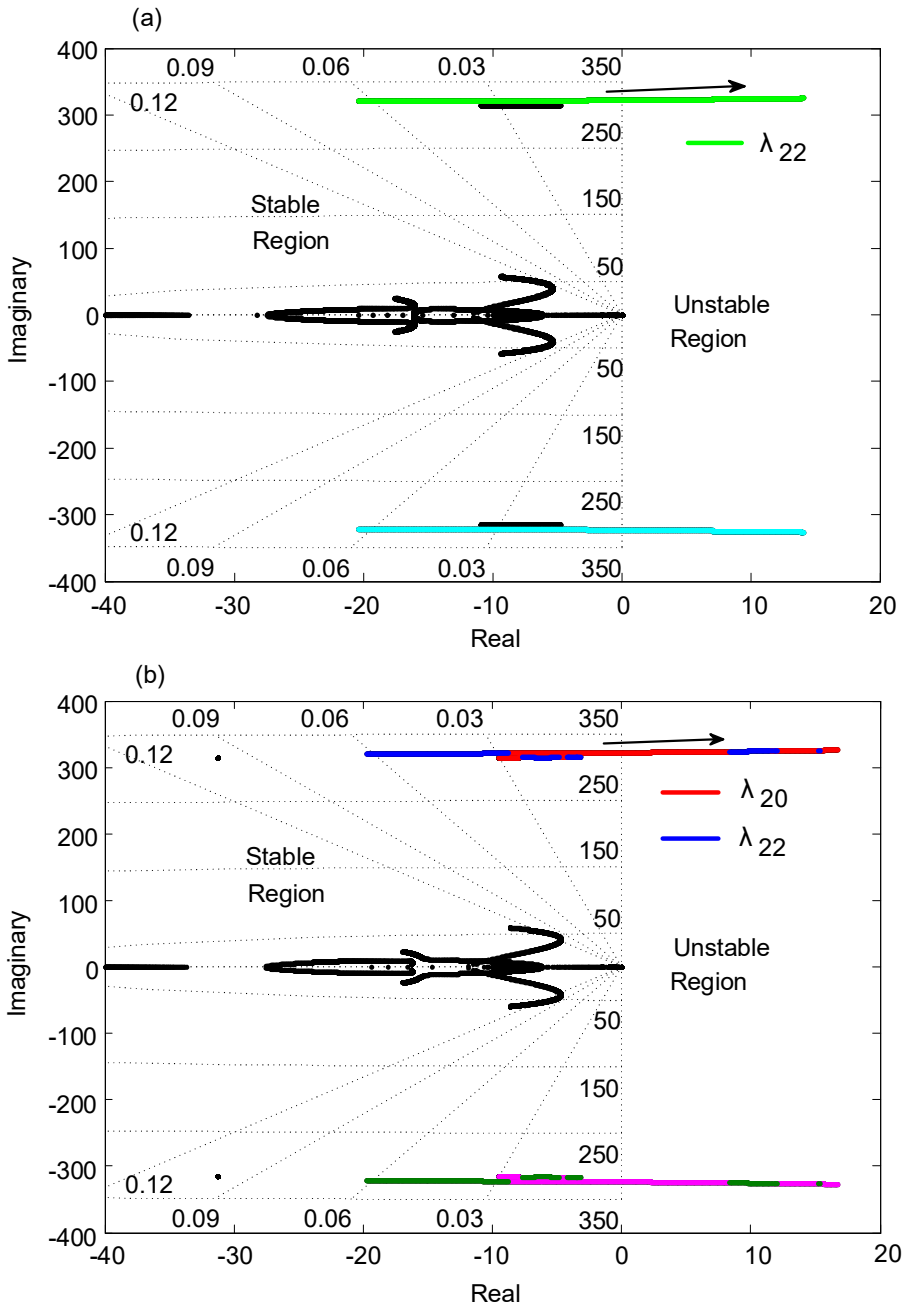

Figure 8.2 Dominant eigenvalue trajectories of a) radial and b) loop microgrids

8.2.2 Variation in the rating of sources

To examine the influence of the rating of the sources within a microgrid on its stability, a sensitivity analysis is conducted. To this end, first let us assume that the rating of the synchronous generator, DG and BES in both radial and loop microgrids increases from 20% of their nominal value given in Table 8.2 to twice of that in steps

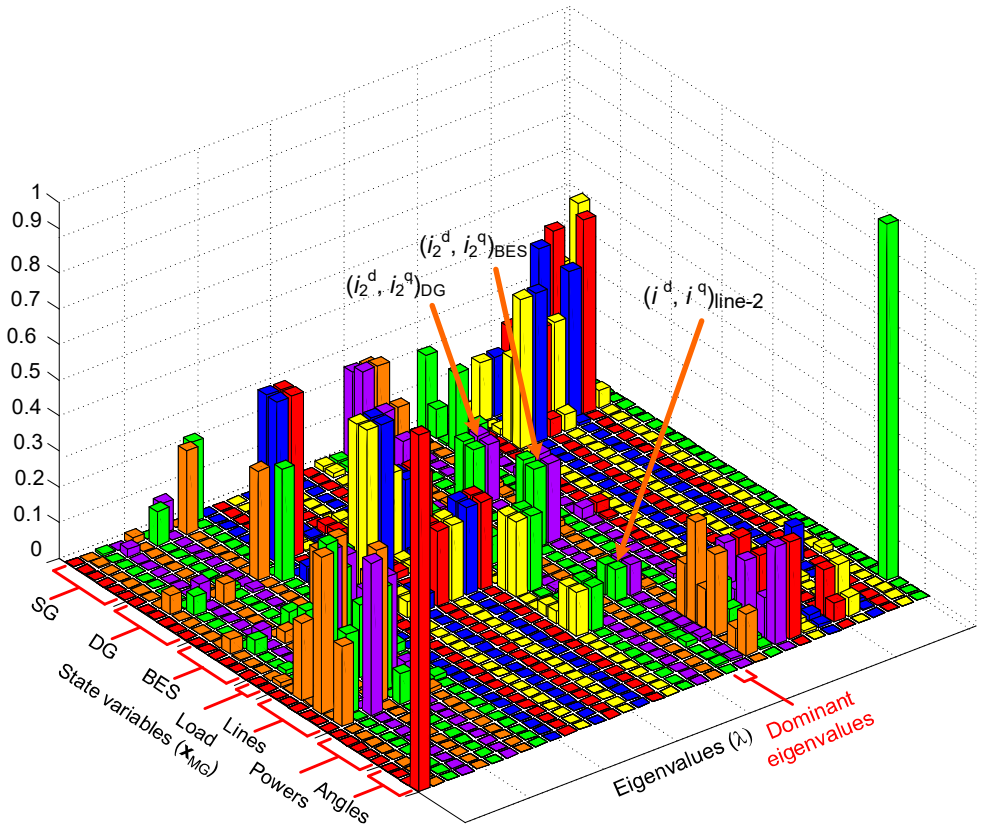

Figure 8.3 Participation factor presentation for the radial microgrid

of 20% while all the rest of the technical parameters remain constant. Fig. 8.4a illustrates the variations of the microgrids' FSI and shows that it rises linearly in the radial microgrid to 1.3 times of its initial value with the increase in the synchronous generator's rating while it increases significantly by respectively 3.8 and 4 times for an increase in the rating of DG and BES. In the loop microgrid, the increase in FSI follows a similar trend for the rating of synchronous generator and DG. However, it rises even higher and about 5.6 times for an increase in the rating of the BES. This figure also shows that both microgrids become unstable when the rating of the DG and BES is respectively 20 and 60 % of the nominal capacities given in Table 8.2. It can also be observed from this study that a variation in the capacity of BES has the maximum influence on the microgrids' FSI and the impact is higher for the loop microgrid. On the other hand, it can be seen that a change in the synchronous generator's nominal capacity has the least effect on the FSI of both microgrids. Another observation is that FSI increases with a larger rate at the lower ratings of DG whereas it saturates when the rating increases above 150% of the assumed nominal capacity.

Another study is performed to analyse the effect of the variation of BES's SoC on the microgrids' FSI. To this end, the energy capacity of the BES is assumed to remain constant while its SoC is increased from 10 to 100 %. Fig. 8.4b illustrates the results of this study from which it can be seen that the FSI increases from 2.95 to 15.3 % for the radial microgrid while it rises from 1.85 to 14.25 % for the loop one. Thereby, it can be concluded that operating BESs in the discharging mode, when they have a larger SoC, significantly improve the stability of the microgrid while it may jeopardize the stability when their SoC is very close to their SoC^{min}.

8.2.3 Variation in quantities of sources

Another study is conducted in which the number of the synchronous generators, DGs and BESs are increased in both microgrids from 1 to 10. This has been processed in two different methods. In the first method, it is assumed that all added sources have the same nominal capacity as the initial one; thus, a rise in the source's number increases the overall supply capacity of the microgrid. However, in the second method,

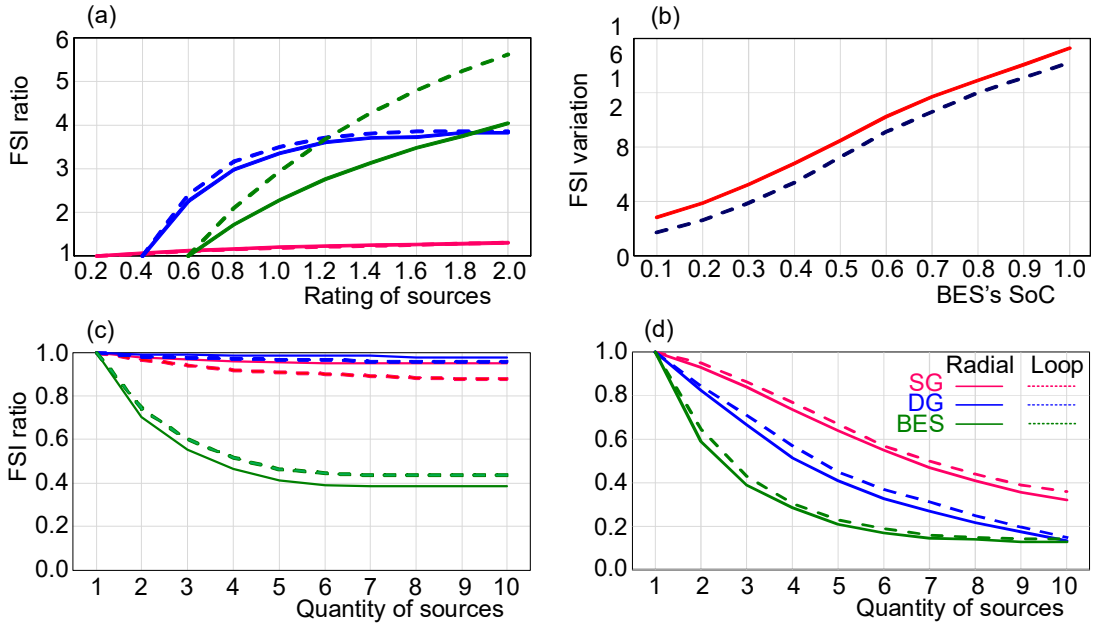

Figure 8.4 Variation of FSI for change in (a) sources nominal capacity, (b) BES's SoC, (c) sources number while the total generation capacity increases, (d) sources number while the total generation capacity is constant

this capacity is assumed to remain constant albeit the increase in the number of sources. To this end, with an increase in the number of sources, the rating of each source is decreased linearly. The results of these two studies are provided in Fig. 8.4c-d. As seen

in Fig. 8.4c (for the first method), the FSI decreases by 5% as the number of synchronous generators increases in the radial microgrid while it decreases by only 2% in the case of DG. However, FSI decreases by 60% for the increase in the number of BESs. Likewise, in the loop microgrid, the FSI decreases with an increase in the number of the sources. However, the decrease is lesser than of the radial microgrid in case of BES while is higher than in case of the synchronous generators and DGs.
On the other hand, Fig. 8.4d (for the second method) shows that the FSI decreases almost linearly for the increase in the number of synchronous generators and DGs for both microgrids. This decreases very rapidly when the BES number increases from 1 to 4 while it nearly saturates when the number of BESs increases above that. It is also observed that by increasing the number of synchronous generators, DGs and BESs from 1 to 10, the FSI drops to almost 36, 14 and 15% of the initial condition.

8.2.4 Variation in synchronous generator's internal parameters

To evaluate the effect of some internal parameters of synchronous generators on the microgrids' FSI, another study is performed. First, the influence of V_{ref} is analysed by

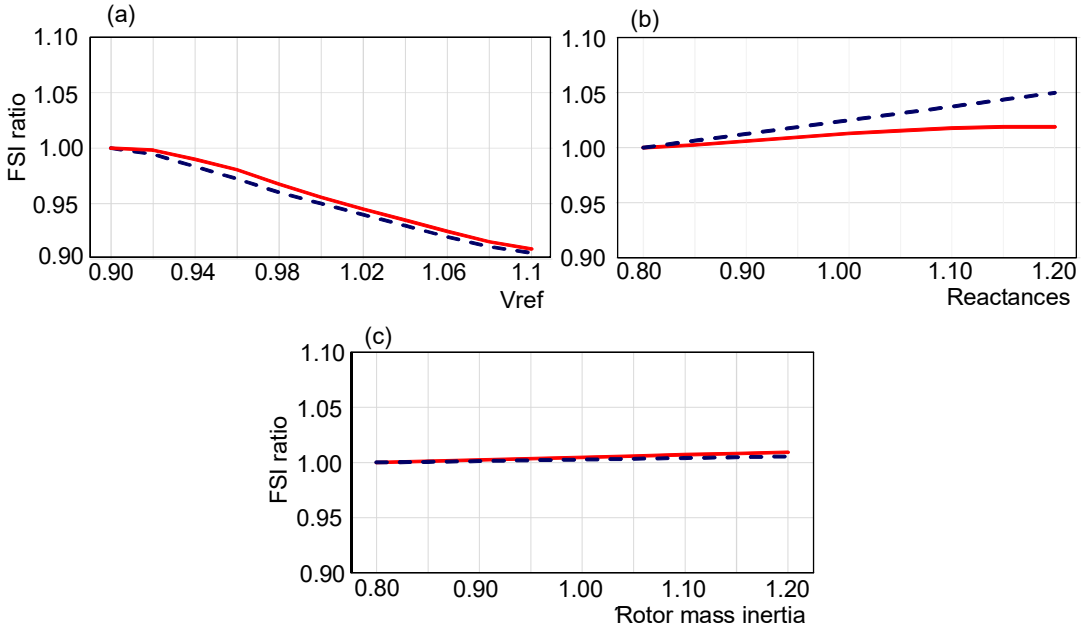

Figure 8.5 Variation of FSI for change in (a) synchronous generator's excitation voltage, (b) synchronous generator's reactances, (c) synchronous generator's rotor mass inertia

varying it from 90 to 110 % of the nominal value (i.e., 1 pu). Fig. 8.5a illustrates the change of the FSI in this study and shows a 10% decrease for a 20% increase in V_{ref}.

As synchronous generators designed by various manufacturers may have different stator winding dq-axis reactive impedances of X_d and X_q (which is employed in (4)), a second study is carried out to examine the influence of the variation of these parameters on the microgrid's FSI. To this end, these inductances are varied from 80 to 120% of the nominal values given in Table 8.2 and the microgrid's FSI variation is provided in Fig. 8.5b. It can be observed from this figure that this change increases the FSI by 2% in the radial microgrid and by 5% in the loop one. Likewise, various designs of synchronous generators may exhibit different rotor mass inertia (J_r). Thus, a third study is conducted to demonstrate the effect of the variation of the synchronous generator's rotor mass on the FSI of the microgrids. Fig. 8.5c shows that the FSI remains almost unaffected when the synchronous generator's rotor mass increase from 80 to 120 % of the nominal value for both radial and loop microgrids.

From the above studies, it can be concluded that although the microgrid's FSI decreases with the increase in V_{ref} and with a decrease in its X_d and X_q inductances, it is not significantly influenced by the internal parameters of the synchronous generator.

8.2.5 Variation in loads

To measure the effect of the number of loads in the microgrid, another study is carried out in which the number of loads is increased in both microgrids from 1 to 10. This has been processed in two different methods. In the first method, it is assumed that all added loads have the same rating as the initial one; thus, a growth in the number increases the total loading of the microgrid. However, for the second method, the total load of the microgrid is supposed to remain constant albeit the increase in their number. Fig. 8.6a illustrates the variation in the microgrids' FSI for the first method and shows that the FSI increases from 8.55 to 8.95 % as the number of the load increases in the radial microgrid. Similarly, for the loop microgrid, the FSI increases from 7.35 to 8 %. For the second method, as presented in Fig. 8.6b, the FSI increases slightly from 8.55 to 8.65% for the radial microgrid while an increase of 7.35 to 7.45 % is observed for the loop one. The main observation from both of the studies is that the FSI is sensitive to the number of load increase when the total demand of the microgrid increases. In contrary, when the total demand is constant, the FSI is sensitive to the change in the number of loads only when their number is small.

A second study is conducted to assess the influence of the power factor of the load on

the microgrids' FSI. To this end, the load's power factor is changed from 0.1 to 0.98 lagging while keeping its apparent power constant. Fig. 8.6c demonstrates the results of this study and shows that for the radial microgrid, the FSI decreases from 8.95 to 8.55 %. Similarly, the FSI decreases from 7.6 to 7.35 % for the loop microgrid.

The above studies show that the change in the number of loads impacts the microgrid's FSI and this figure is higher for loads with a low power factor.

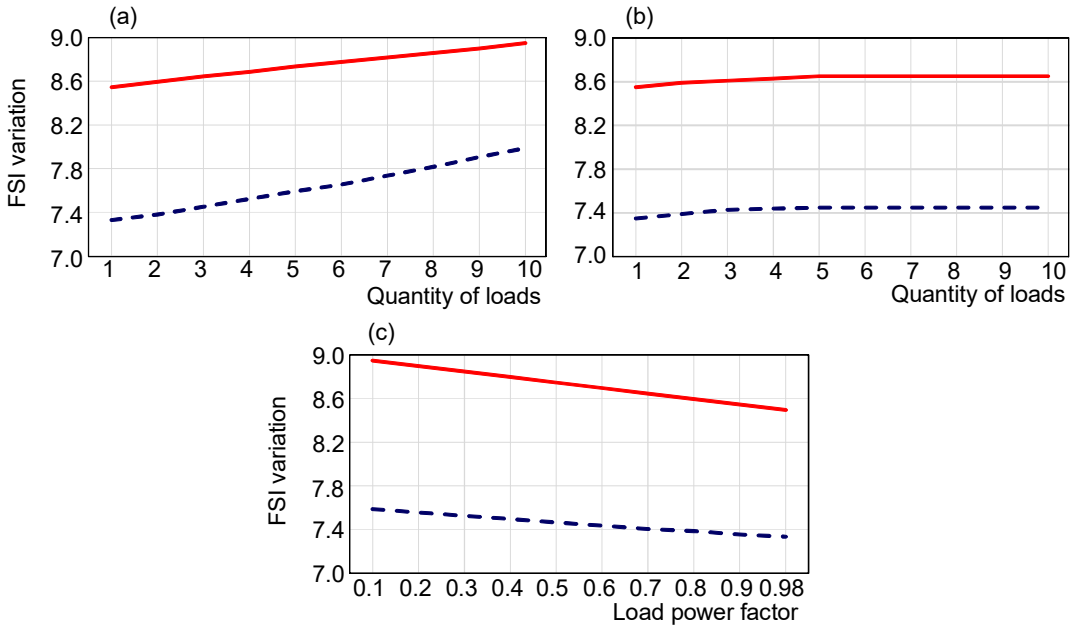

Figure 8.6 Variation of FSI for change in (a) load number for the change in total demand, (b) load number for the constant total demand, (c) load power factor

8.2.6. Variation in lines

To evaluate the effect of the line parameters on the microgrids' FSI, another study is performed. First, it is assumed that the length of all lines within the microgrids are varied from 20% of their initial values given in Table 8.2 to twice of that while the rest of the technical parameters are thought to be constant. Fig. 8.7a illustrates the FSI for this study and shows an increase from 5.05 to 12.5% for the radial microgrid and an increase of 4.7 to 10.4% for the loop one. Thus, the microgrid observes higher stability when the building components are significantly isolated by conductors with either larger lengths or impedances.

The above study has evaluated the impact of the microgrid's overall expansion or shrinkage. A second study is performed to assess the influence of the variation in an

individual line length (impedance) within the microgrid. Only the loop configured microgrid is considered for this study. First, the lines between every two sources are varied, one line at a time, from 20 to 200% of the nominal impedance given in Table 8.2. The results of this study are provided in Fig. 8.7b and shows that the FSI is more sensitive to the change in line length (impedance) between two non-inertial sources (i.e., the DG and BES) compared to that between an inertial and non-inertial (i.e., synchronous generator and DG, or synchronous generator and BES). The observed FSI varies in this case from 4.5 to over 9%. At the second stage, the length (impedance) of the line between a source and the load is varied. Fig. 8.7c shows the results of this study and illustrates that the FSI is less sensitive to the variation in the length (impedance) of the line between a BES and load while it is almost equally sensitive to that between synchronous generator and load, or DG and load.

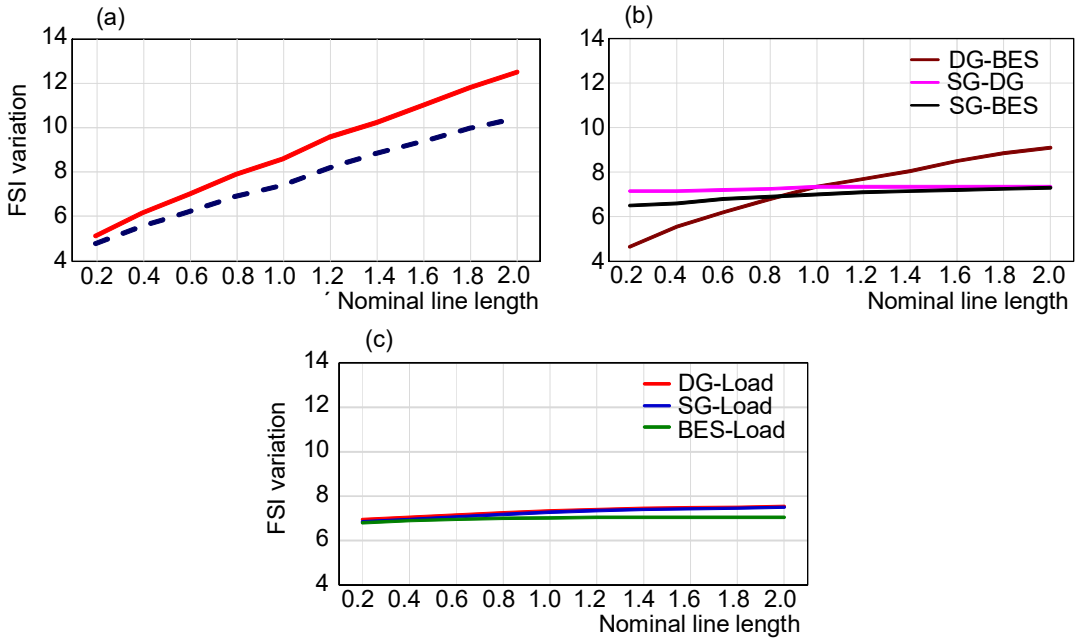

Figure 8.7 Variation of FSI for change in (a) microgrid's line lengths (b) distance between sources, (c) distance between a source and load

A third study is also carried out to assess the influence of the lines' X/R ratio. To this end, the X/R ratio is assumed as 0.1, 1 and 10 for all the lines and the FSI variation is presented in Fig. 8.8a. The first 3 scenarios are for the cases with R_{line} = 0.2 Ω while in the second 3 scenarios X_{line} = 0.2 Ω. From this figure, it can be seen that for the radial microgrid, the FSI is 7.85% for the scenario -1 and 2 while it slightly increases to 8.6% for scenario-3. However, for the loop microgrid, the FSI continuously

increases from 6.8 to 7.45% with an increase in X/R and drops to 4.15% for the scenario -6. Thus, it can be concluded that the microgrid's stability increases as the lines become more inductive up to a limit beyond which the microgrid's stability decreases.

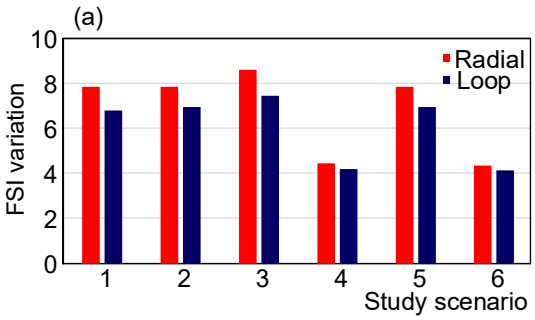

Figure 8.8 Variation of FSI for change in (a) X/R ratio of microgrid's lines

8.3. Findings for designing more stable microgrids

Table 8.3 summarises the overall findings of the above sensitivity analyses and aims to introduce the highest and lowest influencing parameters on the stability of a microgrid from the perspective of its building components (i.e., synchronous generators, DGs, BESs, loads and lines). It can be seen from this table that the rating

Table 8.3 Summary of the frequency stability index variation within studies

Considered parameters	Highest influencing factor	Least influencing factor
Source rating increase	BES	SG
Source quantity increase while overall capacity rises	BES	SG, DG
Source quantity increase while overall capacity is constant	DG, BES	SG
Line	Length (impedance) and X/R; Line between DG and BES	Line between a source and load; and a SG and DG/BES
Overall highest influencing factors	DG's rating, BES's rating and SoC, and line impedances	
Factors with no or almost insignificant influence	Internal parameters of sources and load's quantity, rating and power factor	

and SoC of BESs (with the structure and control discussed in Section 2) have the

highest influence on the stability of a microgrid and can rise its stability by almost four times. These two factors are determined as the first and second largest influencing factors for the microgrid's stability. It can also be seen that the increasing the rating of a synchronous generator or its quantity within a microgrid has the least influence when the microgrid's total generation capacity remains constant and does not influence the stability by more than respectively 30 and 10%. Another observation is that the influence of the sources also depends on the microgrid configuration. As an example, the variation impact of BESs' rating and the quantity of synchronous generators and DGs is more prominent for a microgrid with a loop configuration versus one with a radial one.

Furthermore, as seen from this table, in terms of synchronous generators' internal parameters, the studies show that the variation of the excitation voltage reference, the stator winding's dq-axis reactances, and its rotor mass inertia do not influence the microgrid's stability by more than 10%.

Table 8.3 also shows that the variation in loads' quantity has a higher effect on the microgrid's stability when the total demand of the microgrid increases with an increase in the load quantity versus when the total demand is constant; however, this impact is very small compared to the other factors discussed above and does not exceed by more than 1%.

It can also be seen from Table 8.3 that the line impedances are the third most significant factor affecting the microgrid's stability and is more pronounced in radial microgrids. Additionally, among individual lines, it can be seen that the interlinking line between a DG and BES exhibits a huge impact to the microgrid's stability whereas the interlinking line between a synchronous generator and DG has the least effect. Similarly, it is seen that the line interlinking a synchronous generator to the load has the higher influence on a loop microgrid's stability versus that interlinking other sources to the load.

Thus, the above findings can be summarised as:

- Those building components of a microgrid that benefit its stability are: (a) increasing the rating of a DG and BES (see Fig. 8.4a); (b) operating a BES under the discharging mode when its SoC is significant (see Fig. 8.4b); (c) decoupling the building components by using lines with suitably larger impedances and X/R ratios (see Fig. 8.7a and 8.8a),
- Those building components of a microgrid that detriment its stability is increasing

the number of sources while maintaining the microgrid's overall supply capacity constant (see Fig. 8.4d) in addition to the contraries of those mentioned above.

- Those building components of a microgrid that are almost neutral on its stability are: (a) internal parameters of sources (see Fig. 8.5a-c); (b) the quantity, rating and power factor of the loads (Fig. 8.6a-c).

8.4 Summary

This paper presents a detailed and scalable holistic small signal model of a microgrid and uses the developed platform to analyse the impact of various parameters of its building components such as synchronous generators, DGs, BESs, loads and lines to derive a general understanding of the microgrid's stability. Through a sensitivity type analysis, two assumed radial and loop microgrid's stability margin variation is analysed versus a change in the quantity and rating as well as the internal parameters of the components mentioned above. The studies show that the rating of a DG and BES, as well as the BES's SoC and line impedances can strongly impact the stability of the microgrid while the internal parameters of sources as well as the quantity, rating and power factor of the loads do not influence that.

Chapter 9 Conclusions and recommendations

This chapter summarises the important findings of this thesis. Based on different finding and observations, some recommendations are also made for future researchers.

9.1 Conclusions

This thesis investigated the impact of high penetration of wind power on the low frequency oscillatory modes, and also identified the influences of different control devices on such oscillations. The capability of such control devices to enhance the transient stability of wind integrated power system is also explored in this thesis. At the distribution network, as the voltage stability is more of an issue, this thesis investigated the influence of wind power on the voltage stability of a distribution feeder with a wind farm when integrated at a weak part of the feeder. Finally, the small signal stability of a microgrid network was examined to enhance the design of such microgrids hosting a cluster of inertial and non-inertial DGs.

In an integrated power system, the low frequency oscillations exist due to small disturbances caused by variations in loads and generation. Such oscillations are observed in the range of 0.1 to 3 Hz frequency mainly due to insufficient damping of the oscillations. In a real power network, these oscillations could place the power system in a significant threat from the stability and reliability perspective. When wind power is integrated, the modes of oscillation are influenced positively or negatively. Therefore, considerable attention must be given to understand such influences, when the wind power reaches a significant penetration level. At such levels, the wind integration could cause a considerable reduction in the total inertial contribution from the generating system. This condition could result in a change in the electromechanical torque, which could thereby lead to low frequency oscillations. Exploring the damping capability of the control devices, and the design of a supplementary controller showed

positive interactions with the high wind power. Thereby, enhancing the damping capability of the power system to damp power oscillations positively.

Firstly, the impact of a series FACTS device on the small signal stability of a power system was studied. The line connecting a remote wind farm to the power system was compensated with a series FACTS device, and the study was conducted to observe the influence of the device on the stability. Eleven pairs of complex eigenvalues were detected with the frequency of oscillations in the range of 0.057 to 1.793 Hz. At the uncompensated power system, a pair of complex eigenvalue was observed on the unstable region of the eigenvalue plot, making the power system unstable. The pair was found to be moved to the stable region with the implementation of the series FACTS device, enabling stable operation of the power system. Additionally, the application of the FACTS device showed an improvement in the damping ratio and the frequency of oscillations of the most of the eigenvalues detected. An eigenvalue sensitivity study was conducted to observe the sensitivity of the power system stability to the change in the degree of compensation and the voltage gain of the wind farm. It was observed that the complex eigenvalues were sensitive to the degree of compensation, with the increase in the degree of compensation the eigenvalues were observed to move to the more stable region. However, the most of the complex eigenvalues were insensitive to the change in the voltage gain of the wind farm.

Apart from the above study, small signal stability for different penetration levels of a DFIG-based wind farm integrated power system, with and without an HVDC link, was also analysed in this thesis. In the power system without an HVDC link, a pair of complex eigenvalue was observed to have an oscillation of increasing amplitude for a low wind penetration of about 5%, making the power system unstable. When the wind penetration was increased from 5 to 20 %, the oscillation was observed to be better damped, thereby, increasing the power system stability. This observation showed that the increase in wind penetration contributed to the damping of the critical eigenvalue. Similarly, the study of an HVDC link integrated power system showed an enhancement in the damping of the critical eigenvalue when compared to the cases without the link for all the 5 to 20 % wind power penetration levels analysed in this thesis. This observation showed that an HVDC link assisted to enable higher penetration of wind power by contributing to the enhancement in the low frequency power oscillation damping. Further to this, the wind farm was observed to have better damping capability when was operated at its higher voltage gain values irrespective of

the wind power penetration level in the power network.

Additionally, an SVC-based supplementary controller was designed and implemented in a wind farm connected power system to provide an additional damping capability of the device to damp power oscillations. The study was conducted for 20 and 60 MW penetration levels of wind power from a DFIG-based wind farm. Twelve pairs of complex eigenvalues were observed in the frequency range of 0.06 to 2.01 Hz. A critical eigenvalue was observed to have a damping ratio of 2.07 and 4.08 % respectively at 20 and 60 MW wind penetration levels. The implementation of the SVC device contributed to enhancing the damping ratio of the critical mode to 4.09 and 5.24 % respectively for the above mentioned penetration levels. In the end, a supplementary controller was designed to provide an additional damping capability to the SVC device. The study showed that the designed controller provided damping of over 15 % to the critical eigenvalue for both the penetration levels. A sensitivity analysis showed that the critical eigenvalue was sensitive to the change in total system load and less sensitive to the change in wind penetration.

At the distribution level, the steady state and transient voltage stability with and without a remote DFIG-based wind farm were analysed in this thesis. The analysis of the bus voltages responses showed an improvement in the voltages of all the buses of the distribution system with the wind integration. From the steady state analysis, it was observed that the voltage improvement was higher at the buses in the proximity of the wind farm as compared to the distant buses. The maximum loading margin of the distribution buses was observed to be improved with the wind penetration. However, the increment in the loading margin was higher for the buses near the wind farm. In the end, the study was conducted to observe the response of the distribution system for the common types of distribution faults. The transient voltage stability analysis for 3-phase faults, sudden loss of motor load, and motor starting show that the wind farm can contribute to improve the voltages and to damp the oscillations during and following the studied transient conditions. Hence, the study showed that a distant DFIG-based wind farm could improve the steady state and transient voltage response capability of a weak distribution system.

Finally, this thesis presents a comprehensive small signal modelling of a microgrid. The developed model was used to analyse the impact of various parameters of microgrid components such as various sources, loads and lines to develop an understanding of the test microgrid's stability. A sensitivity analysis was adopted using

which two assumed radial and loop microgrids' stability margin was analysed with a change in the quantity and rating as well as the internal parameters of the microgrid building components. The studies showed that variation in certain parameters significantly influences the microgrid stability. However, the stability was less or not affected by variation in other parameters considered in the analysis.

The main outcomes of this thesis can be summarised as:

- A series FACTS device can enhance the stability of power system for the evacuation of power from a remote wind farm. The studies show that the stability improvement becomes more effective with the increase in the degree of series compensation.
- An HVDC link in a power system enables higher penetration of wind power due to the enhancement in the damping of low frequency oscillations.
- A DFIG-based wind farm connected at a remote weak distribution network can improve the steady state and transient voltage response capability of the distribution system
- A supplementary controller can be integrated with a shunt FACTS device to enhance the damping of power oscillations in a power system to enable higher penetration of wind power.
- The frequency stability of a microgrid is influenced by the variation in the parameters of its building power components.

9.2 Recommendations

This thesis has not considered the following stability aspects of the wind power (renewable) integration in power systems and microgrids. I recommend other researchers to work in this line in future.

- In a complex power system where multiple low frequency oscillatory modes are to be damped, a coordinated control system with multiple controllers could be an effective way of damping power oscillations.
- Voltage stability of a transmission and sub-transmission system could be an issue in near future due to the high penetration of wind power, given that the renewable penetration has significantly increased in the recent years.

Therefore, the voltage stability issues in the transmission system might need an attention.

- At the microgrid level, the stability impacts of coupling and decoupling MGs versus the penetration levels of different renewable resources could be an interesting study.
- This research had studied the influence of the variation in the parameters of a microgrid in its frequency stability margin. The variation in the microgrid's voltage stability with respect to the parameters of the microgrid could be a future research avenue.
- In the studies of this research, the application of the *P-f* droop control was focused in microgrids of remote areas. The key benefit (advantage) of such a droop control is its simplicity and lack of necessity for any communication system, which makes the remote area microgrids more economic. A future research avenue in studying the frequency stability margin of the microgrid when other types of controllers have been utilised.

References

[1] International Energy Agency, “Executive summary: Energy technology perspectives 2012 pathways to a clean energy system”. Available: https://www.iea.org/publications/freepublications/publication/ETP2012SUM.pdf.

[2] Wind Energy Foundation, “History of wind energy”, 2015. [Online]. Available: http://windenergyfoundation.org/about-wind-energy/history/.

[3] Global Wind Energy Council, “Global wind statistics 2017”. [Online]. Available: http://gwec.net/wp-content/uploads/vip/GWEC_PRstats2017_EN-003_FINAL.pdf.

[4] American Wind Energy Association, “Wind power closes 2017 strong, lifting the American economy”. [Online]. Available: https://www.awea.org/resources/press-releases/2018/wind-power-closes-2017-strong,-lifting-the-america.

[5] RenewEconomy, “Graph of the day: Wind capacity set to nearly double in 5 years”, [Online]. Available: https://reneweconomy.com.au/graph-of-the-day-wind-capacity-set-to-nearly-double-in-5-years-77214/.

[6] Australian Government Geoscience Australia, “Wind energy”, 2018. [Online]. Available: http://www.ga.gov.au/scientific-topics/energy/resources/other-renewable-energy-resources/wind-energy.

[7].Clean Energy Council, “Clean energy Australia report”, 2016. [Online]. https://www.cleanenergycouncil.org.au/policy-advocacy/reports/clean-energy-australia-report.html.

[8] Global Wind Energy Council, “Global wind report annual market update 2013”. [Online]. Available: http://www.gwec.net/publications/global-wind-report-2/global-wind-report-2013.

[9] P. Kundur, Power system stability and control, New York: McGraw Hill, 1994.

[10] P. Kundur, J. Paserba, V. Ajjarapu, G. Andersson, A. Bose, C. Canizares, N. Hatziargyriou, D. Hill, A. Stankovic, C. Taylor, T. Van Cutsem and V. Vittal,

"Definition and classification of power system stability," IEEE Transactions on Power Systems, vol. 19, no. 2, pp. 1387-1401, May 2004.

[11] L. Chang, "Wind energy conversion systems," [Online]. Available: www.ieeetmc.com/reg/7/canrev/canrev40/chang.pdf.

[12] S. Y. C. Kong, "Advanced control and analysis of wind and solar energy systems," Ph.D. Thesis, The University of Queensland, Australia, 2011.

[13] S. Mathew, "Wind energy: fundamentals, resources analysis and economics," Kerala, India: Springer, 2006.

[14] B. Babypriya and R. Anita, "Modelling, simulation and analysis of doubly fed induction generator for wind turbines," Journal of Electrical Engineering, vol. 60, no. 2, pp. 79-85, 2009.

[15] H. Ibrahim, M. Ghandour, M. Dimitrova, A. Ilinca, and J. Perron, "Integration of wind energy into electricity systems: technical challenges and actual solutions," Energy Procedia, vol. 6, no. 1, pp. 815-824, 2011.

[16] Y. Sun, L. Wang, G. Li, and J. Lin, "A review on analysis and control of small signal stability of power systems with large scale integration of wind power," International Conference on Power System Technology (POWERCON). China, pp. 1-6, 24-28 October 2010.

[17] J. G. Slootweg, "Wind power, modelling and impact on power system dynamics," Ph.D. Thesis, Delft University of Technology, Delft, Netherlands, 2003.

[18] K. Elkington, V. Knazkins, and M. Ghandhari, "On the rotor angle stability of power systems with doubly fed induction generators", Power Tech IEEE Lausanne, Stockholm, pp. 213-18, Sweden, 1-5 July 2007.

[19] H. Pingping, D. Ming, and L. Binbin, "Study on transient stability of grid-connected large scale wind power system," IEEE International Symposium on Power Electronics for Distributed Generation Systems, Hefei, China, pp. 621-625, 2010.

[20] G. Tsourakis, B. M. Nomikos, and C. D. Vournas, "Effect of wind parks with doubly fed asynchronous generators on small-signal stability," Electric Power Systems Research, vol. 79, no. 1, pp. 190-200, January 2009.

[21] M. Stiebler, "Wind energy systems for electric power generation," Springer-Verlag Berlin Heidelberg, 2008.

[22] N. Modi, "Advanced control methodology for improving small-signal stability of a large electricity network," Ph.D. Thesis, The University of Queensland, 2012.

[23] S. Q. Bu, W. Du, H. F. Wang, Z. Chen, L.Y. Xiao, and H. F. Li. "Probabilistic analysis of small-signal stability of large-scale power systems as affected by penetration of wind generation," IEEE Transactions on Power Systems, vol. 27, no. 2, pp. 762-70, 2012.

[24] J. L. Dominguez-Garcia, O. Gomis-Bellmunt, F. D. Bianchi, and A. Sumper, "Power oscillation damping supported by wind power: A review," Renewable and Sustainable Energy Reviews, vol. 16, no. 1, pp. 4994-5006, 2012.

[25] M. R. Shah, "Enabling large-scale PV in power system: Small-disturbance angle stability enhancement," Ph.D. thesis, The University of Queensland, 2013.

[26] T. Ackermann, Wind power in power systems, West Sussex, England: John Wiley & Sons Ltd, 2005.

[27] S. Y. Kong, R. C. Bansal, and Z. Y. Dong, "Comparative small-signal stability analyses of PMSG-, DFIG- and SCIG-based wind farms," International Journal of Ambient Energy, vol. 33, no. 2, pp. 87-97, 2012.

[28] D. Gautam, V. Vittal, R. Ayyanar, and T. Harbour, "Supplementary control for damping power oscillations due to increased penetration of doubly fed induction generators in large power systems," in Power Systems Conference and Exposition (PSCE), Phoenix, AZ, pp. 1-6, 20-23 March 2011.

[29] D. Gautam, V. Vittal, and T. Harbour, "Impact of increased penetration of DFIG-based wind turbine generators on transient and small signal stability of power systems," IEEE Transaction on Power Systems, vol. 24, no. 3, pp. 1426-1434, 2009.

[30] A. Ostadi, A. Yazdani, and R. K. Varma, "Modelling and stability analysis of a DFIG-based wind-power generator interfaced with a series-compensated line," IEEE Transactions on Power Delivery, vol. 24, no. 3, pp. 1504-1514, July 2009.

[31] R. Grunbaum, "FACTS for grid integration of wind," in IEEE PES Innovative Smart Grid Technologies Conference, Gothenberg, Sweden, pp. 1-8, 11-13 October 2010.

[32] J. G. Slootweg, and W. L. Kling, "The impact of large scale wind power generation on power system oscillations," Electric Power Systems Research, vol. 67, no. 1, pp. 9-20, October 2003.

[33] C. Wang, L. Shi, L. Yao, L. Wang, Y. Ni, and M. Bazargan, "Modelling analysis in power system small signal stability considering uncertainty of wind generation," IEEE Power and Energy General Meeting, pp. 1-7, 2010.

[34] F. M. Hughes, O. Anaya-Lara, N. Jenkins, and G. Strbac, "A power system stabilizer for DFIG-based wind generation," IEEE Transactions on Power Systems, vol. 21, no. 2, pp. 763-772, May 2006.

[35] R. D. Fernandez, R. J. Mantz, and P. E. Battaiotto, "Impact of wind farms on a power system. An eigenvalue analysis approach," Renewable Energy, vol. 32, no. 10, pp. 1676-1688, August 2007.

[36] J. C. Munoz and C. A. Canizares, "Comparative stability analysis of DFIG-based wind farms and conventional synchronous generators," in IEEE Power System Conference and Exposition (PSCE), Phoenix, AZ, pp. 1-7, 20-23 March 2011.

[37] J. Chaudhary, A. Mitra, and D. Chatterjee, "Effect of doubly fed induction generator based wind farms on the small signal stability of multi-machine power system," International Conference on Power and Energy Systems (ICPS), Chennai, India, 22-24 December 2011.

[38] C. Wang, L. Shi, L. Wang, and Y. Ni, "Small signal stability analysis considering grid-connected wind farms of DFIG type," in IEEE Power and Energy Society General Meeting-Conversion and Delivery of Electrical Energy in the 21st Century, Pittsburgh, PA, pp. 1-6, 20-24 July 2008.

[39] M. Jafarian and A. M. Ranjbar, "Interaction of the dynamics of doubly fed wind generators with power system electromechanical oscillations," IET Renewable Power Generation, vol. 7, no. 2, pp. 89-97, March 2013.

[40] D. Gautam and V. Vittal, "Impact of DFIG based wind turbine generators on transient and small signal stability of power systems," in IEEE Power and Energy Society General Meeting, Calgary, AB, pp. 1-6, 26-30 July 2009.

[41] B. Mehta, P. Bhatt, and V. Pandya, "Small signal stability analysis of power systems with DFIG based wind power penetration," Electrical Power and Energy Systems, vol. 58, no. 1, pp. 64-67, June 2014.

[42] A. Mendonca and J. A. Peas Lopes, "Impact of large scale wind power integration on small signal stability," in International Conference on Future Power Systems, Amsterdam, vol. 1, no 1, pp. 1-5, 18 November 2005.

[43] T. Knuppel, J. N. Nielsen, K. H. Jensen, A. Dixon, and J. Ostergaard, "Small-signal stability of wind power system with full-load converter interfaced wind turbines," IET Renewable Power Generation, vol. 6, no. 2, pp. 79-91, March 2012.

[44] C. Liu, Z. Chen, C. Bak, et al., “Transient stability assessment of power system with large amount of wind power penetration: The Danish case study,” in IEEE Conference on Power & Energy, Ho Chi Minh City, pp. 461-467, 2012.

[45] L. Shi, S. Sun, L. Yao, Y. Ni, and M. Bazargan, “Effects of wind generation intermittency and volatility on power system transient stability,” IET Renewable Power Generation, vol. 8, no. 5, pp. 509-521, 2014.

[46] M. S. Sarkhanloo, A. S. Yazdankhan, and R. Kazemzadeh, “A new control strategy for small wind farm with capabilities of supplying required reactive power and transient stability improvement”, Renewable Energy, Vol. 44, pp. 32-39, 2012.

[47] C. Eping, J. Stenzel, M. Poller, and H. Muller, “Impact of large scale wind power on power system stability,” in International Workshop on Large-Scale Integration of Wind Power and Transmission Networks for Offshore Wind Farms, pp. 1-9, April 2005.

[48] H. Li, B. Zhao, C. Yang, H. W. Chen, and Z. Chen, “Analysis and estimation of transient stability for a grid-connected wind turbine with induction generator,” Renewable Energy, vol. 36, no. 5, pp. 1469-76, 2011.

[49] W. Qiao and R. Harley, “Effect of grid-connected DFIG wind turbines on power system transient stability,” in Power and Energy Society General Meeting, Pittsburgh, PA, pp. 1-7, 2008.

[50] M. Dicorato, G. Forte, and M. Trovato, “Wind farm stability analysis in the presence of variable-speed generators,” Energy, vol. 39, no. 1, pp. 40-47, 2012.

[51] M. V. A. Nunes, J. A. Pecas Lopes, H. H. Zurn, U. H. Bezerra, and R. G. Almeida, “Influence of the variable-speed wind generators in transient stability margin of the conventional generators integrated in electrical grids,” IEEE Transactions on Energy Conversion, vol. 19, no. 4, pp. 692-701, December 2004.

[52] W. Hongbin and M. Ding, “Modelling and control of distribution system with wind turbine generators,” in International Conference on Electric Utility Deregulation and Restructuring and Power Technologies, Nanjuing, pp. 2498-2503, 6-9 April 2008.

[53] J. W. Smith and D. L. Brooks, “Voltage impacts of distributed wind generation on rural distribution feeders,” in IEEE/PES Transmission and Distribution Conference and Exposition, Atlanta, GA, vol. 1, pp. 492-497, 28 October- 02 November 2001.

[54] E. Muljadi, C. P. Butterfield, J. Chacon, and H. Romanowitz, “Power quality aspects in a wind power plant,” Power Engineering Society General Meeting, pp. 8-16, June 2006.

[55] C. Zheng and M. Kezunovic, “Distribution system voltage stability analysis with wind farms integration,” in North American Power Symposium (NAPS), Arlington, TX, pp. 1-6, 26-28 September 2010.

[56] Y. Chi, Y. Liu, W. Wang, and H. Dai, “Voltage stability analysis of wind farm integration into transmission network,” in International Conference on Power System Technology, Chongqing, pp. 1-7, 22-26 October 2006.

[57] J. Zhao, X. Li, J. Hao, and J. Lu, “Reactive power control of wind farm made up with doubly fed induction generators in distribution system,” Electric Power Systems Research, vol. 80, no. 1, pp. 698-706, 2010.

[58] M. M. Aly and M. Abdel-Akher, “Voltage stability assessment for radial distribution power system with wind power penetration,” in IET Conference on Renewable Power Generation, Edinburgh, pp. 1-6, 6-8 September 2011.

[59] W. S. Mota and L. S. Barros, “Dynamic simulations of wind generators connected to distribution systems,” in 18th International Conference and Exhibition on Electricity Distribution, Turin, Italy, pp. 1-4, 6-9 June 2005.

[60] N. K. Roy, H. R. Pota, M. J. Hossain, and D. Cornforth, “Impact of SCIG and DFIG type wind turbine on the stability of distribution networks: static and dynamic aspects,” in International Conference on Environment and Electrical Engineering (EEEIC), Venice, pp. 543-548, 18-25 May 2012.

[61] E. Vittal, M. O'Malley, and A. Keane, “A steady-state voltage stability analysis of power systems with high penetrations of wind,” IEEE Transactions on Power Systems, vol. 25, no. 1, pp. 433-442, 2010.

[62] L. T. Ha and T. K. Saha, “Investigation of power loss and voltage stability limits for large wind farm connections to a sub-transmission network,” in IEEE Power Engineering Society General Meeting, Denver, CO, vol. 2, pp. 2251-2256, 10 June 2004.

[63] G. D. Marzio, O. B. Fosso, K. Uhlen, and M. p. Palsson, “Large-scale wind power integration, voltage stability limits and modal analysis,” in Power Systems Computation Conference, Liege, Belgium, pp. 1-7, 22-26 August 2005.

[64] G. J. Rogers, Power System Oscillations, London, Kluwer Academic Publishers, 2000.

[65] B. Pal and B. Chaudhuri, Robust Control in Power Systems, New York, US: Springer-Verlag New York Inc., 2005.

[66] B. R. Gupta, Power system analysis and design, New Delhi, India: S. Chand & Company Ltd, 2008.

[67] B. Gao, G. K. Morison, and P. Kundur, "Voltage stability evaluation using modal analysis," IEEE Transactions on Power Systems, vol. 7, no. 4, pp. 1529-1542, November 1992.

[68] I. P. S. R. Committee, "Voltage collapse mitigation," December 1996. [Online]. Available: www.pes-psrc.org/Reports/Voltage Collapse Mitigation.pdf.

[69] T. Aziz, T. K. Saha, and N. Mithulananthan, "Static and dynamic var planning to support widespread penetration of distributed generation in distribution system", Australasian Universities Power Engineering Conference (AUPEC), Brisbane, Australia, 25-28 Sept. 2011, pp. 1-6.

[70] D. Jakus, R. Goic, and J. Krstulovic, "The impact of wind power plants on slow voltage variations in distribution networks", Electric Power Systems Research, vol. 81, pp. 589-598, 2011.

[71] N. A. Lahacani, D. Aouzellag, and B. Mendil, "Static compensator for maintaining voltage stability of wind farm integration to a distribution network", Renewable Energy, Vol. 35, pp. 2476-82, 2010.

[72] L. Mariotto, H. Pinheiro, G. Cardoso, and M. R. Muraro, " Determination of the static voltage stability region of distribution systems with the presence of wind power generation", International Conference on Clean Electrical Power, Capri, 21-23 May 2007, pp. 556-562.

[73] N. T. Linh, "Voltage stability analysis of grids connected wind generators", IEEE Conference on Industrial Electronics and Applications, Xi'an, 25-27 May 2009, pp. 2657-2660.

[74] N. K. Roy, H. R. Pota, and M. J. Hossain, "Reactive power management of distribution networks with wind generation for improving voltage stability", Renewable Energy, Vol. 58, pp. 85-94, 2013.

[75] B. Dong, S. Asgarpoor, and W. Qiao, "Voltage analysis of distribution systems with DFIG wind turbines", IEEE Power Electronics and Machines in Wind Applications, pp. 1-5Lincoln, NE, 24-26 June 2009.

[76] R. Piwko, N. Miller, J. Sanchez-Gasca, X. Yuan, R. Dai, and J. Lyons, "Integrating large wind farms into weak power grids with long transmission lines",

IEEE/PES Transmission and Distribution Conference and Exhibition: Asia and Pacific, pp. 1-7, Dalian, China, 2005.

[77] M. W. Mustafa, N. Magaji, and Z. B Muda, "TCSC control of power system oscillation and analysis using eigenvalue techniques," International Journal of Engineering & Technology, vol. 9, no. 10, pp. 37-43, 2009.

[78] S. Dahal, N. Mithulananthan, and T. Saha, "An approach to control a photovoltaic generator to damp low frequency oscillations in an emerging distribution system", IEEE Power and Energy Society General Meeting, pp. 1-8, 2011.

[79] P. Zhang, A. R. Messina, A. Coonick, and B. J. Cory, "Selection of locations and input signals for multiple SVC damping controllers in large scale power systems," in IEEE Power Engineering Society Winter Meeting, New York, vol. 1, pp. 667-670, 31 January- 4 February 1999.

[80] N. Martins and L. T. G. Lima, "Determination of suitable locations for power system stabilizers and static VAR compensators for damping electromechanical oscillations in large scale power systems," in Power Industry Computer Application Conference, Seattle, WA, USA, pp. 74-82, 1-5 May 1989.

[81] J. Suo, Z. Hu, Z. Zhang, and Y. Liu, "Damping controller design of power system with wind farms based on a novel identification method", International Conference on Mechatronics and Automation, pp. 1446-1451, Tianjin, 3-6 August 2014.

[82] M. Singh, A. J. Allen, E. Muljadi, V. Gevorgian, Y. Zhang, and S. Santoso, "Interarea oscillation damping controls for wind power plants", IEEE Transactions on Sustainable Energy, vol. 6, no. 3, July 2015.

[83] E. V. Larsen, J. J. Sanchez-Gasca, and J. H. Chow, "Concepts for design of FACTS controllers to damp power swings," IEEE Transactions on Power Systems, vol. 10, no. 2, pp. 948-956, May 1995.

[84] P. Pourbeik, R. J. Koessler, D. L. Dickmander, and W. Wong, "Integration of large wind farms into utility grids (Part 2- performance issues)," in IEEE Power Engineering Society General Meeting, pp. 1520-1525, vol. 3, pp. 1520-1525, 13-17 July 2003.

[85] H. F. Wang, F. Li, and R. G. Cameron, "FACTS control design based on power system nonparametric models," IEE Proceedings on Generation, Transmission and Distribution, vol. 146, no. 5, pp. 409-415, September 1999.

[86] J. Li, H. Shen, H. Li, and B. Huang, "Investigation on the 750 kV fixed series compensation scheme of Hexi wind power transmission corridor in Northwest

China grid," Transmission and distribution conference and exposition, Asia and Pacific, Seoul, South Korea, pp. 1-5, 2009.

[87] S. Panda and N. P. Padhy, "A PSO-based SSSC controller for improvement of transient stability performance," International Journal of Electrical and Computer Engineering, vol. 1, no. 9, pp. 1303-1310, 2007.

[88] S. Panda, "Modelling, simulation and optimal tuning of SSSC-based controller in a multi-machine power system," World Journal of Modelling and Simulation, vol. 6, no. 2, pp. 110-121, 2010.

[89] V. Salehi, S. Afsharnia, and S. Kahrobaee, "Improvement of voltage stability in wind farm connection to distribution network using FACTS devices", IEEE 32nd Annual Conference on Industrial Electronics, pp. 4242-4247, November 2006, Paris, France.

[90] F. Shahnia, R. Sumedha, and A. Ghosh, Static compensators (STATCOMs) in power systems, Springer, 2015.

[91] T. M. Masaud and P. K. Sen, "Study of the implementation of STATCOM on DFIG-based wind farm connected to a power system," IEEE Conference on Innovative Smart Grid Technologies (ISGT), Washington, DC, pp. 1-7, 16-20 January 2012.

[92] L. Wang and H. Jia, "STATCOM impact on small signal stability of wind farm integration," IEEE Conference on Innovative Smart Grid Technologies-Asia (ISGT Asia), Tianjin, pp. 1-5, 21-24 May 2012.

[93] E. Zhou, "Application of static VAR compensators to increase power system damping," IEEE Transactions on Power Systems, vol. 8, no. 2, pp. 655-661, May 1993.

[94] L. Li, S. Liangliang, Y. Yihan, M. Youzhong, and W. Tao, "Impact of SVC on small signal stability of induction generator connected power systems," Power and Energy Engineering Conference (APPEEC), Beijing, China, pp. 1-4, 2010.

[95] H. F. Wang, F. J. Swift, and M. Li, "Selection of installing locations and feedback signals of facts-based stabilizers in multimachine power systems by reduced-order modal analysis", IEE Proceeding-Generation Transmission and Distribution, vol. 144, no. 3, pp. 263-269, May 1997.

[96] N. Martins and L. T. G. Lima, "Determination of suitable locations for power system stabilizers and static VAR compensators for damping electromechanical

oscillations in large scale power systems," IEEE Transactions on Power Systems, vol. 5, no. 4, pp. 1455-1469, 1990.

[97] S. Dahal, N. Mithulananthan, and T. K. Saha, “Enhancing small signal stability of an emerging distribution system by a coordinated controller”, IEEE Power and Energy Society General Meeting, pp. 1-8, 2012.

[98] S. Dahal, N. Mithulananthan, and T. Saha, “Enhancement of small signal stability of a renewable energy based electricity distribution system using shunt controller”, Australasian Universities Power Engineering Conference (AUPEC), pp. 1-6, Christchurch, New Zealand, 5-8 December 2010.

[99] S. Dahal, N. Mithulananthan, and T. K. Saha, “Assessment and enhancement of small signal stability of a renewable energy based electricity distribution system”, IEEE Transactions on Sustainable Energy, vol. 3, no. 3, pp. 407-415, July 2012.

[100] M. Sedighizadeh, S. A. Fatemi, A. Rezazadeh, and M. Khatibi, “Selecting of SSSC control mode to improve transient and small signal stability in Iran National Grid,” in International Conference on Universities Power Engineering, Padova, pp. 1-5, 1-4 September 2008.

[101] Y. Li, C. Rehtanz, S. Ruberg, L. Luo, and Y. Cao, “Assessment and choice of input signals for multiple HVDC and FACTS wide-area damping controllers,” IEEE Transactions on Power Systems, vol. 27, no. 4, pp. 1969-1977, November 2012.

[102] M. M. Farsangi, Y. H. Song, and K. Y. Lee, “Choice of FACTS device control inputs for damping interarea oscillations,” IEEE Transactions on Power Systems, vol. 19, no. 2, pp. 1135-1143, May 2004.

[103] K. Elkington, and M. Ghandhari, “Non-linear power oscillation damping controllers for doubly fed induction generators in wind farms”, IET Renewable Power Generation, vol. 7, no. 2, pp.172-179, March 2013.

[104] A. E. Leon, and J. A. Solsona, “Power oscillation damping improvement by adding multiple wind farms to wide-area coordinating controls”, IEEE Transactions on Power Systems, vol. 9, No. 3, May 2014.

[105] H. F. Latorre and M. Ghandhari, “Improvement of power system stability by using a VSC-HVDC,” International Journal of Electrical Power and Energy Systems, vol. 33, no. 1, pp. 332-339, 2011.

[106] G. M. Huang and V. Krishnaswamy, “HVDC controls for power system stability,” in IEEE Power Engineering Society Summer Meeting, Chicago, IL, USA, vol. 1, pp. 597-602, 25 July 2002.

[107] C. Nguyen-Mau, K. Rudion, and Z. A. Styczynski, “HVDC application for enhancing power system stability, EPU-CRIS International Conference on Science and Technology. Hanoi, Vietnam, 16 November 2011.

[108] U. V. Marreddy and R. Rao P.V, “Damping effects of supplementary control signals for enhancement of transient stability in AC-DC power systems,” International Journal of Engineering Science and Technology, vol. 2, no. 7, pp. 3084-92, 2010.

[109] X. Yao, H. Sui, and Z. Xing, “The study of VSC-HVDC transmission system for offshore wind power farm,” in International Conference on Electrical Machines and Systems, Seoul, pp. 314-319, 8-11 October 2007.

[110] E. Spahic and G. Balzer, “Offshore wind farms - VSC-based HVDC connection,” in IEEE Conference on Power Tech, St. Petersburg, pp. 1-6, 27-30 June 2005.

[111] S. K. Chaudhary, R. Teodorescu, and P. Rodriguez, “Wind farm grid integration using VSC based HVDC transmission-An overview,” IEEE Conference on Energy 2030, Atlanta, GA, pp. 1-7, 17-18 November 2008.

[112] L. Wang and K. H. Wang, “Dynamic stability analysis of a DFIG-based offshore wind farm connected to a power grid through an HVDC link,” IEEE Transactions on Power Systems, vol. 26, no. 3, pp. 1501-1510, August 2011.

[113] X. Guo, Z. Lu, B. Wang, et al., “Dynamic phasors-based modelling and stability analysis of droop-controlled inverters for microgrid applications,” IEEE Transactions on Smart Grid, vol. 5, no. 6, pp. 2980-2987, 2014.

[114] R. H. Lasseter, “Microgrids,” IEEE Power Engineering Society Winter Meeting, vol. 1, pp. 305-308, 2002.

[115] Z. Xu, M. Nthontho, and S. Chowdhury, “Rural electrification implementation strategies through microgrid approach in South African context,” International Journal of Electrical Power & Energy Systems, vol. 82, pp. 452-465, 2016.

[116] J. M. Guerrero, J. C. Vasquez, J. Matas, et al., “Hierarchical control of droop-controlled ac and dc microgrids-a general approach toward standardization,” IEEE Transactions on Industrial Electronics, vol. 58, no. 1, pp. 158-172, 2011.

[117] J. M. Guerrero, M. Chandorkar, T.L. Lee, and P. C. Loh, “Advanced control

architectures for intelligent microgrids-part I: decentralized and hierarchical control," IEEE Transactions on. Industrial Electronics, vol. 60, no. 4, pp. 1254-1262, 2013.

[118] M. Yazdanian, and A. Mehrizi-Sani, "Distributed control techniques in microgrids," IEEE Transactions on Smart Grid, vol. 5, no. 6, pp. 2901-2909, 2014.

[119] F. A. Rengifo, L. Romeral, J. Cusido, and J. J. Cardenas, "New model of a converter-based generator using electrostatic synchronous machine concept," IEEE Transactions on. Energy Conversion, vol. 29, no. 2, pp. 344-353, 2014.

[120] X. Tang, W. Deng, and Z. Qi, "Investigation of the dynamic stability of microgrid," IEEE Transactions on. Power Systems, vol. 29, no. 2, pp. 698-706, 2014.

[121] R. Majumder, "Some aspects of stability in microgrids," IEEE Transactions on. Power Systems, vol 28, no. 3, pp. 3243-3252, 2013.

[122] N. Pogaku, M. Prodanovic, and T.C. Green, "Modelling, analysis and testing of autonomous operation of an inverter-based microgrid," IEEE Transactions on Power Electronics, vol. 22, no. 2, pp. 613-625, 2007.

[123] M. Rasouli and R. Sabzehgar, "Reducing estimated parameters of a synchronous generator for microgrid applications," IEEE Conference on Energy Conversion, pp. 1-6, 2016.

[124] D. J. Lee and L. Wang, "Small-signal stability analysis of an autonomous hybrid renewable energy power generation/energy storage system part I: Time-domain simulations," IEEE Transactions on Energy Conversion, vol. 23, no. 1, pp. 311-320, 2008.

[125] E. A. A. Coelho, P. C. Cortizo, and P. F. D. Garcia, "Small-signal stability for parallel-connected inverters in stand-alone ac supply systems," IEEE Transactions on. Industry Applications, vol. 38, no. 2, pp. 533-542, 2002.

[126] M. Belkhayat, "Stability criteria for ac power systems with regulated loads," Ph.D. thesis, Purdue University, USA, 1997.

[127] R. D. Middlebrook, "Input filter consideration in design and application of switching regulators," IEEE Industrial Application Society Annual Meeting, pp. 366-382, 1976.

[128] Z. Zeng, H. Yang, and R. Zhao, "Study on small signal stability of microgrids: A review and a new approach," Renewable and Sustainable Energy Reviews, vol. 15, no. 9, pp. 4818-4828, 2011.

[129] J. Sun, “Small-signal methods for ac distributed power systems-A review,” IEEE Transactions on Power Electronics, vol. 24, no. 11, pp. 2545-2554, 2009.

[130] M. Amelian, R. Hooshmand, and A. Khodabakhshian, “Small signal stability improvement of a wind turbine-based doubly fed induction generator in a microgrid environment,” International Conference on Computer and Knowledge Engineering (ICCKE 2013), pp. 384-389, Ferdowsi University of Mashhad, Mashhad, 31 October-1 November, 2013.

[131] M. N. Marwali, J. W. Jung, and A. Keyhani, “Stability analysis of load sharing control for distributed generation systems,” IEEE Transactions on Energy Conversion, vol. 22, no. 3, pp. 737-745, 2007.

[132] E. Barklund, N. Pogaku, M. Prodanovic, et al., “Energy management in autonomous microgrid using stability-constrained droop control of inverters,” IEEE Transactions on Power Electronics, vol. 23, no. 5, pp. 2346-2352, 2008.

[133] R. Majumder, B. Chaudhuri, A. Ghosh, et al., “Improvement of stability and load sharing in an autonomous microgrid using supplementary droop control loop,” IEEE Transactions on Power Systems, vol. 25, no. 2, pp. 796-808, 2010.

[134] M. Rasheduzzaman, J. A. Mueller, and J. W. Kimball, “An accurate small-signal model of inverter-dominated islanded microgrids using dq reference frame,” IEEE Journal of Emerging and Selected Topics in Power Electronics, vol. 2, no. 4, pp. 1070-1080, 2014.

[135] F. Shahnia, and A. Arefi, “Eigenanalysis-based small signal stability of the system of coupled sustainable microgrids,” International Journal of Electrical Power & Energy Systems, vol. 91, no. 1, pp. 42-60, 2017.

[136] F. Shahnia, “Stability and eigenanalysis of a sustainable remote area microgrid with a transforming structure,” Sustainable Energy, Grids & Networks, vol. 8, no. 1, pp. 37-50, 2016.

[137] F. Katiraei, M. R. Iravani, and P. W. Lehn, “Small-signal dynamic model of a micro-grid including conventional and electronically interfaced distributed resources,” IET Generation, Transmission & Distribution, vol. 1, no. 3, pp. 369-378, 2007.

[138] S. Mishra, and D. Ramasubramanian, “Improving the small signal stability of a PV-DE-dynamic load-based microgrid using an auxiliary signal in the PV control Loop,” IEEE Transactions on Power Systems, vol. 30, no. 1, pp. 166-176, 2015.

[139] A. U. Krismanto and N. Mithulananthan, “Identification of modal interaction

and small signal stability in autonomous microgrid operation". IET Generation, Transmission & Distribution, vol. 12, no. 1, pp. 247-257, 2018.

[140] A. Jamehbozorg, and G. Radman, "Small signal analysis of power systems with wind and energy storage units," IEEE Transactions on Power Systems, vol. 30, no. 1, pp. 298-305, 2015.

[141] Z. Zhao, P. Yang, Y. Wang, et al., "Dynamic characteristics analysis and stabilization of PV-based multiple microgrid clusters," IEEE Transactions on. Smart Grid, doi: 10.1109/TSG.2017. 2752640, 2017.

[142] A. V. Jayawardena, L. G. Meegahapola, D. A. Robinson. et al., "Representation of a grid-tied microgrid as a reduced order entity for distribution system dynamics and stability studies", International Journal of Electrical Power and Energy, vol. 73, no. 1, pp. 591-600, 2015.

[143] V. Mariani, F. Vasca, J. C. Vasquez, and J. M. Guerrero, "Model order reductions for stability analysis of islanded microgrids with droop control," IEEE Transactions on. Industrial Electronics, vol. 62, no. 7, pp. 4344-4354, 2015.

[144] N. Bottrell, M. Prodanovic, and T. C. Green, "Dynamic stability of a microgrid with an active load," IEEE Transactions on Power Electronics, vol. 28, no. 11, pp. 5107-5119, 2013.

[145] A. A. A. Radwan and Y. A. R. I. Mohamed, "Stabilization of medium-frequency modes in isolated microgrids supplying direct online induction motor loads," IEEE Transactions on. Smart Grid, vol. 5, no. 1, pp. 358-370, 2014.

[146] I. Serban, R. Teodorescu, and C. Marinescu, "Energy storage systems impact on the short-term frequency stability of distributed autonomous microgrids, an analysis using aggregate models," IET Renewable Power Generation, vol. 7, no. 5, pp. 531-539, 2013.

[147] A. U. Krismanto, N. Mithulananthan, and I. Kamwa, "Oscillatory stability assessment of microgrid in autonomous operation with uncertainties," IET Renewable Power Generation, vol. 12, no. 4, pp. 494-504, 2018.

[148] F. M. Uriarte, C. Smith, S. VanBroekhoven, and R. E. Hebner, "Microgrid ramp rates and the inertial stability margin," IEEE Transactions on Power Systems, vol. 30, no. 6, pp. 3209-3216, 2015.

[149] C. Ahumada, R. Cardenas, D. Saez, and J. M. Guerrero, "Secondary control strategies for frequency restoration in islanded microgrids with consideration of communication delays," IEEE Transactions on Smart Grid, vol. 7, no. 3, pp. 1430-

1441, 2016.

[150] S. Tan, H. Geng, and G. Yang, “Stability analysis and improvement of LCL-converters based microgrid,” International Conference on Renewable Power Generation, pp. 1-6, 2015.

[151] F. Milano, “Power system analysis toolbox,” [Online]. Available: http://www.power.uwaterloo.ca/~fmilanno, 2010.

[152] B. C. Babu and K. B. Mohanty, “Doubly- fed induction generator for variable speed wind energy conversion systems - Modelling and simulation,” International Journal of Computer and Electrical Engineering, vol. 2, no. 1, pp. 141-147, 2010.

[153] G. H. Li, B. H. Zhang, Z. G. Hao, J. Wang, Z. Q. Bo, D. Writer, and T. Yip, “Modelling of DFIG based wind generator and transient characteristics analysis,” in International Conference on Environment and Electrical Engineering (EEEIC), Rome, pp. 1-4, 8-11 May 2011.

[154] L. M. Fernandez, C. A. Garcia, J. R. Saenz, and F. Jurado, “Equivalent models of wind farms by using aggregated wind turbines and equivalent winds,” Energy Conversion and Management, vol. 50, no. 3, pp. 691-704, 2009.

[155] R. C. Bansal, T. S. Bhatti, and D. P. Kothari, “On some of the design aspects of wind energy conversion systems,” Energy Conversion and Management, vol. 43, no. 16, pp. 2175-2187, 2002.

[156] N. Modi, T. Saha, and N. Mithulananthan, “Effect of wind farms with doubly fed induction generators on small signal stability- A case study on Australian equivalent system,” in IEEE PES Conference on Innovative Smart Grid Technologies Asia (ISGT), Perth, Australia, pp. 1-7, 13-16 November 2011.

[157] K. K. Sen, “SSSC-Static synchronous series compensator: Theory, modelling, and application,” IEEE Transactions on Power Delivery, vol. 13, no. 1, pp. 241-246, 1998.

[158] N. G. Hingorani and L. Gyugyi, Understanding FACTS: Concepts and technology of flexible AC transmission systems, New Jersey: Wiley-IEEE Press, 2000.

[159] N. Mithulananthan, C. A. Canizares, J. Reeve and G. J. Rogers, “Comparison of PSS, SVC, and STATCOM controllers for damping power system oscillations,” IEEE Transactions on Power Systems, vol. 18, no. 2, pp. 786-792, May 2003.

[160] N. Mithulananthan, C. A. Canizares, and J. Reeve, “Hopf bifurcation control in power system using power system stabilizers and static VAR compensators,” in

Annual North American Power Symposium, San Luis Obispo, California, pp. 1-8, 10-12 October 1999.

[161] "Matlab help files," MathWorks, [Online]. Available: http://www.mathworks.com/help/matlab.

[162] M. M. Farsangi, H. Nezamabadi-pour, Y. H. Song, and K. Y. Lee, "Placement of SVCs and selection of stabilizing signals in power systems," IEEE Transactions on Power Systems, vol. 22, no. 3, pp. 1061-1071, August 2007.

[163] H. M. Ayres, I. Kopcak, M. S. Castro, F. Milano, and V. F. da Costa, "A didactic procedure for designing power oscillation dampers of FACTS devices," Simulation Modelling Practice and Theory, vol. 18, no. 6, pp. 896-909, June 2010.

[164] P. W. Sauer and M. A. Pai, Power System Dynamics and Stability, Champaign, IL, Stipes Publishing L.L.C., 2006.

[165] F. M. Hughes, O. Anaya-Lara, N. Jenkins, and G. Strbac, "Control of DFIG based wind generation for power network support," IEEE Transactions on Power Systems, vol. 20, no. 4, pp. 1958-1966, 2005.

[166] P.C. Krause, Analysis of Electric Machinery and Drive Systems, Wiley, 2012.

[167] A. Ghosh, and G. Ledwich, Power Quality Enhancement using Custom Power Devices, Kluwer Academic, 2002.

[168] F. Shahnia, R. P. S. Chandrasena, S. Rajakaruna, and A. Ghosh, "Primary control level of parallel distributed energy resources converters in system of multiple interconnected autonomous microgrids within self-healing networks," IET Generation, Transmission & Distribution, vol. 8, no. 1, pp.203-222, 2014.

[169] H. Bevrani, and S. Shokoohi, "An intelligent droop control for simultaneous voltage and frequency regulation in islanded microgrids", IEEE Transactions on Smart Grid, vol. 4, no. 3, pp.1505-1513, 2013.

[170] I. U. Nutkani, P. C. Loh, P. Wang, and F. Blaabjerg, "Cost-prioritized droop schemes for autonomous ac microgrids," IEEE Transactions on Power Electronics, vol. 30, no. 2, pp. 1109-1119, 2015.

[171] T. Hosseinimehr, A. Ghosh, and F. Shahnia, "Cooperative control of battery energy storage systems in microgrids," International Journal of Electrical Power & Energy Systems, vol. 87, no. 1, pp.109-120, 2017.

[172] A. Tewari, Modern Control Design, Wiley, 2002.

[173] S. Dahal, N. Mithulananthan, and T. Saha, "Investigation of small signal stability of a renewable energy based electricity distribution system", IEEE Power and

Energy Society General Meeting, pp. 1-8, Minneapolis, MN, 25-29 July 2010.

[174] T. Aziz, S. Dahal, N. Mithulananthan, and T. K. Saha, "Impact of widespread penetrations of renewable generation on distribution system stability", International Conference on Electrical and Computer Engineering, pp. 338-341, Dhaka, Bangladesh, 18-20 December 2010.

[175] K. Prasertwong, N. Mithulananthan, and D. Thakur, "Understanding low frequency oscillation in power systems", International Journal of Electrical Engineering Education, vol. 47, no. 3, pp. 248-262, 2010.

[176] C. Y. Chung, W. Lei, F. Howell, and P. Kundur, "Generation rescheduling methods to improve power transfer capability constrained by small-signal stability", IEEE Transactions on Power Systems, vol. 19, no. 1, pp. 524-530, 2004.

[177] University of Washington Electrical Engineering, Power system test case archive, 2013. [Online] Available: http://www.ee.washington.edu/research/pstca.

[178] R. Grunbaum, B. Halvarsson, and A. Wilk-Wilczynski, "FACTS and HVDC light for power system interconnections," Power Delivery Conference, pp. 1-18, Madrid, Spain, 1999.

Publications Arising from this Thesis

Journal articles

1) **Amit Kunwar**, F. Shahnia, and R.C. Bansal, "Eigenvalue-oriented dynamic stability examination to enhance the design of a microgrid hosting a cluster of inertial and non-inertial distributed generators," under review in *IEEE Transaction on Smart Grid*, TSG-00062-2019, submitted on 11/01/2019.
2) **Amit Kunwar**, and R.C. Bansal, "A supplementary controller for improvement of small signal stability of power system with wind power penetration", *Electric Power Components and Systems*, 44(16):1825-1838, 2016.
3) **Amit Kunwar** and R.C. Bansal, "Stability analysis of power system with DFIG-based wind farm connected through series FACTS device compensated line," *International Journal of Ambient Energy*, 35(3):118-131, 2014.
4) **Amit Kunwar** and R.C. Bansal, "Effect of high voltage direct current link on small signal stability of power system with different penetration level of doubly fed induction generator and direct drive synchronous generator-based wind farms", *International Journal of Green Energy*, 13(4):335-343, 2014.
5) **Amit Kunwar**, R.C. Bansal, and O. Krause, "Steady state and transient voltage stability analysis of a weak distribution system with a remote doubly fed induction generator-based wind farm", *Energy Science and Engineering*, 2(4):188-195, 2014.

Conference paper

6) **Amit Kunwar**, F. Shahnia, and R.C. Bansal, "Impact of the capacity and number of inertial and non-inertial distributed energy resources within a microgrid on its stability margins," IEEE 27th International Symposium on Industrial Electronics (ISIE), Cairns, Australia, 2018.